

Microwave NDT&E using Open-ended Waveguide Probe for Multilayered Structures

A doctoral thesis submitted for the degree of Doctor of Philosophy

Ruslee Sutthaweekul



Intelligent, Sensing and Communications Research Group
(ISC),

School of Engineering, Newcastle University

September 2018

CERTIFICATE OF ORIGINALITY

This is to certify that all the works submitted in this thesis are my own works except as specified in acknowledgements. Neither the work nor the thesis has been submitted to any other institution for another degree. I am responsible for all the works in this thesis.

..... (Signed)

..... (Candidate)

*I dedicate this thesis to my sponsor - Ministry of Science and Technology,
Royal Thai Government*

Table of Contents

List of Figures.....	vii
List of Tables	xii
List of Publications	xiii
List of Abbreviations	xiv
Acknowledgements	xvii
Abstract.....	xviii
Chapter 1 Introduction.....	20
1.1 Background.....	20
1.2 Aim and Objectives	23
1.3 Research Scopes	24
1.4 Major Achievements.....	25
1.5 Research Methodology	26
1.5.1 Study 1: Steel corrosion stages characterisation.....	27
1.5.2 Study 2: Detection of impact damage on woven CFRP composites	28
1.5.3 Study 3: Detection and evaluation of flat-bottom holes in coated GFRP pipe.....	28
1.6 Thesis layout.....	28
1.7 Chapter Summary	29
Chapter 2 Literature Review.....	30
2.1 Review of NDT&E Approaches for Multilayered Structure.....	30
2.1.1 Eddy Current Testing.....	30
2.1.2 Ultrasonic Testing.....	31
2.1.3 Thermography	33
2.1.4 Radiography.....	34
2.1.5 Microwave and Millimetre-wave NDT	35
2.1.6 Comparison of NDT approaches for Multilayered Structures.....	37
2.2 Microwave NDT using Open-ended Waveguide Probe	39
2.2.1 Non-destructive Evaluation of Steel Corrosion under Paint	40
2.2.2 Inspection of Impact Damage on Woven Carbon Fibre Composites	43
2.2.3 Inspection of Inner Defects in Glass Fibre Reinforced Pipe	45

2.2.4 Quantitative Non-destructive Evaluation	47
2.2.5 Synthetic Aperture Imaging.....	51
2.3 Identification of Challenges in Microwave NDT&E for Multilayered Structures.....	52
2.4 Chapter Summary	53
Chapter 3 Development of Microwave NDT&E System.....	54
3.1 Background of Microwave NDT&E using Open-ended Waveguide Probe.....	54
3.2 Multilayered Models for Microwave NDT&E Experimental Studies.....	56
3.2.1 Corrosion Progression Sample	56
3.2.2 Woven CFRP with Impact damage	57
3.2.3 Glass Fibre Reinforced Polymer with Flat-bottom hole defects	59
3.3 Design and Implementation of Microwave NDT&E System.....	60
3.3.1 Design of Microwave NDT&E System.....	60
3.3.2 Implementation of Microwave NDT&E System.....	61
3.3.3 Feature Extraction.....	65
3.3.4 Synthetic Aperture Radar Imaging	70
3.4 Chapter Summary	73
Chapter 4 Steel Corrosion Stages Characterisation.....	74
4.1 Open-ended Rectangular Waveguide Measurement	74
4.2 Corrosion Samples.....	76
4.2.1 Uncoated Corrosion Samples	76
4.2.2 Coated Corrosion Samples	76
4.2.3 Surface Preparation Samples with Corroded Surface.....	77
4.3 Experimental Setup.....	78
4.4 Experimental Results and Discussion.....	79
4.4.1 Spectral Responses of Corrosion.....	79
4.4.2 PCA for Feature Extraction of Corrosion Progress	82
4.4.3 PCA Results Comparison and Discussion.....	83
4.5 Chapter Summary	86
Chapter 5 Detection and Characterisation of Impact Damage on Woven CFRP.....	88
5.1 Simulation Studies of Woven CFRP models.....	88
5.1.1 Grid Model (t=0)	89

5.1.2 Plain and 5HS models.....	90
5.1.3 5HS with Multi-ply model.....	91
5.1.4 Discussion on Simulation Results	92
5.2 Experimental Studies	93
5.2.1 Woven CFRP with Impact Damage Samples.....	93
5.2.2 Measurement Setup	94
5.2.3 Experiment results	95
5.3 Feature Extraction of Impact Damage.....	98
5.3.1 Framework for Feature Extraction of Impact damage.....	98
5.3.2 Frequency Selection and PCA feature.....	99
5.4 Quantitative Evaluation of Impact Damage on Woven CFRP	100
5.5 Chapter Summary	100
Chapter 6 Detection and Evaluation of Flat Bottom Hole Defects on Coated GFRP Pipe	102
6.1 GFRP Pipe Composite Model	102
6.2 FRP Pipe Samples	103
6.3 Experiment Setup for FRP Pipe Inspection using Open-ended Waveguide Probe	104
6.4 Experiment Result and Validation.....	106
6.4.1 Magnitude and Phase Features Images.....	106
6.4.2 PC Feature Images.....	106
6.4.3 SAR Tomography.....	107
6.5 Quantitative Evaluation of Flat Bottom Hold Defects	108
6.5.1 Quantitative Evaluation of Location and Size.....	109
6.5.2 Quantitative Evaluation of Depth.....	110
6.6 Chapter Summary	113
Chapter 7 Conclusions and Future Work	115
7.1 Conclusions of Major Contributions	115
7.2 Future Work Suggestions	117
References	120

List of Figures

Figure 1.1 Corrosion effects [2]	20
Figure 1.2 (a) Composite aircraft Boeing 787 Dreamliner, (b) impact damage on a multi-hull forward beam of racing yacht composites [6], (c) Boeing 787s was damaged by hail on July 27, 2015 [7].	21
Figure 1.3 Emerging composite materials: (a) reinforced by particles, (b) reinforced by chopped fibres, (c) unidirectional, (d) laminates, (e) woven reinforced plastic and (f) honeycomb sandwich [10].	22
Figure 1.4 Research Methodology.....	27
Figure 2.1 High frequency ECT measurement (a) stacked layers, (b) copper coated PET samples, (c) measurement operation [20].	30
Figure 2.2 UT System and multilayer rivet sample [31].	32
Figure 2.3 (a) passive thermography and (b) active thermography (microwave source) [35].	33
Figure 2.4 Images obtained from XCT measurement include original sample slide and corrosion products [53].	35
Figure 2.5 A microwave open-ended rectangular waveguide radiating into an N -layer structure backed by conducting plate [76].	36
Figure 2.6 (a) a fibreglass pipe or tank inspected by an open-ended waveguide probe [95] (b) a modified open-ended rectangular waveguide probe radiating into a two-layer coating (i.e., paint and primer) with conducting substrate (carbon composite) [96].	39
Figure 2.7 Three basic configurations of dielectric medium (a) infinite thickness, (b) finite thickness terminated by a metallic plate and (c) finite thickness and unterminated, yielding a stratified structure [94].	40
Figure 2.8 (a) uniform corrosion-time relationship (b) illustration of uniform corrosion product.	41
Figure 2.9 The different models of corrosion sublayers (a) two layers, (b) no layer and (c) three layers [107].	41
Figure 2.10 (a) a steel sample with the scanned area and (b) image at 70 GHz (arrows indicate pitting) [68].	42

Figure 2.11 (a) Microscopic observations of the different damage mechanisms within a 100 J impacted 3D woven plate [120] (b) Illustration of typical CFRP defects from impact damage [36].	43
Figure 2.12 GFRP pipe wall: schematic presentation (left), cut section (right) [134].	45
Figure 2.13 Machine learning system architecture for defect quantitative evaluation.	47
Figure 2.14 The concept of linear PCA and Kernel PCA [171].	50
Figure 2.15 (a) sample before pouring mortar, (b) measurement setup, and (c) reconstructed high-resolution 3-D (volumetric) image from experimentally collected data at K-band (units: cm) [194].	51
Figure 3.1 Plane wave transmission and reflection in multilayered media based on transmission line model	55
Figure 3.2 E-field and H-field distribution of rectangular open-ended waveguide operating in TE ₁₀ mode	55
Figure 3.3 Models of corrosion progress (a) with coating and (b) without coating	57
Figure 3.4 Structure of 3D woven composites composed of a matrix of polymer (blue) and carbon fibre bundles in different directions (other colours) [205].	58
Figure 3.5 Defects of impact damage at different impact energies	58
Figure 3.6 Model of woven CFRP with impact damage	59
Figure 3.7 A model of GFRP pipe with FBH defect	60
Figure 3.8 System diagram of Microwave NDT using open-ended waveguide probe	61
Figure 3.9 Microwave NDT using open-ended waveguide system configuration (a) system illustration and (b) actual system implementation.	62
Figure 3.10 Flowchart of C-scan operation of microwave NDT&E system	64
Figure 3.11 Graphical user interface (GUI) of microwave NDT&E system.	64
Figure 3.12 Four scanning operation modes: (a) probing (A-scan), (b) raster scanning (C-scan), (c) raster probing and (d) lift-off	65
Figure 3.13 An example of microwave reflection coefficient response with peak magnitude and peak frequency features	67
Figure 3.14 Time-of-flight feature extraction process for time domain signals.	68
Figure 3.15 PCA for feature extraction	69

Figure 3.16 PC feature value extraction of a single spectrum response.....	70
Figure 3.17 PC feature image extraction of spatial-spectral responses.....	70
Figure 3.18 A monostatic OEW probe C-scan for 2-D SAR imaging.....	71
Figure 3.19 Dispersion in kz for plane wave decomposition using ω - k algorithm.....	72
Figure 3.20 2-D SAR processing for wideband signal.....	72
Figure 3.21 A monostatic OEW probe C-scan for SAR Tomography.....	73
Figure 3.22 SAR-tomography processing.....	73
Figure 4.1 (a) Open-ended waveguide field distribution in TE_{10} mode, and (b) a corrosion model of corrosion under coating.....	75
Figure 4.2 Uncoated corrosion progression samples.....	76
Figure 4.3 Coated corrosion progression samples.....	77
Figure 4.4 Surface preparation samples range.....	77
Figure 4.6 experiment for obtaining reflection coefficients over corrosion samples.....	78
Figure 4.7 Average magnitude responses of UP samples obtained by WR-62: (a) M0, (b) M1, (c) M3, (d) M6, (e) M10, (f) M12 and WR-42: (g) M0, (h) M1, (i) M3, (j) M6, (k) M10, (l) M12.....	80
Figure 4.8 Average magnitude responses of CP samples obtained by WR-62: (a) M0, (b) M1, (c) M3, (d) M6, (e) M10, (f) M12 and WR-42: (g) M0, (h) M1, (i) M3, (j) M6, (k) M10, (l) M12.	81
Figure 4.9 Average magnitude of the reflection coefficients of the coating layer from CP samples (C1-C12) measured by (a) WR-62 and (b) WR-42.	81
Figure 4.10 Average magnitude responses of US samples obtained by WR-62: (a) US1, (b) US2, (c) US3, (d) US4 and WR-42: (e) US1, (f) US2, (g) US3, (h) US4.....	82
Figure 4.11 PCA for feature extraction of corrosion progression.....	83
Figure 4.12 PC1-PC3 projected values of UP samples: (a) WR-62 PC1, (b) WR-62 PC2, (c) WR-62 PC3, (d) WR-42 PC1, (e) WR-42 PC2, (f) WR-42 PC3; PC projected values of CP samples: (g) WR-62 PC1, (h) WR-62 PC2, (i) WR-62 PC3, (j) WR- 42 PC1, (k) WR-42 PC2 and (l) WR-42 PC3.....	84
Figure 4.13 PC1-PC3 projected values of US samples: (a) WR-62 PC1, (b) WR-62 PC2, (c) WR-62 PC3, (d) WR-42 PC1, (e) WR-62 PC2, (f) WR-62 PC3.....	86

Figure 5.1 Simulation models of three plies 5HS CFRP and open-ended waveguide	88
Figure 5.2 Unit Cell model of CFRP weave: (a) Plain and (b) 5 Harness-satin.....	89
Figure 5.3 Responses of grid models (a) $w=0.5\text{mm}$, $g=1\text{mm}$, (b) $w=1\text{mm}$, $g=1\text{mm}$, (c) $w=1\text{mm}$, $g=0.5\text{mm}$	90
Figure 5.4 Responses of Plain weave models: (a) $t=0\text{mm}$ (b) $t=0.25\text{mm}$, (c) $t=0.5\text{mm}$	91
Figure 5.5 Responses of 5HS weave models: (a) $t=0\text{mm}$ (b) $t=0.25\text{mm}$, (c) $t=0.5\text{mm}$	91
Figure 5.6 Multi-ply 5HS weave model and their response: (a) $n=1$ (b) $n=2$, (c) $n=3$	92
Figure 5.7 E-field distribution on the CFRP with a grid model	93
Figure 5.8 E-field distribution on the CFRP with a plain weave model	93
Figure 5.9 Woven CFRP with impact damage ranging from 2J to 10J.....	94
Figure 5.10 Measurement setup for CFRP inspection.....	94
Figure 5.11 Microwave responses of 5HS CFRP sample with and without impact damage: (a) a reconstructed image of 6J sample, (b) response of non-impact, (c) response of impact damage, (d) average responses from non-impact and impact damage.	96
Figure 5.12 Reconstructed images of 6 J impact damage sample using average magnitude feature: (left) original (right) with 2-D SAR correction.	97
Figure 5.13 the framework for PC based feature extraction of impact damage.....	98
Figure 5.14 Reconstructed images based on features extracted from PC1-PC6	99
Figure 5.15 Images of impact damages of 2J to 10J samples presented by PC6 features.....	100
Figure 5.16 k-mean clustering of impact damage at 2J to 10J samples	100
Figure 6.1 Microwave Open-ended Waveguide for GFRP pipe scanning.....	103
Figure 6.2 The GFRP pipe sample with 4 FBHs.....	104
Figure 6.3 Equipment setup for OEW scanning system of GFRP pipe	105
Figure 6.4 Measurement setup for scanning GFRP pipe sample	105
Figure 6.5 Images of FBHs reconstructed by features: average magnitude (AM), average phase (AP), and principal components (PC1-PC4) with ROI.	106
Figure 6.6 Tomography representing the location of FBHs: (a) H1, (b) H2, (c) H3 and (d) H4	108

Figure 6.7 Process block diagram of FBH evaluation based on PC and tomography features	109
Figure 6.8 Cross section plot of FBHs by ROI centred and normalised of (a) PC3 feature and (b) SAR tomography feature	110
Figure 6.9 Process block diagram of ToF feature extraction from FBH response.....	111
Figure 6.10 Time-domain signal at H1 centre: (a) original (b) background (c) background subtracted.....	111
Figure 6.11 Reflected signals of FBHs: (a) H1, (b) H2, (c) H3 and (d) H4.....	112
Figure 6.12 Time-of-flight feature against defect depth: (a) amplitude, (b) time delay.....	113

List of Tables

Table 2.1	Advantages and limitations of various NDT&E methods for multilayered structures.....	38
Table 4.1	The properties of WR-62 and WR-42 probes in the TE_{10} mode.....	74
Table 4.2	Properties of surface preparation samples	77
Table 4.3	Measurement parameters	78
Table 4.4	Standard deviations of uncoated (UP) and coated (CP) corrosion samples at 0° and 90°	84
Table 4.5	Standard deviations of uncoated surface preparation (US) samples at 0° and 90°	86
Table 5.1	Measurement parameters of CFRP impact damage detection and texture inspection.....	95
Table 5.2	The images of woven CFRPs with impact damage 4J – 10J at scanning step size ranging from $a/2$ to $a/20$	97
Table 5.3	Principal Components PC1-PC6 from spectral responses over the scanning area	99
Table 6.1	GFRP pipe sample parameters and values.....	104
Table 6.2	OEW Measurement Parameters and values.....	105
Table 6.3	Locations of FBH determined from PC3 and tomography.....	109
Table 6.4	FBH size of PC3 and tomography features	110
Table 6.5	Time-of-flight features from FBHs	113

List of Publications

Journal Articles

1. Sutthaweekul, R., & Tian, G. Y. (2017). Steel corrosion stages characterization using open-ended rectangular waveguide probe. *IEEE Sensors Journal*, 18(3), 1054-1062.
2. Sutthaweekul, R., Tian, G. Y., Wang, Z., & Ciampa, F. (2019). Microwave Open-ended Waveguide for Detection and Characterisation of FBHs in Coated GFRP Pipes. *Composite Structures*, 111080.

Conference Papers

1. R. Sutthaweekul, A. M. J. Marindra, and G. Y. Tian, "Study of microwave responses on layered woven CFRP composites," in *2017 9th International Conference on Information Technology and Electrical Engineering (ICITEE)*, 2017, pp. 1–5.
2. R. Sutthaweekul, G. Y. Tian, and M. D. Buhari, "Detection of impact damage and fibre texture on CFRP using open-ended waveguide probe," in *2016 13th International Conference on Electrical Engineering/Electronics, Computer, Telecommunications and Information Technology (ECTI-CON)*, 2016, pp. 1–6.
3. R. Sutthaweekul, M. D. Buhari, A. I. Sunny, and G. Y. Tian, "Influence of lift-off on microwave open-ended waveguide time of flight based tire inspection," in *2016 International Conference for Students on Applied Engineering (ICSAE)*, 2016, pp. 275–279.

Related works

1. C. Tang, G. Y. Tian, K. Li, R. Sutthaweekul, and J. Wu, "Smart Compressed Sensing for Online Evaluation of CFRP Structure Integrity," *IEEE Transactions on Industrial Electronics*, vol. PP, no. 99, pp. 1–1, 2017.
2. Buhari, M. D., G. Y. Tian, R. Tiwari, R. Sutthaweekul, and A. H. Muqaibel. "OFDM SAR Multiple Targets Image Reconstruction Using MUSIC-LSE Algorithm." In *2016 4th International Workshop on Compressed Sensing Theory and Its Applications to Radar, Sonar and Remote Sensing (CoSeRa)*, 42–46, 2016.

List of Abbreviations

AM	Average Magnitude
AP	Average Phase
BVID	Barely Visible Impact Damage
CFRP	Carbon Fibre Reinforced Polymer
CMP	Common Midpoint
CSRR	Complementary Split-Ring Resonator
CT	Computed Tomography
DFT	Discrete Fourier Transform
DWT	Discrete Wavelet Transform
ECPT	Eddy Current Pulsed Thermography
ECT	Eddy Current Testing
EHD	Edge Histogram Descriptors
EM	Electromagnetic
EMAT	Electromagnetic Acoustic Testing
ESPRIT	Estimation of Signal Parameters via Rotational Invariance Techniques
FBH	Flat-Bottom Hole
FDTD	Finite Different Time Domain
FFT	Fast Fourier Transform
FSS	Frequency Selective Surface
FWI	Full Wave Inversion
GFRP	Glass Fibre Reinforced Polymer
GPIB	General Purpose Interface Bus
GPR	Ground Penetrating Radar
HHM	Hidden Markov Model
HHT	Hilbert-Huang Transform
HS	Harness Satin
HT	Hough Transform
ICA	Independent Component Analysis
IR	Infrared
LDA	Linear Discriminant Analysis
LPT	Long pulse Thermography
LPT	Parallel Port Interface

LT	Lock-in Thermography
MF	Matched Filter
MUSIC	Multiple Signal Classification
MWT	Microwave Thermography
NDT&E	Non-Destructive Testing and Evaluation
OEW	Open-Ended Waveguide
ORWG	Open-Ended Rectangular Waveguide
PCA	Principal Component Analysis
PCB	Printed Circuit Board
PEC	Pulsed Eddy Current
PPS	Polyphenylene Sulphide
PT	Pulsed Thermography
PZT	Piezoelectric Zirconate-titanate Transducer
QNDE	Quantitative Non-Destructive Evaluation
RCW	Rigorous Coupled Wave
RF	Radio Frequency
RFID	Radio Frequency Identification
ROI	Region of Interest
SAR	Synthetic Aperture Radar
SNR	Signal-to-Noise Ratio
SSPC	Steel Structures Painting Council
STFT	Short-Time Fourier Transform
SUT	Sample under Test
SVM	Support Vector Machine
SVR	Support Vector Regression
TDE	Time Delay Estimation
TDR	Time Domain Reflectometry
TE	Transverse Electric
TEM	Transverse Electromagnetic
THz-TDS	Terahertz Time Domain Spectroscopy
ToF	Time of Flight
TTV	Time Domain Reflectometry
UHF	Ultra High Frequency

UST	Ultrasonic Thermography
UT	Ultrasonic Testing
VNA	Vector Network Analyser

Acknowledgements

My deepest gratitude to my supervisor, Professor GuiYun Tian, a professor of sensor technologies at School of Engineering, Newcastle University. He has been consistently supporting throughout my years of the postgraduate research study. He dedicated his precious time and effort to take care of me and my colleagues in their progression of a research career. He gave me opportunities to work and explore research activities including industrial and academic projects. It is my pleasure to be a part of his research team.

My sincere thanks also go to Dr Rajesh Tiwari for an introduction to universal radio software peripherals (USRPs), Dr Hong Zhang and Dr Jun Zhang, who introduced me to the microwave and RFID NDT. I would like to thank to all my colleagues and friends, Dr Ali Imam Sunny, Dr Aobo Zhao, Mohammed Buhari, Chaoqing Tang, Adi Marindra, Junzhen Zhu and Qiuji Yi for inspiring discussions and cheerful events. Thank to staffs and technicians, Paul Killan and Stephen Robson who always supported me in equipment needed and solving technical issues.

Special thanks to Dr Cristian Ulianov and Andy Hamer from NewRail, Newcastle University, who supervised and supported me through the RFID research for INNOWAG project. Thank to Matt Chamberlain from Radix2Design, and again my former colleagues, Dr Ali Imam Sunny and Denis Ona for the cooperating in the design and development of a novel PCB eddy current probe. Thank to my sponsor, Ministry of Science and Technology of Royal Thai Government and Office of Educational Affairs, the Royal Thai Embassy for financial supporting and taking care throughout the PhD study. Thank to my former supervisor, Dr Prayoot Akkaraekthalin from Electrical and Computer Engineering department, King Mongkut's University of Technology North Bangkok, for encouraging and supporting me to study aboard.

Thanks to my family, father (in-law), mother (in-law), brother and all relatives for supporting me as always. Finally, sincerely thanks to my wife who has been accompanying and supporting throughout the time in Newcastle, United Kingdom and Thailand.

Abstract

Microwave NDT&E has been proved to be suitable for inspecting of dielectric structures due to low attenuation in dielectric materials and free-space. However, the microwave responses from multilayered structures are complex as an interrogation of scattering electromagnetic waves among the layers and defects. In many practical applications, electromagnetic analysis based on analytic- and forward structural models cannot be generalised since the defect shape and properties are usually unknown and hidden beneath the surface layer.

This research proposes the design and implementation of microwave NDT&E system for inspection of multilayered structures. Standard microwave open-ended rectangular waveguides in X, Ku and K bands (frequency range between 8-26.5 GHz) and vector network analyser (VNA) generating sweep frequency of wideband monochromatic waves have been used to obtain reflection coefficient responses over three types of challenging multilayered samples: (1) corrosion progression under coating, (2) woven carbon fibre reinforced polymer (CFRP) with impact damages, and (3) thermal coated glass fibre reinforced polymer (GFRP) pipe with inner flat-bottom holes. The obtained data are analysed by the selected feature extraction method extracting informative features and verify with the sample parameters (defect parameters). In addition, visualisation methods are utilised to improve the presentation of the defects and material structures resulting in a better interpretation for quantitative evaluation.

The contributions of this project are summarised as follows: (1) implementation of microwave NDT&E scanning system using open-ended waveguide with the highest resolution of 0.1mm x 0.1 mm, based on the NDT applications for the three aforementioned samples; (2) corrosion stages of steel corrosion under coating have been successfully characterised by the principal component analysis (PCA) method; (3) A frequency selective based PCA feature has been used to visualise the impact damage at different impact energies with elimination of woven texture influences; (4) PCA and SAR (synthetic aperture radar) tomography together with time-of-flight extraction, have been used for detection and quantitative evaluation of flat-bottom hole defects (i.e., location, size and depth).

The results conclude that the proposed microwave NDT&E system can be used for detection and evaluation of multilayered structures, which its major contributions are follows.

- (1) The early stages (0-12month) of steel corrosion undercoating has been successfully characterised by mean of spectral responses from microwave opened rectangular waveguide probe and PCA.

- (2) The detection of low energy impact damages on CFRP as low as 4 Joules has been achieved with microwave opened rectangular waveguide probe raster scan together with SAR imaging and PCA for feature extraction methods.
- (3) The inner flat-bottom holes beneath the thermal coated GFRP up to 11.5 mm depth has been successfully quantitatively evaluated by open-ended waveguide raster scan using PCA and 3-D reconstruction based on SAR tomography techniques. The evaluation includes location, sizing and depth.

Nevertheless, the major downside of feature quantities extracted from statistically based methods such as PCA, is it intensely relies on the correlation of the input dataset, and thus hardly link them with the physical parameters of the test sample, in particular, the complex composite architectures. Therefore, there are still challenges of feature extraction and quantitative evaluation to accurately determine the essential parameters from the samples. This can be achieved by a future investigation of multiple features fusion and complementary features.

Chapter 1 Introduction

This chapter gives a brief introduction to Microwave non-destructive testing and evaluation (NDT&E) system for sensing and imaging of layered structures and an overview of the work carried out throughout the project. A summary of aim the objectives of the project is provided. The major research achievements are highlighted and finally, the thesis layout is described.

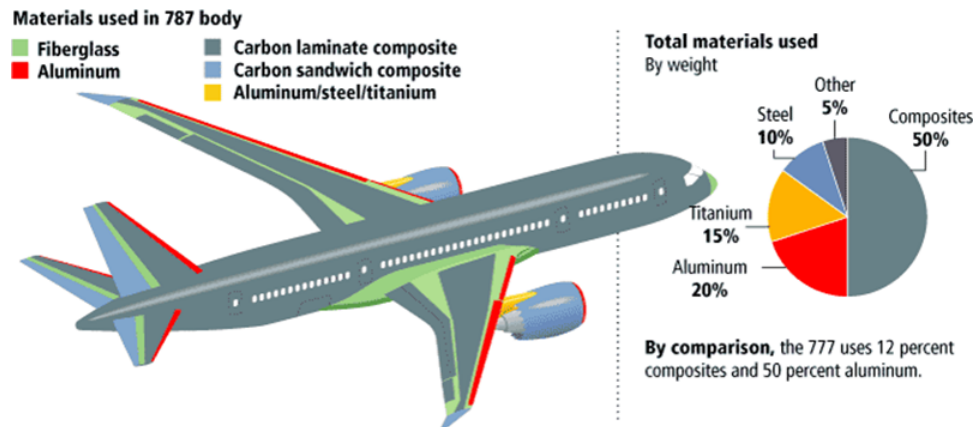
1.1 Background

Inspection and maintenance of most engineering structures require NDT&E, which refers to techniques used to evaluate materials by finding a physical phenomenon without causing damage or altering the specimen function [1]. For the existing structures, steel is known as the most common material providing strength to construction. However, steel is known to be deteriorated overtime by attacking of corrosion. Illustrated in Figure 1.1, corrosion causes failure in materials resulting in costs for maintenance, repair and replacement. Moreover, it may results in industrial leakages, contamination and tragic accidents. The standard method to prevent corrosion is applying coating layers (e.g., primer, paint, or insulation) on the steel surface. Although it may effectively control the generation of corrosion for a certain period, these coating layers often oppose to visual inspection and numerous NDT techniques.



Figure 1.1 Corrosion effects [2]

Although common steel surface has been protected by layers of coating, corrosion may still develop under the coating due to debonding and flaking of the coating layers overtime. This corrosion under coating is known as one of the significant problems in the oil and gas industries. To inspect corrosion or other types of defects under coating, several NDT&E methods require the removal of the protection layers to gain access to the steel surface [3], [4]. Some other methods such as x-ray tomography [5] may require off-line inspection causing downtime in the production.



(a)



(b)



(c)

Figure 1.2 (a) Composite aircraft Boeing 787 Dreamliner, (b) impact damage on a multi-hull forward beam of racing yacht composites [6], (c) Boeing 787s was damaged by hail on July 27, 2015 [7].

To overcome the problem of corrosion on steel, a new type of fibre composite materials have been recently developed [8]. Fibreglass or glass fibre is one of the first modern composites widely used for sports equipment, automobile and civil industries. The glass fibre is commonly made of a matrix of plastic reinforced with hair-like threads of glass [9]. With the requirement of material that stronger and lighter than steel, the fibre made of carbon was developed. However, it gains much higher cost due to complexity of manufacturing process. Therefore, the applications of carbon fibre are usually limited to sport equipment and aerospace industry. The example of structures made of carbon composite is shown in Figure 1.2. In Figure 1.2(a), the

newly developed Boeing 787 made use of over 50% of modern composites in its design, mainly carbon laminate composites. It offers weight savings on average of 20% compared to the conventional aluminium designs. However, in-use fibre composites still vulnerable to hazards, like impact damage caused by sea wave impact (Figure 1.2(b)), tool drops, hails (Figure 1.2(c)) and bird strikes. The typical damage induced in the polymer composites include surface dent, matrix crack, fibre breakage and delamination. These damages often occur within the internal structure leaving little or no evidence on the surface for the visual inspection. Therefore, it is important to investigate for a novel NDT technique that effectively applies for structural evaluation of these composites.

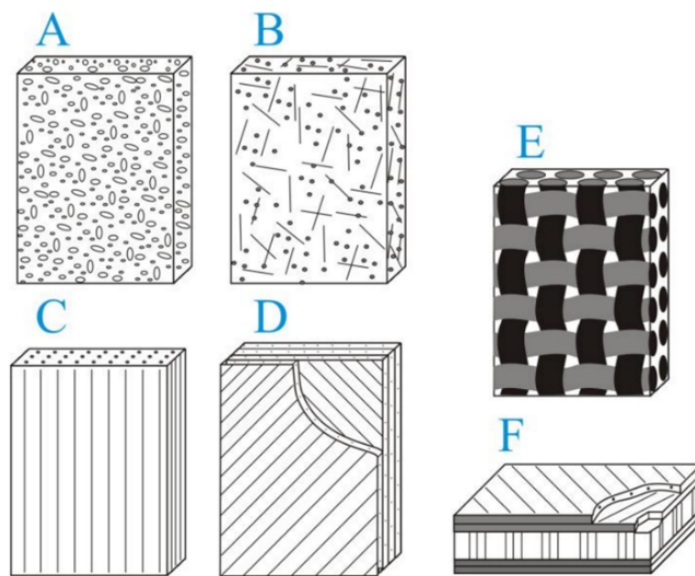


Figure 1.3 Emerging composite materials: (a) reinforced by particles, (b) reinforced by chopped fibres, (c) unidirectional, (d) laminates, (e) woven reinforced plastic and (f) honeycomb sandwich [10].

The reinforcement of carbon fibre can be in many forms depending on demanding mechanical properties [10], demonstrated in Figure 1.3 from simple to advanced structures. The particle and chopped fibres reinforced composites (see Figure 1.3(a) and (b)) gain in stiffness but less effective than the unidirectional and laminated fibre reinforcement types shown in Figure 1.3(c) and (d). However, the advantage of the particle and chopped types is their simplicity and low manufacturing cost. Shown in Figure 1.3(f), the honeycomb sandwich composites have the combined properties of high stiffness and low structural weight. The honeycomb core is usually made of metal or polymer to resist shear stress. The sandwich skins are usually made of aluminium or fibre reinforced plastic to resist tensile and compressive stresses. Finally, the woven reinforced plastic demonstrated in Figure 1.3(e) give highest strength and are the most complex composite, consisting of fibre yarns in weaving/braiding architectures embedded in the plastic matrix. It has better properties of stiffness, strength and anti-delamination (due to z-

binders). Due to their complicated structures, inspection of woven carbon composite is currently one of the most challenging NDT&E applications.

In order to overcome these challenges in NDT&E of steel under coating/insulation and the woven carbon composite, this work provides an investigation on multilayered models of these structures. Based on literature review detailed in Chapter 2, microwave NDT technique has been selected, over other NDT techniques (e.g., Ultrasound, Eddy current, Thermography, etc.), due to its excellent penetration properties in dielectric material with total reflection on conductive surface, making it ideal for inspection of steel corrosion under coating and defects within polymer composites. Moreover, microwave reflected signals (reflection coefficient) are sensitive to EM properties (i.e., permittivity and permeability) of material, which is suitable for inspection of woven carbon fibre reinforced plastic. However, the challenges of microwave inspection are the complex analysis of electromagnetic wave interrogation and the great amount radio frequency (RF) and environmental interferences (e.g., the layer interface causing multiple reflections) in the measurements. In the next section, the aim and objectives of this research are outlined in the following subsection to tackle these problems.

1.2 Aim and Objectives

The aim of this project is to design and develop a microwave NDT&E system for imaging and evaluating defects in multilayered structures of corrosion under coating, woven carbon fibre composites, and glass fibre pipes.

The research objectives are summarised as follows:

- To design and implement Microwave NDT&E scanning system using open-ended waveguide (OEW) probes for multilayered structures. The X-Y scanning resolution should not be lower than 0.5 x 0.5 mm as it is required for inspection of woven carbon composite texture. Though, the image resolution can be later improved by SAR signal processing technique. The operating frequency is limited by the VNA and commercially available probes, in range between 8GHz to 26.5GHz.
- To investigate the potential feature extraction and characterisation of early steel corrosion (0-12 months) based on microwave responses at X (8-12GHz), Ku (12.4-18GHz) and K (18-26.5GHz) bands of dedicated corrosion sample.
- To investigate the potential feature extraction of low energy impact damages (ranging from 2-12 Joules) on woven carbon fibre composite. The selected feature extraction method should eliminate the interference of the fibre texture and be able to detect and visualise the defect of impact damage at 4 Joules.

- To demonstrate the capability of microwave NDT&E scanning system to evaluate flat-bottom hole (FBH) defects resided underneath curved glass fibre composite pipes. The system should be able to evaluate the FBH at 11.5mm depth.

1.3 Research Scopes

In this project, experimental approaches are undertaken to investigate the microwave NDT&E system with dedicated samples. Multilayered models and their parameters (i.e., geometric and electromagnetic properties) are analysed based on scenarios of structural deterioration and/or changes in the chemical or mechanical process to understand the relationship between the model parameters and their responses. Further feature extraction methods are exploited to determine the capability of the microwave NDT&E system for detection and characterisation of the defects and layer properties within the multilayered structures.

Three types of real-world dedicated samples are designed and studied: early stages of steel corrosion undercoating (0-12 months), woven carbon composites with low impact damage (0-12 J) and glass fibre composite pipes with internal flat-bottom holes up to 11.5 mm depth. The steel corrosion samples are initially made by exposing a set of mild steel plates to the marine atmospheric environment with various exposure time periods: 1, 3, 6, 10 and 12 months. Then, the corrosion samples were painted by a thin coating layer resulting in corrosion under coating samples, which are modelled by two homogenous dielectric layers backed by a metallic plate. The impact damages on commercial woven CFRPs are made by dropping a round-headed hammer with diameter of 20 mm at various heights producing low energy at 2J, 4J, 6J, 8J, 10J and 12J. The drops generated various types of impact defects on the sample surface and within the CFRP laminate structures. The last sample is a GFRP pipe, flat-bottom holes are made by machining on the inner surface of the dedicated sample with various depths: 4.0, 5.5, 8.0, 11.5 mm.

The initial stage of the project is the feasibility study. The responses of the prepared samples obtained by the developed microwave NDT&E system are observed for the possibility to be characterised or quantitatively evaluated by the monotonic or linear relationship to the controlled parameters of the samples. Samples with the homogenous layered, like steel corrosion, is usually measured by only a single probing (A-scan) at the centre of the material patch. Composite samples with area defects such as woven carbon composite with impact damage require an area scan (C-Scan) to form an image. Then, the data obtained from each sample are analysed for the potential features reflecting the interesting properties of the samples.

In case that an analytical model is not provided by literature, numerical simulations with simplified models are carried out to study the influences of the interesting parameters based on the theory and hypothesis of changes in materials caused by defect or deterioration process. The simulation results are compared with the results of the preliminary experimental study. Due to the complexity of the real-world sample with uncertainty of measurement environment, it is not expected that both simulation and experimental results are precisely matched, but the trends of both results should agree with each other.

In experimental studies, measurement data are carried out from the dedicated samples within the controlled measurement environment. Then, the obtained data are analysed based on the potential feature extraction methods. The feature values calculated by feature extraction methods are compared with the experimental controlled parameter of the samples. The feature extraction method having its values most correlated to the controlled parameter (typically monotonic characteristic) will be selected for the quantitative evaluation of the samples. In addition, experimental results of previous works applying different technique with the same sample will be compared and discussed.

1.4 Major Achievements

The significant achievements of establishing the microwave NDT&E system are supported by thesis chapters and the following journal and conference publications.

- The system design and implementation of microwave NDT&E system using open-ended waveguide have been carried out based on challenges/problems identification of NDT techniques for multilayered structures. The scanning resolution of 0.1 x 0.1mm can be archived. The system has been used to investigate in publications [11]–[16].
- A model of steel corrosion is exploited as layers of homogeneous dielectric backed by perfect conductive plate. The early corrosion stages, from 0-12 months, of steel corrosion under coating have been successfully characterised by the first principal component. It is also found that the PC1 features are independent of probe operating frequency and coating properties. This work has been published in [11].
- Numerical simulation of simplified woven CFRP models, which are inhomogeneous carbon/plastic composite with different weaving structures and multiple layers has been carried out. The experimental study for the optimal measurement parameters (i.e., scanning step size and lift-off) and fibre/impact damage visualisation have been conducted. A PC based feature has been used to represent the impact damage at different impact energies (from 2-12 Joules of impact energy). The visualisation of low impact

damage at 4 Joules can be archived with the elimination of woven texture influences. These works have been published in [12] and [13].

- A model of curved dielectric layers of glass fibre is exploited. The area of the sample is scanned with variations of lift-off due to the curvature of the pipe surface. PCA and SAR tomography have been successfully utilised for detection and quantitative evaluation of flat-bottom holes (depths between 4.0 – 11.5 mm). The deepest FBH (at 11.5 mm) could be localised and evaluated by the proposed technique. This work has been published in [14].

1.5 Research Methodology

The research carried out in this thesis involves the experimental investigations of microwave NDT&E system for multilayered structure with the three dedicated multilayered models. The primary concern in the development of microwave NDT&E system is to configure commercially available microwave devices tags to obtain responses from three types of samples (i.e., corrosion under coating, woven CFRP with impact damage and coated GFRP composite with inner FBH defects). Signal processing and data analysis methods including feature extraction, visualisation, and quantitative evaluation, are carried out to identify and extract meaningful features out of it. Finally, the results are validated with the controlled parameters of the samples and/or with the results of other related works using the same samples. A summary of these are shown in the subsequent sub-sections and these are detailed in the research methodology diagram presented in Figure 1.4.

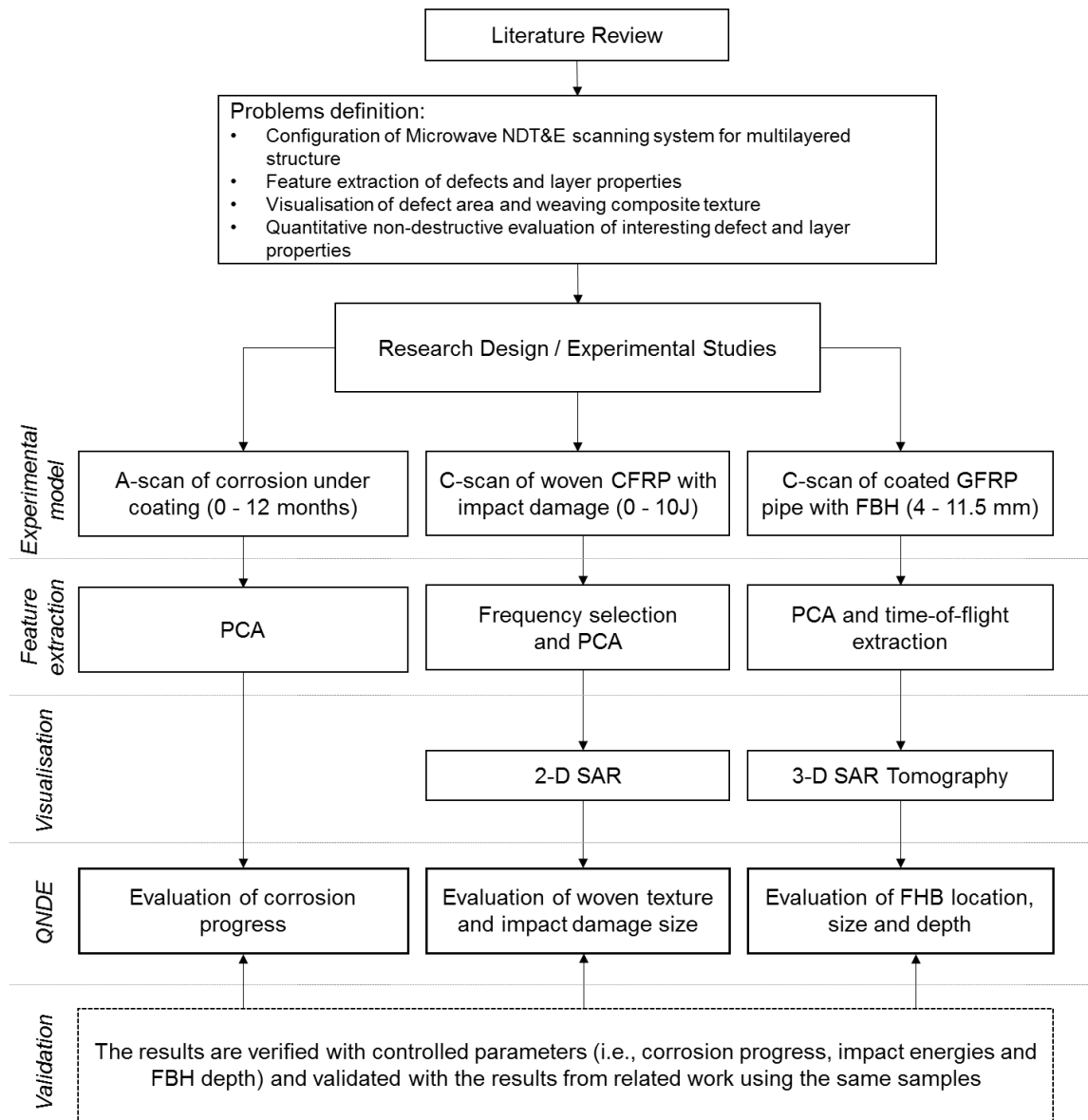


Figure 1.4 Research Methodology

1.5.1 Study 1: Steel corrosion stages characterisation

The experimental study of a steel corrosion stages characterisation method using microwave open-ended rectangular waveguide probes are outlined. Datasets are obtained from sets of coated and uncoated corrosion progression (0 - 12 months) samples, in the form of reflection coefficient spectra (from 9.5 to 26.5 GHz). A statistical-based PCA method is applied for corrosion feature. The robustness of the PC-based features is analysed with influences of operating frequency, coating layers and surface condition. The results are verified by the relationship between corrosion feature and sample controlled parameters (i.e., the corrosion progress from 0 – 12 months) and comparison with the previous work of other methods using the same samples.

1.5.2 Study 2: Detection of impact damage on woven CFRP composites

This work presents a novel framework for feature extraction of impact damage on woven composite based on PCA of spectral responses. Simplified models of woven carbon composites are preliminarily studied based on numerical simulation. The near-field reflection coefficients of CFRP samples with impact damages (0 - 10J) are obtained by performing C-scan using open-ended waveguide probe in K-band. To improve visualisation and eliminate the spatial distortion caused by probe lift-off, the near-field spatial-spectral signals are then preliminarily corrected in the frequency-wavenumber domain using 2-D SAR algorithm. PCA is applied to analyse the impact damage feature and reduce dimensions and redundancy of the spectral responses for the image formation. The results are verified by visual image for fibre texture and the correlation between the defect size and the controlled parameters (i.e., the impact energy 0 - 10 J) for the impact damage characterisation.

1.5.3 Study 3: Detection and evaluation of flat-bottom holes in coated GFRP pipe

This study proposes a novel microwave NDT application to detect and characterise internal defect; i.e., flat-bottom holes in coated GFRP pipes. Initially, responses of four FBH areas obtained by microwave open-ended waveguide probe are analysed using PCA to reveal FBH defect and eliminate the pipe curvature influence. Following that, SAR tomography images are produced to select the corresponding principal component and verify the location of FBHs. FBHs are quantitatively evaluated using PC feature and SAR tomography including time-of-flight feature. The depths of FBHs are characterised by analysing the time-of-flight feature of background-subtracted responses. Finally, the results are verified based on controlled parameters of FBH samples (i.e., location, size and depth).

1.6 Thesis layout

In this chapter, so far, project background, aim and objectives, research scopes and major achievements have been described. The rest of this thesis are organised as follows.

Chapter 2 presents the literature survey of microwave and other related NDT&E methods for inspection of multilayered structures. Advantages and disadvantages of each NDT&E method are discussed. Finally, the challenges of microwave NDT&E for multilayered structures are identified.

Chapter 3 presents the theoretical background of microwave open-ended waveguide, models of dedicated corrosion and composite samples, design and implementation of microwave NDT&E system. Finally, the research methodology, which outlines the research investigations, are presented.

Chapter 4 outlines the experimental case study 1: characterisation of steel corrosion stages. The model of corrosion progression and open-ended waveguide measurement mechanism are presented. Details of the experimental setup and the dedicated corrosion samples used in this work are explained. Finally, the results are discussed and summarised.

Chapter 5 elaborates the experimental case study 2: detection and characterisation of impact damages on woven CFRP. This chapter begins with a simulation study of the simplified carbon composite models. The simulation results are discussed and compared with the preliminary study of the microwave responses of impact damage. Following this, feature extraction of impact damage is studied. The results are analysed for impact damages evaluation and conclusions are made.

Chapter 6 presents the experimental case study 3: detection and quantitative evaluation of GFRP pipe with flat-bottom holes. Firstly, a model of glass fibre pipe with flat-bottom holes is discussed. Next, experimental setup and dedicated glass fibre pipe sample are explained. Following by experimental study and data analysis based on PCA and SAR tomography methods. Finally, the quantitative evaluation of defects is presented with a summary of the work.

Chapter 7 summarises the findings from the research work and outlines the potential future work.

1.7 Chapter Summary

This chapter presents a brief introduction to the research work. The background of NDT&E challenges of multilayered structures includes corrosion under coating and carbon/glass fibre composites. The selection and motivation of microwave open-ended waveguide technique are generalised and explained based on previous literatures. Four objectives include (1) system design and implementation, (2) steel corrosion stages characterisation, (3) investigation of impact damage on CFRP and (4) quantitative evaluation of FBH in GFRP pipe, are identified with detailed specifications and related publications. The research methodology discusses a summary of three case study scenarios of microwave NDT applications. Finally, the summary of this thesis structure from chapter 2: literature review, chapter3: methodology and chapter4-6: three major contributions and chapter 7: summary are outlined.

Chapter 2 Literature Review

Following the introduction to the thesis in the previous chapter, this chapter presents a literature review on the common NDT techniques used for multilayered structures, microwave NDT methods using open-ended waveguide probe with specific challenges of multilayered materials, and the identification of challenges in microwave NDT.

2.1 Review of NDT&E Approaches for Multilayered Structure

In recent few decades, compound materials, made of layered dielectric/conductive laminates have found their applications in many sections including civil construction, aerospace, and oil and gas pipeline. These materials are usually composed of layers of homogeneous coatings such as layers of paint/primer, thermal barrier and insulator. The core material can be made of layers of the inhomogeneous composite such as a carbon/glass fibre reinforced polymer. In laminate composites, these layers are bonded together using thin layers of adhesive resulting in a laminated structure. Advanced composites can be also in the form of the woven structure of weft and warp fibre yarns. Detection and evaluation defects within these composites are challenges for common NDT&E methods [17]–[19]. Hence, in the following sub-sections, reviews and comparison of various NDT&E approaches for these multilayered structured are presented.

2.1.1 Eddy Current Testing

The principle of the eddy current testing (ECT) is based on the interrogation between an excitation magnetic field (100 Hz to 4 MHz) and material under test inducing an eddy current in the sample. The presence of small defects can be revealed by observing changes in the secondary magnetic field related to the flow of eddy current. Unlike other magnetic methods, ECT allows detection of defects within various types of conductive materials including ferro- and non-ferromagnetic.

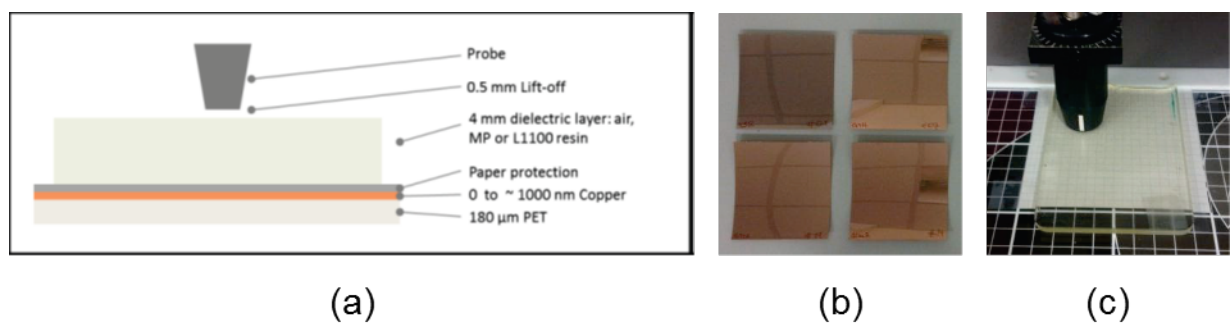


Figure 2.1 High frequency ECT measurement (a) stacked layers, (b) copper coated PET samples, (c) measurement operation [20].

Development of pulsed eddy current (PEC) enabled the technique measure layer thickness of non-conductive material such as coating and corrosion [21], [22]. High frequency ECT [20] is also applicable for non-conductive composites, where the impedance matching between the probing coil and the permittivity of the sample contains useful information such as local permittivity variation of copper coated PET samples demonstrated in Figure 2.1. The spatial resolution of high frequency eddy current was improved by the study [23] using a metamaterial lens realised with two conical Swiss rolls. Moreover, due to the capability of ECT for conductivity and permittivity mapping, an automated 3-D visualisation of fibre orientation in woven CFRP laminates (both surface and near sub-surface) are done by means of further signal processing [24].

The significant challenge for ECT method is the lift-off variation, which is normally caused by a thick dielectric coating or an irregular shape (non-flat) of the test sample [25]. Lift-off can be regarded as noise that conceals the responses and reduces sensitivity to the defects. One may overcome the problem of curved samples by utilising an automated scanning system (e.g., a robot arm) [24] to maintain a constant gap between the probe and sample.

2.1.2 Ultrasonic Testing

Ultrasonic testing (UT) is a standard method for defect detection and obtain layer thickness of the material under test based on discontinuities in density and stiffness within the material [26]. Significant advantages of UT are one side accessing and high accuracy of localisation and estimation the size and shape of the defect within high-density materials such as steel and alloys. An ultrasonic transducer transmits a high-frequency acoustic pulse (0.5 to 15 MHz) propagating in solid or liquid materials [27]. The backscattered waves from any discontinuity inside the material are captured by one of three system setup configurations: (1) pulse-echo, (2) pitch-catch or (3) through transmission.

The conventional UT technique requires liquid couplant (water or gel) to be placed between the probe and the sample surface to achieve high sensitivity. To overcome this challenge, laser ultrasonic testing had been developed as a non-contact method reducing scanning time and complexity [28]. However, it is relatively expensive, and its performance is strongly affected by the surface condition. Another interesting non-contact ultrasonic method is electromagnetic acoustic testing (EMAT) [29]. EMAT utilises electromagnetic-acoustic transducers to excite long radio-frequency bursts generating eddy currents in the metal sample. The presences of defects are detected by variations in the reverberating signals. EMAT does not require contact with the surface and hence enabling inspection of extremely hot and cold slab surface.

In ultrasonic NDT for multilayered structure, the delamination between reinforcement and the surrounding concrete was investigated in [30]. This system effectively detected the separation of the steel bar concrete interface of corroded and non-corroded specimens using the combination of a piezoelectric zirconate-titanate transducer (PZT) and an EMAT. In aircraft composite structures, the UT inspection of pitting corrosion of rivet in aircraft complex multilayer structure had been presented [31]. Figure 2.2 shows the configuration of UT scanning system and the dimensions of the rivet sample. The UT system composed of UT probe mounted on XYZ scanner, which is controlled by a computer. The Pulser/Receiver generates pulses and retrieve echoes and transform them to digital signal through the digitizer. The B-scan signals of the rivet sample with scanning step size of 0.5 x 0.5 mm were analysed using short-time Fourier transform (STFT) for crack detection and estimation of crack depth. Also, a high frequency ultrasonic method using 125-MHz piezoelectric transducer and wideband laser-ultrasonic demonstrated the measurement of internal corrosion [32]. However, only the corrosion layer thickness was conclusively revealed by this method due to their difference in mechanical parameters.

The major limitations of the UT methods are the requirement of an accessible surface of the test material and it is not suitable for materials with a rough surface, irregular shape, small, thin and inhomogeneous.

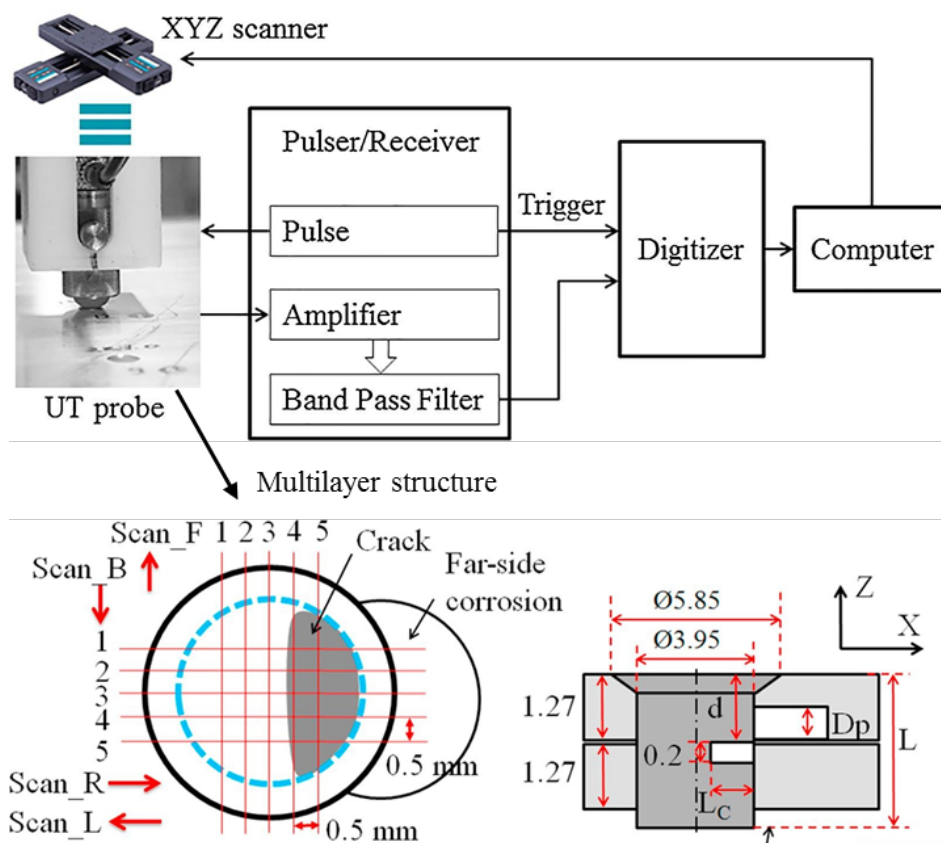


Figure 2.2 UT System and multilayer rivet sample [31].

2.1.3 Thermography

Thermography or infrared (IR) thermography has shown the capabilities of quick, good image resolution and high sensitivity for inspection of defects based on the contrast in heat conductivity. There are two significant types of thermography: passive and active. Presented in Figure 2.3, both passive and active thermography use IR camera to capture heat pattern from test object. However, the active thermography excites a sample with choices of heat excitation sources including light, eddy current, laser, microwave and ultrasound, making it capable for wider NDT applications [33], [34].

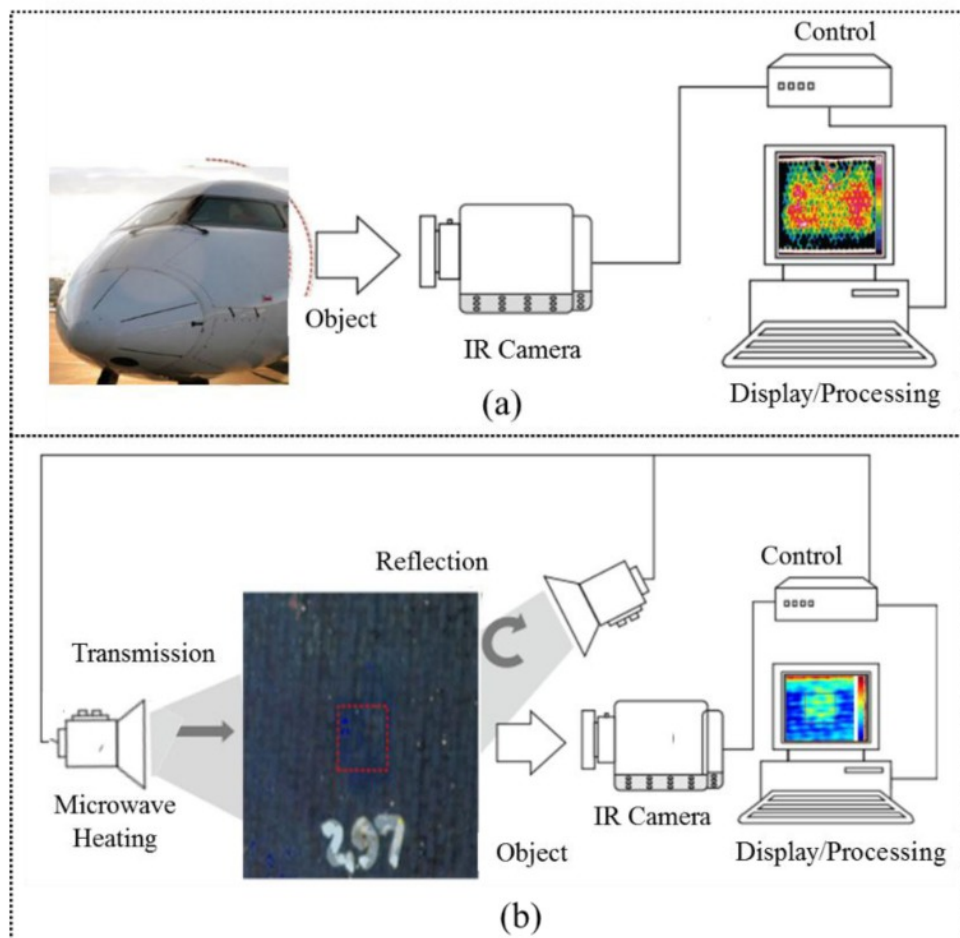


Figure 2.3 (a) passive thermography and (b) active thermography (microwave source) [35].

Active thermography methods are common methods for inspection of composite structures [33], [35]–[38], in particular, aerospace composites [36], [39]–[41]. Typical defects include cracks, impact damage, delamination, matrix/fibre cracking, voids and core crushing. The active thermography can be categorised into two major methods: optical and non-optical [33]. In optical tomography, pulsed thermography (PT) [42] employs a very short duration (0.1 to 50 ms) of flashing pulse on the sample and uses IR camera to capture the temperature gradients from the sample surface. Lock-in thermography (LT) [43] uses a periodic heat excitation to

generate thermal waves within the sample. The variations in temperature are captured by IR camera, magnitude and frequency of the obtained signals are analysed using Fourier transform. Long pulse thermography (LPT) [37] uses the longer heating time to enable defect detection at the deeper range. Although these optical thermography methods show good results for the surface defect, the heat from optical sources is usually limit within a few millimetres from the surface.

In non-optical tomography, ultrasonic thermography (UST) generates strong vibrations causing frictional heat at the crack surfaces of material [44]. However, it requires high-power, contact of ultrasonic transducer that may produces complex wave propagation, and thus complicated heating pattern and further signal analysis. Eddy current pulsed thermography (ECPT) uses electromagnetic waves from the primary coil to induce eddy currents in a conductive sample and IR camera to capture the induction heat at the sample surface [22], [45], [46]. Depending on the defect depth and conductivity of the material, excitation frequency can be varying between 150 to 450 kHz with the pulse duration of a few milliseconds (for material with high conductivity) to a few seconds (for material with low conductivity). Nevertheless, the detectability of ECPT is usually limited by the effect of complex and non-uniform heating as well as the low conductivity of the testing material. Microwave thermography (MWT) [47], [48] emits microwave energy to generate heat based on dielectric loss within the material. It has unique advantages such as high heating power efficiency and uniform volumetric heating pattern. However, the high power radiation of microwave heating system may affect the integrity of equipment, particularly, within the aerospace structures.

2.1.4 Radiography

Conventional radiography uses an X-ray beam to penetratingly scan the internal structure of materials and forms a 2-D cross-section image [49]. The image of X-rays is presented by changes in electron density along the beam direction. For advanced 3-D scan, X-ray computed tomography (CT) relies on 3-D computation of X-ray image series obtained from rotating the sample [50]. The output 3-D volume is corresponding to the contrast between the attenuation coefficients (as a function of density) of the material. The high resolution volume obtained provides both qualitative and quantitative information in microscale, mesoscale and macroscale.

In NDT applications of multilayered composite structures, conventional radiography has been demonstrated the capability to detect crack and delamination in glass fibre composite laminates [51]. In some cases where the atomic number of fibre and matrix are relatively close to the defects, a dye penetrant liquid was applied to improve the contrast in the interesting area [52]. By means of X-ray CT scan, the 3-D images of time-dependent corrosion morphology of rebar

in the marine environment are revealed with certain corrosion parameters (see Figure 2.4) [53]. Moreover, the X-ray CT has the capability to scan a large object such as a segment of turbine rotor blade in a CT volume of around $3.5 \times 3.1 \times 1.1 \text{ m}^3$ [54]. The internal structure including orientations of fibre and defects were clearly unveiled. In the studies of fibre composite in microscale [5], [55], [56], micro-CT has demonstrated the capability for the characterisation of damage and internal flaws, including delamination and microcracking in fibre/matrix composites.

The main disadvantages and limitations of X-ray methods are costly, exposure hazard and high computational power required to interpret the volumetric data. Moreover, CT scan of a sample with low-density such as plastic composites may not give good results with adequate contrast and resolution for quantitative analysis.

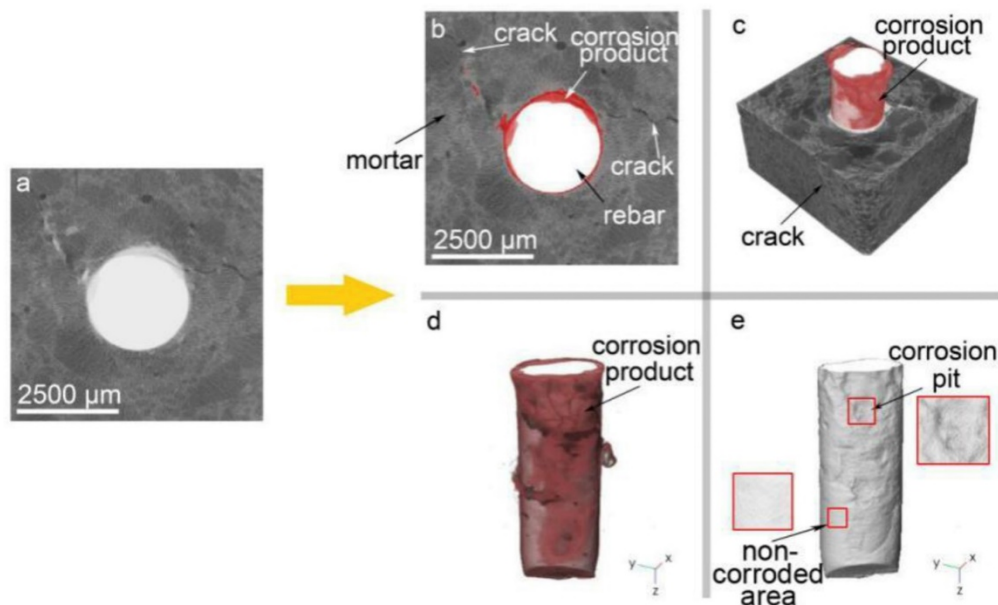


Figure 2.4 Images obtained from XCT measurement include original sample slide and corrosion products [53].

2.1.5 Microwave and Millimetre-wave NDT

Microwave and millimetre-wave transmit high frequency electromagnetic waves (range of 300 MHz to 300 GHz) penetrating through dielectric layers and interrogating to the internal structure of materials [38], [57]. Demonstrated in Figure 2.5, the interrogated signals are affected by the variations of the thickness and permittivity of each layers, which store energy within their layer. Microwave and millimetre wave methods have been applied in many NDT applications include material characterisation [58]–[60], detection and sizing (dielectric thickness) [61]–[63], crack and sizing on metal surface [64]–[66], corrosion undercoating [67]–[69], composite delamination [70], [71] and structural imaging [72]–[75].

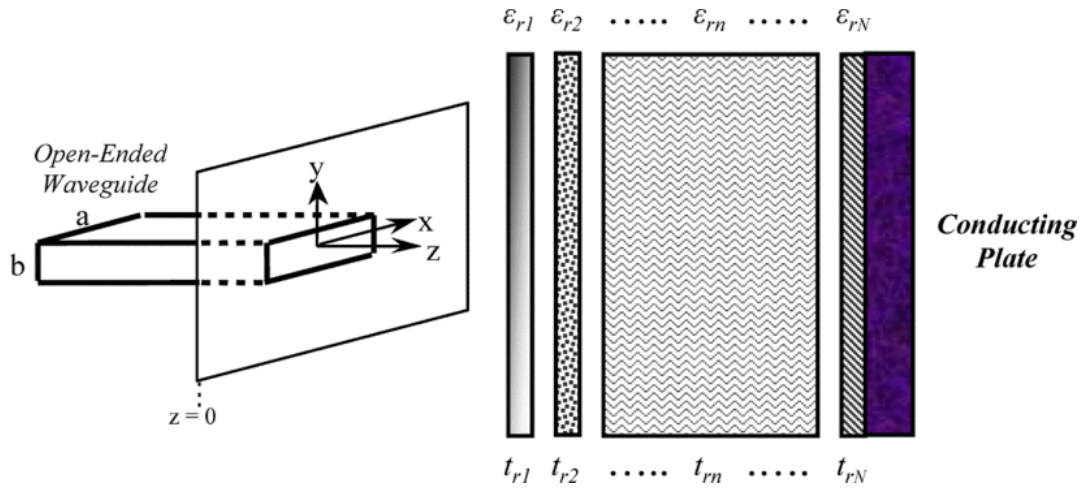


Figure 2.5 A microwave open-ended rectangular waveguide radiating into an N -layer structure backed by conducting plate [76].

Microwave NDT approaches of layered composites can be recognised in three categories, which are self-sensing, near-field and far-field methods. In self-sensing methods, the surface and near-surface damages in CFRP were characterised through a layer of GFRP based on characteristic impedance changes using time domain reflectometry (TDR) technique [77], [78]. This technique locates discontinuity in the material by reflected signals in the time domain. However, it is not suitable for practical application since the probe and sample is inseparable. A technique using an independent microstrip line where the CFRP sample is separated from the measurement probe was proposed in [79]. It allows smaller microstrip probe to perform B-scan over the large composite sample.

In near-field methods, a monostatic configuration of the antenna or open-ended waveguide probe is used to emit microwave or millimetre wave signals to the sample within the vicinity of antenna/probe aperture (see Figure 2.5). The reflectivity or reflection coefficient is usually obtained and analysed for defect detection and structural imaging. The application of fibre orientation detection of CFRP surface ply was demonstrated in [80], [81]. The fibre direction can be detected by the response from the interrogation of the electric field and anisotropic conductivity of carbon fibre at different directions. Strain or deformation of CFRP composite has been studied using reactance calculated from the received signals based on the relationship between carbon fibre links represented by resistance and inductance and the air gap represented by a capacitance [82]. In damage detection, the near-field microwave has demonstrated the capability to detect impact damage and delamination of multilayer CFRP laminates [83], [84]. The detectability of impact damage at an impact energy of 8.89 J of CFRP composite was reported in [85]. This technique performed a C-scan over the sample with horn antenna operating in the frequency range between 65-67 GHz. A low-cost complementary split-ring resonator (CSRR) based on printed-circuit-board (PCB) coils was developed in [86]. The

impact damage of CFRP composite is revealed by the resonance shifted upward in the impact region.

In far-field sensing methods, a pair of antennae is commonly used. A transmitting antenna can be either bistatic or monostatic configuration. Bistatic configuration requires a pair of transmitting and receiving antennae with excellent isolation between channels, whereas monostatic configuration requires a circulator to separate between transmitting and receiving signals. The system configuration and applications of far-field microwave NDT is similar to that of ground penetrating radar (GPR) system [87]–[89]. Hence, the NDT applications of far-field methods cover in extensive sensing applications including geology, archaeology and civil engineering. It has demonstrated the capability for detecting and imaging of hidden structures such as utility mapping [90], railways structural layers [91], [92], and archaeological site exploration [93].

The disadvantages of microwave and millimetre wave are skin depth effect preventing signals propagating into conductive materials, and high cost equipment (e.g., vector network analyser) which its price depends on operating frequency ranges. Moreover, there is also the challenge of microwave and millimetre-wave NDT complex electromagnetic signal processing and the unwanted background signals caused by transmit/receive coupling, multipath scattering, and other electromagnetic interferences in the surroundings.

2.1.6 Comparison of NDT approaches for Multilayered Structures

The reviews of NDT&E methods for the multilayered structure are compared and presented in Table 2.1. It provides a comprehensive comparison of different techniques including their characteristics, advantages and disadvantages when inspecting different type of materials with multilayered structures. NDT techniques such as ultrasonic and X-ray perform best in solid and high-density layers (e.g., metal), while microwave and millimetre-wave demonstrate better sensitivity in low loss dielectric (e.g., glass, wood and plastic). Some techniques may perform in testing better than others but limited by certain constraints and conditions (e.g., one side access, long stand-off and high-speed). Moreover, the data obtained from the measurement are usually further analysed qualitatively and quantitatively. The responses from techniques that contain richer information (higher data dimensions) are usually delicate to unwanted background noise and uncorrelated influences. Thus they typically require more advanced signal conditioning and signal processing with high computational power. Finally, the factors of portability, cost and time efficiency should also be taken into account.

Table 2.1 Advantages and limitations of various NDT&E methods for multilayered structures

Method		Characteristics detected	Advantages		Limitations
Eddy current testing	ECT	Permeability and conductivity	Sensitive to surface defect (e.g., crack)	Quick and suitable for conductive materials	Low penetration depth at high frequency and lift-off attenuation
	PEC			Depth information can be extracted from the response	High current pulse generator and high-speed data acquisition are required
Ultrasonic testing	UT	Density and stiffness	One side; detect defects within thick sample	Various operation modes	Use of liquid couplant; not for rough surface
	EMAT			Dry and non-contact	Low energy conversion efficiency
Thermography	Optical	Thermal conductivity and thermal capacity	Quick and high stand-off distance	Uniform heating	Low penetration depth
	Non-optical			Heat is generated within the materials	Non-uniform and/or complex heating generation
Radiography	X-ray	Electron density	High resolution images in micro and macro scale	2-D high resolution image	Not good for low density material; radiation safety precaution; very expensive
	CT			3-D visualisation of the internal structure	High computation power is required; need a rotating platform
Microwave and Millimetre-wave	Near-field	Permittivity and permeability; totally reflected for a conductor	Low loss in dielectric; high resolution (depending on wavelength)	Suitable for material characterisation (resonance)	Complex electromagnetic analysis due to the curved near-field wavefront
	Far-field			Suitable for targets/layers localisation (time feature)	High attenuation in lossy materials; antennae coupling effect; strong interferences

2.2 Microwave NDT using Open-ended Waveguide Probe

According to the literature reviews and summary in Section 2.1, microwave and millimetre-wave NDT have proven to be ideal methods for inspecting multilayer dielectric structures including material EM properties characterisation, delamination of layered structures, and visualisation of internal structures. In near-field microwave NDT applications, open-ended waveguide probes are the standard tools to measure reflection responses from its aperture as a function of permittivity and geometric shape of the sample under test. Figure 2.6 demonstrates the example applications of open-ended waveguide probe for inspection of a layered GFRP pipe and a CFRP composite under coating.

The studies of microwave and millimetre-wave NDT using open-ended waveguide probe usually have considered the case of radiation into an infinite half-space of a dielectric material. In a study of microwave NDT&E for a homogenous-layered structure, a material is considered as being infinite and fills the half-space $z > 0$. Teodoridis et. al [94] introduced three basic configurations of material models for open-ended waveguide operation as demonstrated in Figure 2.7. The first model shown in Figure 2.7(a) is applied when the material losses and thickness are large enough and the wave diffracted from the aperture is absorbed entirely without further reflection. The second model shown in Figure 2.7(b) is applied when material losses are small, a dielectric slab is terminated by a metallic plate to enhance the reflection coefficient. The last model shown in Figure 2.7(c) considers a material as a stratified structure with finite thickness and unterminated.

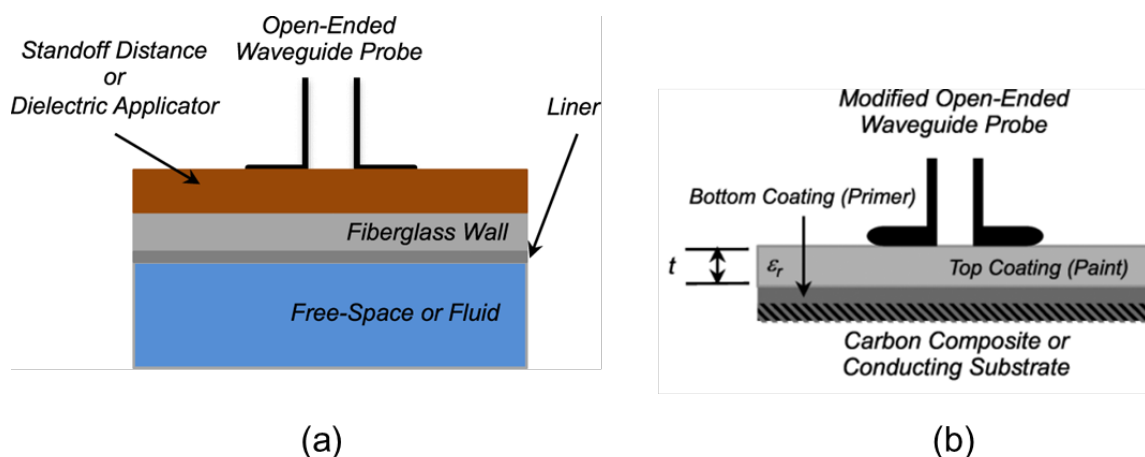


Figure 2.6 (a) a fibreglass pipe or tank inspected by an open-ended waveguide probe [95] (b) a modified open-ended rectangular waveguide probe radiating into a two-layer coating (i.e., paint and primer) with conducting substrate (carbon composite) [96].

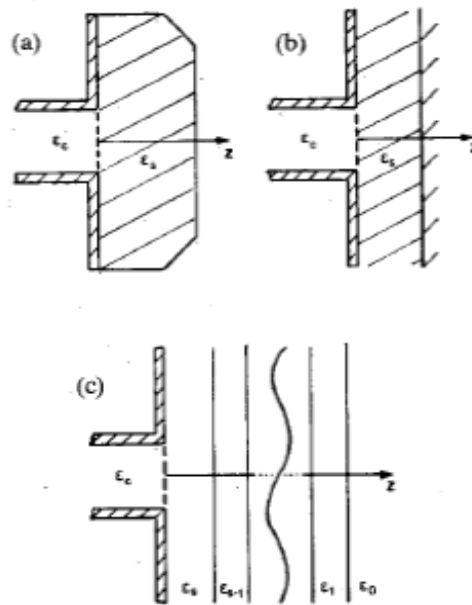


Figure 2.7 Three basic configurations of dielectric medium (a) infinite thickness, (b) finite thickness terminated by a metallic plate and (c) finite thickness and unterminated, yielding a stratified structure [94].

Many studies have developed electromagnetic formulations for both cross polarization and higher order modes including integration [63], [97], matrix correlation [98], [99] and method of moments [100], [101]. Although these rigorous formulations are essential for the accuracy of the inverse calculation of low permittivity and low loss dielectric medium, the contributions of those formulations have not always been considered as presented in [102]–[104]. This calculation simplification provides computational efficiency with sufficient accuracy results and applicable for many practical NDT applications.

2.2.1 Non-destructive Evaluation of Steel Corrosion under Paint

Although more works have unveiled the layer properties with the improvement of measurement techniques, estimation of the steel corrosion progress under coating is still a challenge since its properties including thickness and chemical compound are varying over time [105]–[107]. Moreover, the characteristic of corrosion are a complex function of multiple variables such as oxygen content, pH, biological activity and pollutants. Melchers [108] defined phases of uniform corrosion with time relationship as demonstrated in Figure 2.8(a). Phase 1, concentration control of corrosion is modelled as a linear function in which iron molecules are changed to various forms of ferrous hydroxides as electro-chemical reactions [109], [110]. The rate of reaction is also a function of surface roughness and the dissolved oxygen content. It is known that the phase 1 will continue to govern until such time as the rate of oxygen supply becomes sufficiently inhibited by the gradual build-up of corrosion products. Phase 2, diffusion controlled corrosion has been firstly modelled by Tamman [111] for uniform density

atmospheric corrosion. Copson [112] followed by adapting using experimental observations. The corrosion is estimated by the function

$$c(t) = At^B \quad (2.1)$$

where t is an exposure period, A and B are constants describing the complete observed corrosion-time behaviour. The value of B had argued to be 0.5 by studies of Tammann [111] and Evans [109] for a uniform corrosion product.

The debatable studies of corrosion sublayers are found in the case of weathering steels [107]. In the first model, study in [113] proposed that the corrosion generally consists of two layers: the inner layer consisting of amorphous FeOOH and crystalline Fe_3O_4 ; the outer layer consisting of loose crystalline $\alpha\text{-FeOOH}$ and $\gamma\text{-FeOOH}$ as presented in Figure 2.9(a). The second model is the nonexistence of a layered structure on mild steel as presented in Figure 2.9(b). The last model is endorsed by studies in [114], [115], the corrosion sublayers usually consist of three layers: the inner layer, and two outer layers as presented in Figure 2.9(c).

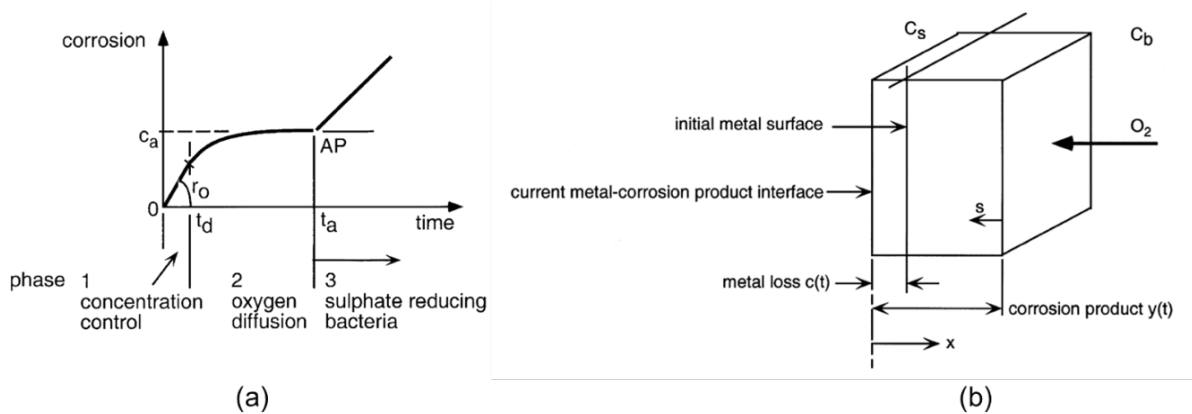


Figure 2.8 (a) uniform corrosion-time relationship (b) illustration of uniform corrosion product.

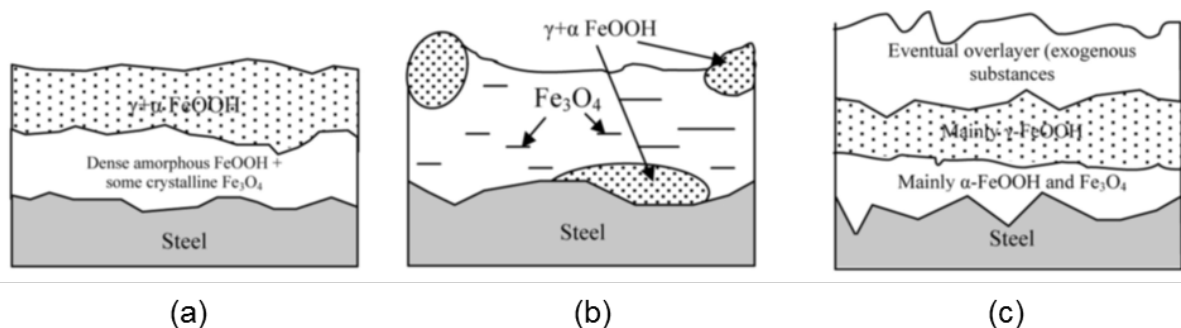


Figure 2.9 The different models of corrosion sublayers (a) two layers, (b) no layer and (c) three layers [107].

Regarding the layered structure of corrosion under paint, the model of dielectric slab backed by a metallic plate is commonly used in the corrosion studies of microwave and millimetre wave NDT [57]. It is noted that the similar models can also be applied to an investigation of corrosion on aluminium substrates [67], [116]. Kharkovsky and Zoughi [68] investigated a sample of corrosion patch produced in a salt fog chamber. The sample shown in Figure 2.10(a), has a total thickness of primer and paint of 0.126 mm. Reflectometer system using an open-ended rectangular waveguide probe with different operating frequencies is utilised for investigating in the sample. Due to the fact that the thickness of the corrosion layer was relatively thin, the low frequency band of microwave and millimetre waves could not reveal good results. However, at higher frequencies of V-band (70 GHz), the results show Figure 2.10(b) could clearly reveal the images of the corroded area with details of non-uniform distribution of small pitting. In the corrosion study by Qaddoumi et al. [116], a reflectometer with open-ended rectangular waveguide probe was used to obtain the phase of reflection coefficients over the coated corrosion samples. Thicknesses of coating and corrosion layers were estimated from phase responses at a specific frequency. However, the prior knowledge of corrosion and coating properties are required for the estimation.

As the development of multilayered electromagnetic formulations, Ghasr et al. [14] introduced a full-wave accurate model and iterative inverse technique for estimating the complex permittivity and thicknesses of dielectric layers. It has shown good accuracy in thickness evaluation of lined-fibreglass [95] and the coating layer of carbon fibre composites [96]. Although these near-field microwave NDT&E methods have demonstrated the capability for detection and corrosion under paint [117], to date, there is no comprehensive study related to the quantitative evaluation of corrosion progression versus exposure time with complex shifting in the corrosion layer properties.

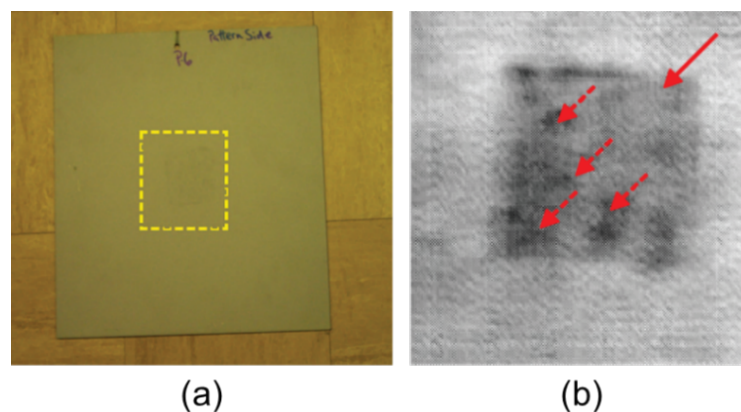
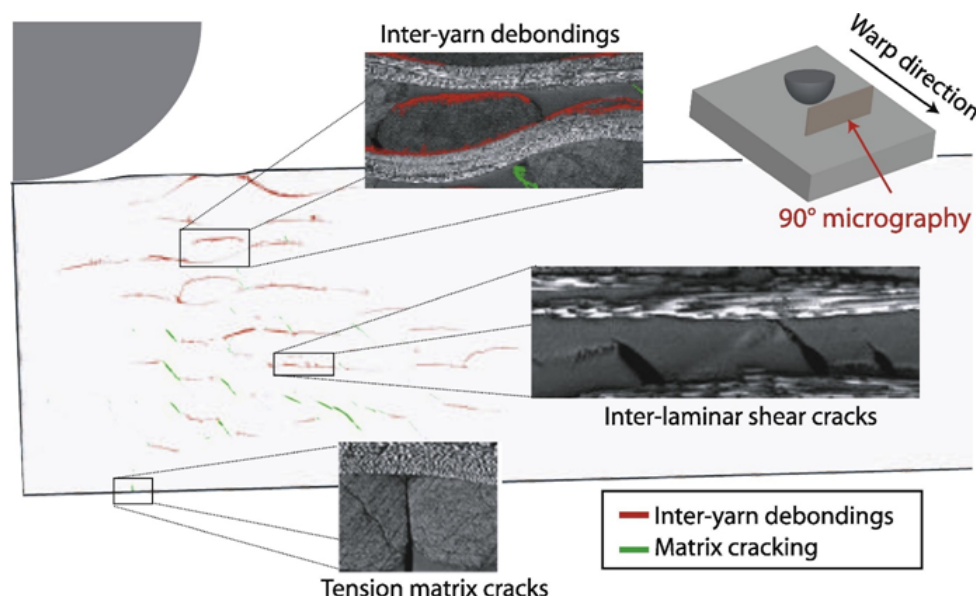


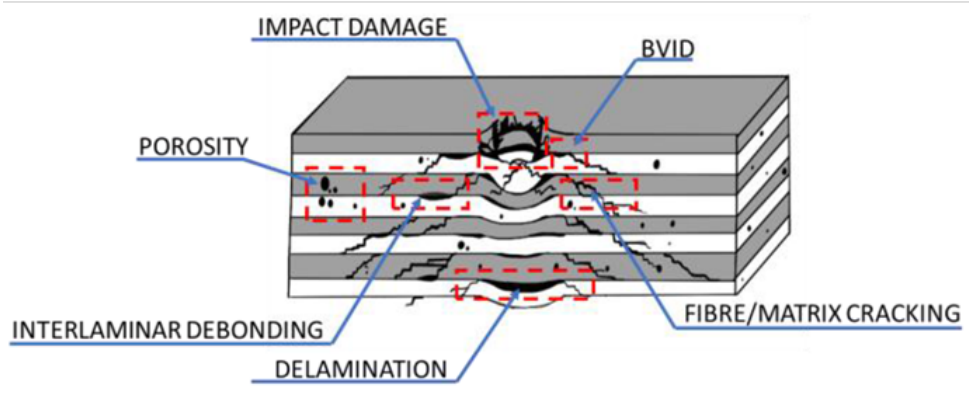
Figure 2.10 (a) a steel sample with the scanned area and (b) image at 70 GHz (arrows indicate pitting) [68].

2.2.2 Inspection of Impact Damage on Woven Carbon Fibre Composites

Recently, emerging materials such as CFRP and GFRP composites have been made more attractive and widely used in various engineering structures such as aerospace, automobile and civil engineering. It is mostly due to their high specific mechanical properties and chemical resistance. The aircraft components such as centre wing box and fuselage are now made of composite laminates. Nonetheless, these new materials are vulnerable to impact and dropped damage even at very low energy/velocity. These types of damages will leave little evidence on the impacted surface as known as barely visible impact damage. However, such damage actively induces residual strength within the material in much larger areas [118], [119].



(a)



(b)

Figure 2.11 (a) Microscopic observations of the different damage mechanisms within a 100 J impacted 3D woven plate [120] (b) Illustration of typical CFRP defects from impact damage [36].

Figure 2.11 presents the microscopic illustration of typical defects generated by impact damages. The impact damage generates major three types of defects [121], [122]: delamination/debonding, matrix cracking and fibre breakage (in case of high energy impact). Among these defects, delamination plays significant roles in reducing the residual strength of the composites, in particular, under compressive loading. The local delamination may propagate along the lateral edges. Therefore, the residual strength of the composite is usually predicted by the area of delamination. To mitigate the issues of delamination, woven composites have been developed for structures with potential exposure to impact. The presence of interleaving weft and warp yarns links the layers together and prevent the expansion of delamination cracks. As consequence, such complexity of woven structures makes it very difficult to be modelled and studied.

Near-field microwave method using microwave open-ended waveguide is known as one of the promising methods for laminated composite inspection [13], [95], [123], [124]. However, to develop an inspection technique for such complex structures of woven CFRPs, the knowledge and understanding of electromagnetic responses versus composite structural parameters is necessarily required. The study of electromagnetic responses linking to the material structure has been introduced in studies of frequency selective surface (FSS) [125]–[128]. These can be categorised into two major types: single-band and multi-band structures. For the single-band structure, the pass-band or stop-band performance is usually obtained from a planar conductive structure printed on a substrate. Multi-band structures, on the other hand, manage more than one frequency range to be passed or rejected and commonly utilise cascade structure of the single-band FSS. To analyse the performance of these FSS structures, the most intuitive way is using an equivalent circuit model, which relates to dimensions of the FSS structure (i.e., the unit dimensions and the gap between each unit). A simple single-band FSS such as conductive grid has been modelled as an LC resonator [129], where inductance L is equivalent to the width of the conductor, and capacitance C is equivalent to the gap between the conductor grid. In multi-band FSS, the equivalent circuits are usually modelled as cascading resonators or RLC lumped elements [126], [130], [131].

Compared the woven CFRP to the laminated FSS, the structure of woven CFRP is more complicated due to its wavy form of weft and warp fibre bundles. To date, there is no formulations that accurately analyse woven structures using simplified equivalent circuit models. Due to their complexity, most of the woven composite structural studies rely on computational models and numerical simulations. Mirotznik et al. [132] proposed rigorous coupled wave (RCW) method to predict EM behaviour of glass fibre composite in frequencies

up to 50 GHz. The texture unit cell was divided into four regions (i.e., x-direction fibres, y-direction fibres, overlap, and resin) without consideration of weft or warp overlapping. The assumption of modelling the overlapping area as double thickness fibres may not be applicable for the conductive composite such as CFRP since the EM waves tend to propagate along with the conductive fibres rather than penetrating through layers like that of glass fibre composite. Wang et al. [133] analysed the EM performance of composite materials using periodic finite different time domain (FDTD) method on the microscopic scale. It is found that composite materials have frequency selective behaviours that vary with fibre radius and distance between fibre bundles, however, this CFRP model is made of non-woven laminated fibres. Base on the literature review to date, there is still no comprehensive microwave study focussing on visualisation and quantitative evaluation of BVID damage on woven CFRP composites.

2.2.3 Inspection of Inner Defects in Glass Fibre Reinforced Pipe

Glass fibre reinforcement plastics have become widely used for many applications due to their inherent corrosion resistance. The use of GFRP pipes is increasingly considered as they inherit the desirable properties of glass fibre composites [134]. The key appealing of GFRP pipes is the characteristic of high corrosion resistance resulting in the lift-time smooth internal surface. Moreover, GFRP pipes offer high strength to weight ratio and relatively low elastic modulus making them more durable and resistant to vibrations and internal shocks [135]. Although GFRP pipes have been intensively used in many different services, methods to assure reliability and structural health monitoring are still not well established, particularly for installed pipes with limited access time and area. In most cases of buried GFRP pipes, visual inspection is not applicable to detect internal defects, especially for opaque thermal coated composites.

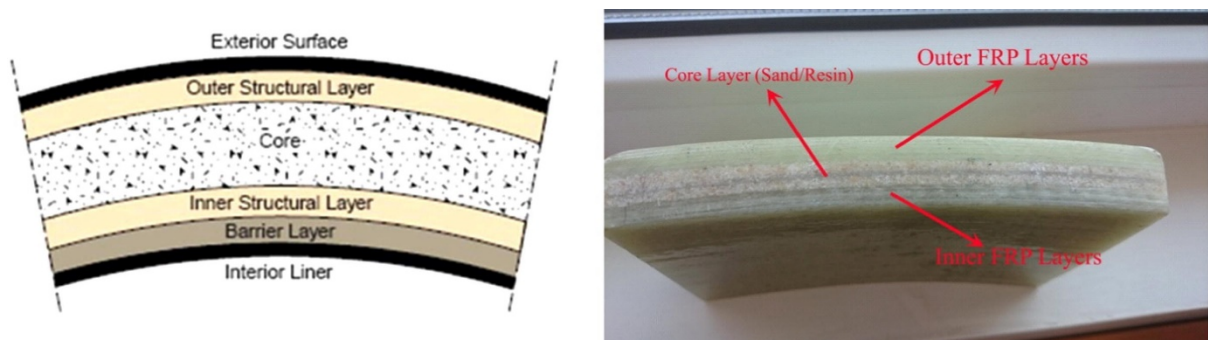


Figure 2.12 GFRP pipe wall: schematic presentation (left), cut section (right) [134].

Presented in Figure 2.12. The common GFRP pipe walls consist of three layers groups of inner layers, core structural layers and outer layers. The inner layers or liner is thin layers of surface

mat and resin providing smooth conveying of internal fluid and preventing direct contact to the internal core structure, whereas the outer layers are usually composed of pure resin. For the structural core layers placed in between, these layers are thick load-bearing layers reinforced with layers of random chopped fibre polyester to improve strength in both longitudinal and circumferential directions. The failures of GFRP pipes are in the form of short and long-term considerations [136]. The failures occurred during the manufacturing or after GFRP pipe installation include air bubbles, moisture formation, and heat released from exothermic reaction resulting in cracks on the pipe surface. The presence of bubbles or void content results in weak interfacial strength, fibre mutual abrasion, and initiation and growth of crack [137].

For low loss polymer composites such as GFRP, high frequency RF methods (i.e., microwave, millimetre-wave and Terahertz) are known to be suitable for inspection of these materials. The primary advantages of these techniques are non-contact, low attenuation in dielectric layers (including the GFRP layer and its thermal coating), and one side access. Gray et al. [138] used microwave method (range of 8.2 -18 GHz) to estimate porosity (i.e., micro balloon volume content) levels in glass fibre composites based on the measured dielectric properties. The results of porosity levels demonstrated a good agreement between the measurement and the sample physical/mechanical properties. Qaddoumi et al. [139] studied the dielectric properties of cured resin binder (used in GFRP manufacturing) in microwave frequency (range of 4-18 GHz). The results indicate the excellent correlation between the dielectric properties and state of cure of resin binder. In work of Hosoi et al. [140], delamination defects were detected in GFRP composites using microwave reflectometry. A defect with a thickness of 7.5 μm was successfully detected in a flat GFRP laminate with 3 mm thick. Ryu et al. [70] successfully utilised terahertz time-domain spectroscopy (THz-TDS) imaging system in reflection mode with 25 incident angles to detect and reveal hidden multi-delamination in GFRP laminates. Han and Kang [141] utilised a fibre-coupled THz-TDS system for characterisation and visualisation of multi-delamination by means of time-domain visualization and THz frequency-domain visualization algorithms. The thickness of the GFRP sample and multi-delamination is estimated using the reflection geometry method.

So far, microwave and THz methods have been proved for the capability of detecting internal defects (e.g., delamination) in flat GFRP composites but only a few works studied into coated GFRP pipes where their coating layer and surface curvature are the significant challenges of these techniques. Ghasr et al. [95] investigated using microwave multilayer characterisation technique by means of Euclidean distance between any two complex reflection coefficients to estimate the GFRP pipe liner and wall thickness. Full-wave simulation results showed that pipe

curvature introduces significant errors in thickness estimation. Moreover, the rough surfaces of real structures introduced a new source of error in the form of an air gap (lift-off) between the probe and wall surface.

2.2.4 Quantitative Non-destructive Evaluation

The major challenge in analysing the NDT results is finding a relationship between the measured data and the defects [142]. Various data analysis methods have been applied including regression, cluster, numerical, multidimensional, multivariate, stochastic, time series, nonlinear estimation, etc. [143]. These data analysis methods, however, have limitations. For instance, a statistical method finds a correlation between data variables but hardly justify the connection with logical descriptions and the physical rules. Therefore, the intuitive learning approaches such as machine learning methods have become in focus by many researchers. The goal of this approach is to learn an ‘offline model’ by observing a set of appearances. Based on this model, the characteristic of ‘online sample’ can be predicted. The scheme of generic machine learning is presented in Figure 2.13. The off-line process in the highlighted box correspond to the training of feature extraction and quantitative evaluation frameworks, whilst the other processes manage online quantitative evaluation in real-time. Nonetheless, it is often found that the re-training process is required periodically in order to keep the offline classifier capable of the new incoming data.

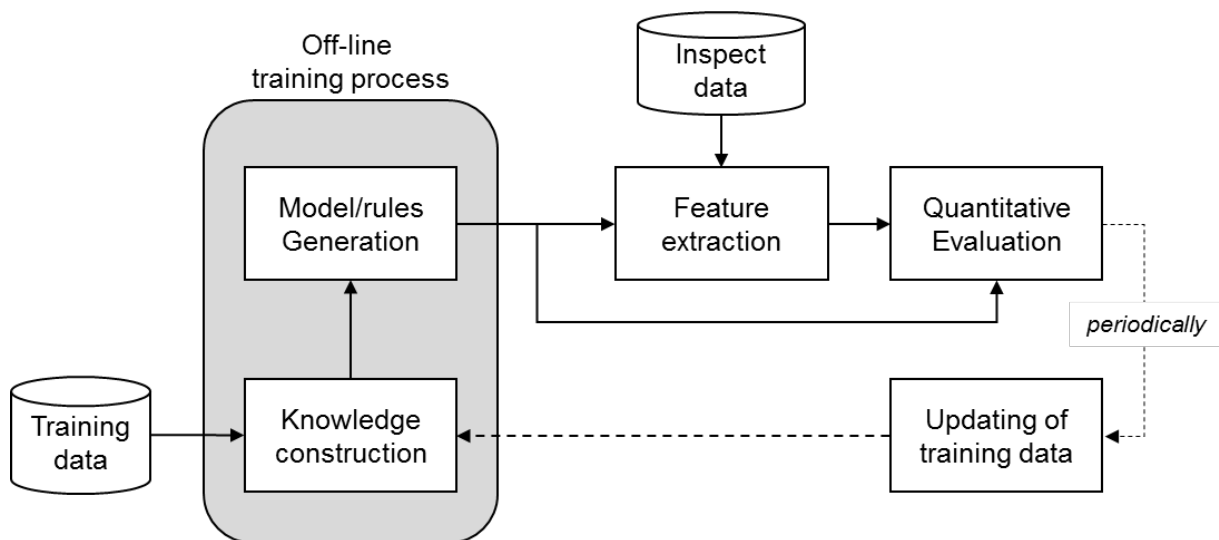


Figure 2.13 Machine learning system architecture for defect quantitative evaluation.

2.2.4.1 Pre-processing

The pre-processing algorithms are applied to sensor data to enhance the signal-to-noise ratio (SNR) and contrast interesting features from the data. These algorithms are essential, particularly, in the microwave inspection at far-field condition (GPR like scenario) where the

measurements probe is in the distance to the inspecting target and surrounding by unavoidable RF interferences and clutter in the measurement scenario. The common pre-processing algorithms are noise filtering and clutter reduction. Most common techniques use Gaussian clutter assumptions due to its simplicity [144] which may degrade the optimal performance. Gurbuz [145] proposed a low-complexity goodness-of-fit test suitable for online GPR detection determining the clutter distribution. The results demonstrate that the distribution of GPR clutter is a gamma distributed rather than Gaussian. Nuzzo [146] applies Radon transform to remove coherent noise in GPR signals. The results achieved are quite encouraging compared conventional methods. Baili et al. [147], [148] applied discrete wavelet transform (DWT) for noise reduction of the GPR signals obtained from flexible pavements. The results demonstrated the improved performance in terms of signal-to-noise ratio (SNR).

2.2.4.2 Region of Interest Extraction

The region of interest (ROI) extraction is an important method required for complex measurement scenarios such as detecting targets in multilayered structures, in particular. It improves the overall computational efficacy of detection and characterisation. In applications of civil engineering such as road pavement assessment [149]–[151] and railway-ballast evaluation [91], [92], [152], the layer boundaries are usually obtained from reflected signals at discontinuous in layer properties (i.e., contrast in permittivity and/or conductivity). To determine layer thickness, time delay estimation (TDE) [151], [153] and time-of-flight (ToF) [154] have been proposed for estimating the layer thickness from the signal echoes, whereas amplitude estimation is used to retrieve the wave speed related to relative permittivity in each layer. The threshold detector and matched filter (MF) detector are utilised in [155], the results show the MF method is superior in case of low SNR, but the threshold detector performs better in case of thin layers, however, both methods are not able to solve successive (overlapped) echoes for a $B\Delta\tau \leq 1$, where B is operating bandwidth, $\Delta\tau$ is the minimal time shift between echoes that can be distinguished. Further enhancement of time resolution was introduced in the studies of multiple signal classification (MUSIC) [153] and estimation of signal parameters via rotational invariance techniques (ESPRIT) [156]–[158] as model-based methods. Machine learning algorithms have been introduced more recently and the support vector machine (SVM) based method known as support vector regression (SVR) [151]. It can compensate the model uncertainty by a large experimental training data set. Other than that, there are velocity estimation methods based on measurement configuration, such as common midpoint (CMP) method [150], [159], [160] and full waveform inversion (FWI) method [161], focusing on determination of layers properties.

2.2.4.3 Feature Extraction

Feature extraction transforms raw data into informative signatures of a system. The process that extracts properties of data such as sample value at the particular time, sample dimensions, physics nature, and signal dynamics could be considered as feature extraction methods. Due to the nature of microwave wideband signals in multilayered structures, the responses are usually in terms of multiple resonances and ripples caused by complex multiple reflections and interrogation of electromagnetic waves within the interfacing dielectric layers. In the practical microwave NDT applications, the obtained responses are high dimensional data with highly dynamic characteristic. Therefore, in this work, the feature extraction methods based on machine learning with statistical analysis such as principal component analysis (PCA) and independent component analysis (ICA) are focused.

In early development, the linear transformation method such as PCA, ICA, and Linear Discriminant Analysis (LDA) are applied to extract significant features from the signals. In PCA, the measurement signals are modelled in the form of linear combination of multiple signal sources (both target and clutters) upon which the signals from target are stronger. Thus, the most significant components (the first principal component) represents the target [162]–[164], whereas the rest signals are regarded as clutters or noises. Sophian et al. [165], [166] proposed a new approach for eddy current NDT application using PCA. The results show the improvement of surface and sub-surface defect detection and classification over the conventional method. PCA has been successfully applied to analyse microwave responses for defect characterisation. Miszczyk et al. [167] applied PCA to inspect protective linings based on a dataset of microwave magnitude spectra. The results showed that various type of defects including wet/dry corrosions and void were successfully characterised by the first two PCs.

The major limitation of conventional PCA is the capability to only extract the linear features from the data, therefore, various nonlinear version of PCAs have been introduced. Kramer [168] presented a nonlinear PCA using auto-associative neural networks. Tan and Mavrovouniotis [169] proposed a nonlinear PCA based on a three-layer network with input training. Hiden et al. [170] proposed a symbolically oriented technique based on the genetic programming (GP) paradigm. Alternatively, Kernel PCA is a novel and high computational efficiency method performing a nonlinear form of PCA in high-dimensional feature using nonlinear mapping, is proposed by Schölkopf et al. [171]. The use of simple matrix algebra making more appealing as optimisation methods [172]. Kernel PCA transforms original data to high dimensional feature space and extracts a significantly larger number of nonlinear principal components allowing better extract of features and discard of noisy space (see Figure 2.14).

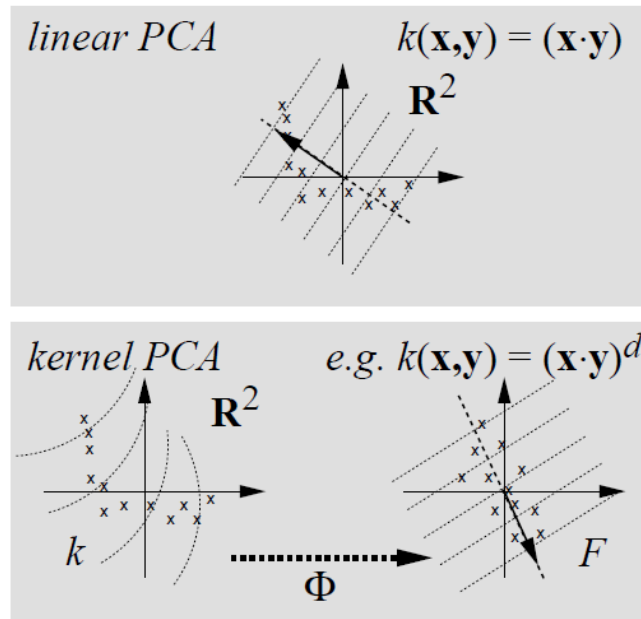


Figure 2.14 The concept of linear PCA and Kernel PCA [171].

It is known that the competency of using conventional PCA is adequate if the data are Gaussian distributed, linear, and stationary. However, in some instance, scattering signals from clutters can be stronger, and thus dominate the target signals. In this case of the scattering signal from clutters are as strong as that of the target, ICA has been applied and proved to be more efficient in highly cluttered environments [173]. The LDA is a supervised method taking the difference between classes into account. It searches the projecting direction by minimizing the within class distance and maximizing the between class distance, so the feature extracted by the LDA extract is most classified [174].

Since A-scan data can be considered as waveform signals, the studies of using time-series transformation methods such as DWT [147], [175], [176] have been applied for feature extraction. DWT is an alternative method to the conventional Fourier transform. Unlike the Fourier method, Wavelet is suitable for analysing non-stationary signals and provides an optimal time-frequency resolution in all frequency ranges. For example, the work of [125] applies DWT and calculation of wavelet entropy; the results demonstrate that both techniques are useful tools for extracting information from the radar signal.

In time-frequency analysis, the vector spectrum of time signals can also be presented as an image of a time-frequency plot. Methods of time-frequency analysis include STFT [178], Wigner distribution (WD) [179], Hilbert-Huang transform (HHT) [180] and wavelet methods [181]. For the image features (based on B- or C-scan data), statistical pattern recognition approaches have been developed. These include algorithms based on hidden Markov model (HMM) [182], [183], edge histogram descriptors (EHD) [184], [185], spectral features [186],

geometric features such as Hough transform (HT) [187], [188] and the average energy value from C-scan [189].

2.2.5 Synthetic Aperture Imaging

The microwave and millimetre-wave NDT&E imaging techniques use the relative position between the probe/antenna and the sample to reveal the spatial distribution of the interesting targets. In this technique, an equivalent large aperture is calculated from a set of smaller probe apertures, so the term synthetic aperture radar or SAR was defined [190]. Originally, the image-reconstruction algorithm was developed for acoustic holography referred as the backward-wave reconstruction [191]. However, the image resolution is limited for near-field systems. Later, Soumekh [192], [193] introduced a model of wavenumber and angular frequency in lieu of frequency and spatial frequency parameters, with extensively used of Fourier transforms. This system is quasi-monostatic, where transmit and receive point is assumed to be at the midpoint of the two antennae.

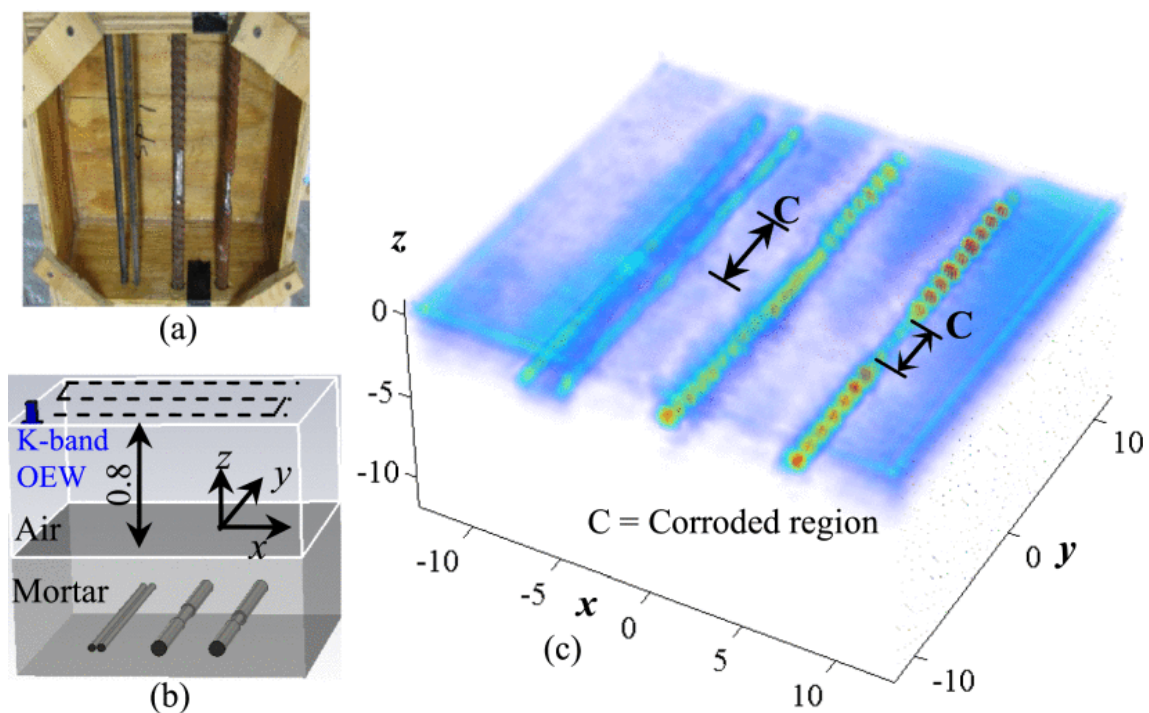


Figure 2.15 (a) sample before pouring mortar, (b) measurement setup, and (c) reconstructed high-resolution 3-D (volumetric) image from experimentally collected data at K-band (units: cm) [194].

Wideband SAR techniques have been utilised to evaluate internal structures by rendering high range and cross-range resolution images. The SAR processing has demonstrated great potential in a wide range of NDT applications, including imaging of stratified dielectric [73], [194]–[196], concealed weapon [197] and composite structures [198]. For example, Fallahpour et al. [73], [194] utilised SAR algorithms with data obtained from a monostatic probe over a mortar

sample. The proposed SAR uses $\omega-k$ algorithm and the targeted application was to detect rebar embedded in the layered mortar sample. The 3-D reconstruction was successfully obtained from multiple reflections and signal attenuation of the scattered electromagnetic signals as a result of the inhomogeneity (dielectric contrast) of the layer (see Figure 2.15).

2.3 Identification of Challenges in Microwave NDT&E for Multilayered Structures

Microwave NDT&E using open-ended waveguide probes have proven to be an ideal method for inspecting multilayer dielectric structures including layer properties characterisation, delamination, and visualisation of layered structures. However, the electromagnetic waves interrogation between antenna/probe and sample are complex and thus require effective system configuration and quantitative non-destructive evaluation (QNDE) method. This project proposes a development of microwave NDT&E system to overcome the limitations of defect and layer properties evaluation in multilayered structures. Based on the literature review in previous sub-sections, problems and challenges are identified as follows.

1. System configuration of microwave NDT&E using open-ended waveguide for inspecting multilayered dielectric and composite structures including steel corrosion under coating (homogenous layered dielectric backed by conductive plate), woven CFRP laminates with impact damages (composite with conductive/dielectric weaving texture) and thermal coated GFRP pipes with inner flat-bottom holes (curved and layered dielectric composites).
2. Feature extraction for defect and layer properties that reduces the redundancy in data (dimension reduction), enhances the informative data, facilitates visualisation and quantitative evaluations, and eliminates uncorrelated interferences (e.g., coating, insulation layers, noise and clutters). The feature extraction methods based on machine learning with statistical analysis such as PCA and ICA could be applied to reduce redundancy and extract interesting eigenfeature from high dimensional data of microwave wideband responses.
3. Visualisation of high quality images/volumes (i.e., good contrast/sharpness, high resolution, and low noise) of defects and layer properties in meaningful presentation, leading to better human interpretation and quantitative analysis. The 2-D SAR technique combine multiple measurement positions to form a synthetic aperture, which improves the cross-range resolution of the reconstructed images.
4. Quantitative evaluation of defects and layer properties within the multilayered structures, giving the meaningful and sensible relationship between feature values and the interesting properties of the material. The 3-D SAR tomography can be

reconstructed from microwave wide band responses of scanning area. The reflection obtained from time-domain signals allowing an estimation of buried target depth based on time-of-flight feature.

2.4 Chapter Summary

In this chapter, literature reviews of microwave and other NDT&E approaches for multilayered structures are presented. Based on advantages and disadvantages of each method, microwave NDT&E has been proved to be a suitable method for inspection of multilayered dielectric structures. Finally, the challenges and problems of microwave NDT&E for multilayered structures are identified. The critical challenges of microwave NDT&E are the requirements of a configuration of microwave NDT&E system for multilayered structures, feature extraction methods that enhance informative parameters while eliminating uncorrelated influences, visualisation methods producing high-quality images, and quantitative evaluation methods based on selected features that link to the interesting defect and layer properties.

In the following chapter, the theoretical background of microwave open-ended waveguide along with design and hardware implementation of microwave NDT&E system are presented. Also, experimental studies with multilayered samples used in this work together with data analysis and quantitative evaluation are described.

Chapter 3 Development of Microwave NDT&E System

Following on the challenges discovered in Chapter 2, this chapter presents the methodology and theoretical background of microwave NDT&E for multilayered structures, in conjunction with three case study models of and its applicability to reveal hidden layer properties. The research methodology is outlined in the remainder of the chapter. The theoretical background of the microwave NDT&E using open-ended waveguide is explained in terms of electromagnetic wave interrogation between aperture and sample surface with a physical mechanism.

The behaviour of the microwave NDT&E system in near field with propagation mode TE_{10} are discussed in Section 3.1 . The geometric consideration topologies of three case study models are described in Section 3.2. Section 3.3 looks into the development and implementation of microwave NDT&E system along with data acquisition mechanisms. The final section summarises the content of this chapter.

3.1 Background of Microwave NDT&E using Open-ended Waveguide Probe

The electromagnetic propagation in multilayered media has been extensively studied in the past decades. When the target is far enough (far field), the reflected waves can be considered as a uniform plane wave propagating in traverse electromagnetic (TEM) mode. The behaviour of these reflected waves could be easily studied by a transmission line model, as shown in Figure 3.1. The transmission coefficient (T_i) reflection coefficients (R_i) at each layer interface i are defined as the complex ratio between transmitted and reflected waves, respectively. These complex coefficients are then calculated by applying boundary conditions as tangential components of electric (E-field) and magnetic fields (H-field).

Even though the assumption of TEM wave could be applied for many far-field applications, many NDT works require operation at relatively close to small defects (e.g., crack and corrosion) to maximise sensitivity and avoid surrounding interferences, and thus the plane wave assumption does not satisfy the requirement and no longer valid. Therefore, EM formulation of the fields within the layered structure has been investigated through analysis of Green's functions [199]–[202]. However, this work does not intend to analyse complex electromagnetic interrogation of the forward model full-wave equations with the generic multilayered model. Only near field operation of open-ended waveguide probe with dedicated sample models (i.e., dielectric material) and the fundamental operating frequency ranges are considered, and thus the reflected waves are being described as transverse electric (TE) propagation mode.

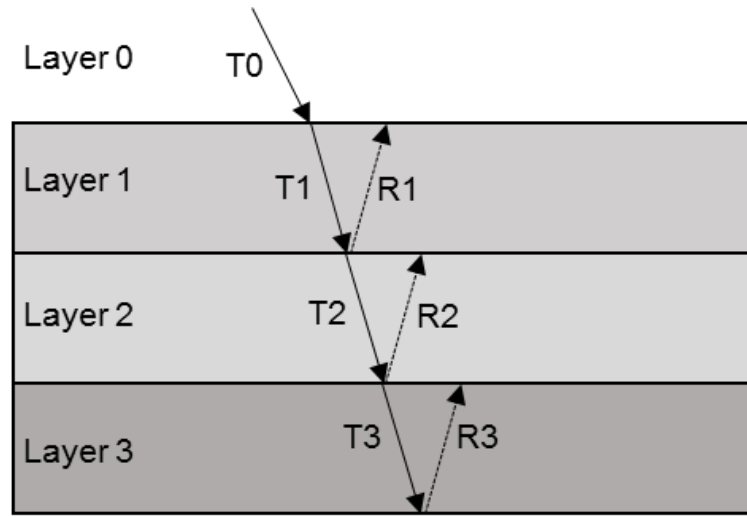


Figure 3.1 Plane wave transmission and reflection in multilayered media based on transmission line model

Based on the selected near-field probe (i.e., open-ended rectangular waveguide) and the symmetry of the incident field and the measurement geometry, only rectangular waveguide modes with $m = \text{odd}$ (1, 3, 5, ...) and $n = \text{even}$ (0, 2, 4, ...) can be excited at the probe aperture [58]. Calculations of cut-off frequencies at different modes of a waveguide probe are given by [58]

$$f_{c_{mn}} = \frac{1}{2\pi\sqrt{\mu\varepsilon}} \sqrt{\left(\frac{m\pi}{a}\right)^2 + \left(\frac{n\pi}{b}\right)^2}, \quad a > b \quad (3.1)$$

where μ and ε are permeability and permittivity of waveguide filling material, respectively, a and b are inner length and width of the waveguide aperture, respectively, m and n are integers used to determine the waveguide propagation modes, respectively.

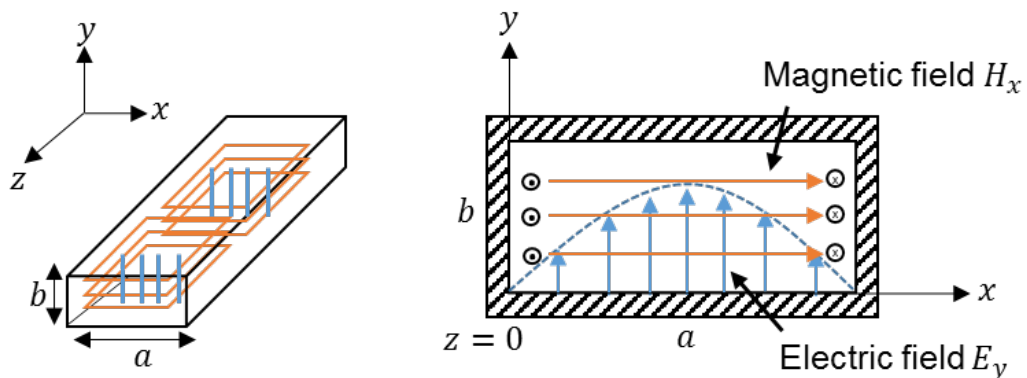


Figure 3.2 E-field and H-field distribution of rectangular open-ended waveguide operating in TE_{10} mode

The open-ended waveguide probes are configured to operate only in the dominant TE_{10} mode by confining the operating frequency within the propagation mode ($m=1, n=0$). Although it is

known that the higher order modes are produced by the interrogation between waveguide aperture and samples, this effect is considered insignificant since it affects measurement result for only less than 3% [63]. The reflection coefficient relating to the coupling between the termination admittance of probe Y_{WG} (or impedance Z_{WG}) and the testing sample. The terminating admittance of the waveguide Y_{WG} can be written as [63]

$$Y_{WG} = G + jB = \frac{\iint_{aperture} [\bar{E}(x, y, 0) \times \bar{W}(x, y, 0)] \cdot \hat{a}_z dx dy}{\left[\iint_{aperture} \bar{E}(x, y, 0) \cdot \bar{e}_o(x, y) dx dy \right]^2} \quad (3.2)$$

$$\bar{W}(x, y) = \bar{H}(x, y, 0) + \sum_{n=0}^{\infty} Y_n \bar{h}_n(x, y) \iint_{aperture} \bar{E}(\eta, \xi, 0) \cdot \bar{e}_n(\eta, \xi) d\eta d\xi \quad (3.3)$$

where $\bar{E}(x, y, 0)$ and $\bar{H}(x, y, 0)$ are the apertures of electric and magnetic field distributions, respectively. The waveguide terminating admittance is expressed using transverse vector mode function and their orthogonal properties. The n th vector mode functions are e_n and h_n , Y_n is the characteristic admittance of the waveguide for the n th mode. Hence, the TE_{10} aperture field presented in Figure 3.2 is given by [63]

$$E_y(x, y, 0) = \bar{e}_o(x, y) = \begin{cases} \sqrt{\frac{2}{ab}} \cos\left(\frac{\pi x}{a}\right), & (x, y) \in aperture \\ 0, & (x, y) \notin aperture \end{cases} \quad (3.4)$$

3.2 Multilayered Models for Microwave NDT&E Experimental Studies

Based on the challenges of microwave NDT for multilayered structures identified in section 2.2.5, three types of dedicated multilayered samples are investigated as follows.

3.2.1 Corrosion Progression Sample

Corrosion progression models are chosen to investigate the microwave responses of corrosion at different progression stages (exposure periods). Based on the literature review of previous works, many microwave NDT techniques [203], [76], [95], [96] could reveal a hidden dielectric layer property (i.e., thickness and permittivity). However, estimation of corrosion layer property is still a challenge because its thickness and chemical compound are varying over time [105]–[107]. The thickness of the corrosion layer tends to rapidly increase in the early stages, while the increasing rate drops in the long-term and may become negative due to flaking off and metal loss. Moreover, steel plates are usually coated with primer and paint to prevent them

from corroding, but corrosion can still develop under the coating due to delamination and peeling of the coating layer overtime.

So far, there is no comprehensive study of microwave open-ended waveguide responses related to corrosion progression and complex changes in the corrosion layer properties. To study the influence of coating layer along with corrosion progress, two types of corrosion progression models (i.e., coated and uncoated) shown in Figure 3.3, are designed and investigated in this work. The layers of coating and steel corrosion are simulated by layers homogenous dielectric with different properties and thickness. In these models, the property of the corrosion layer is varying along with the corrosion progression period, whereas the layer property of the coating remains constant for all exposure periods. To mitigate the lift-off effect, the open-ended waveguide probe obtains reflection coefficient response over the sample surface with no lift-off.

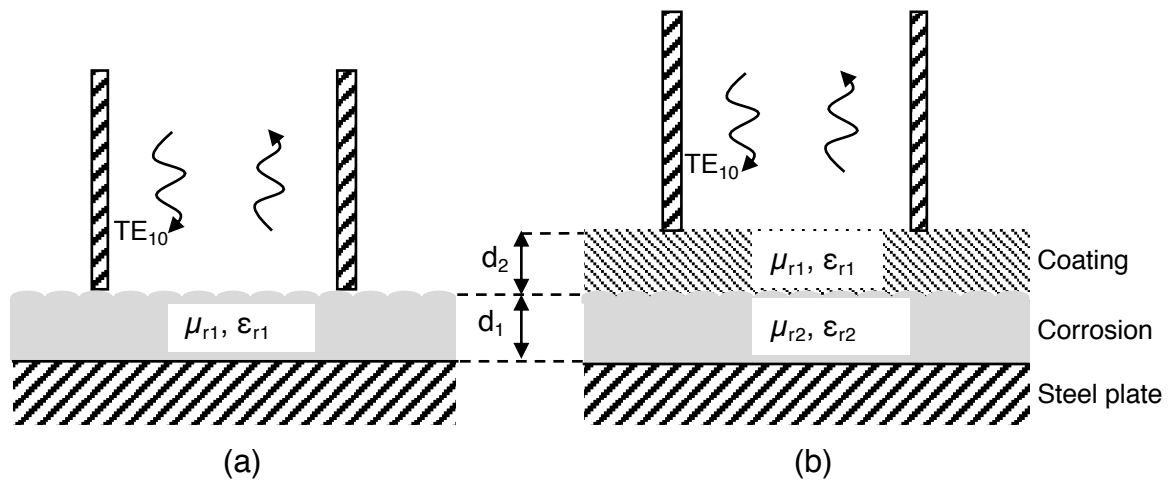


Figure 3.3 Models of corrosion progress (a) with coating and (b) without coating

3.2.2 Woven CFRP with Impact damage

Models of woven carbon fibre reinforced polymer or CFRP are selected to study the influence of spatial texture to the microwave responses of impact damages at different impact energies ranging from 2 J to 10 J. The woven CFRP structure consists of the fibre bundles or fibre yarns embedded in the polymer matrix as illustrated in Figure 3.4. The yarns made of a bundle of carbon fibres are identified as traverse (weft) and longitudinal (warp) depending on the fibre directions (0 and 90 degrees). The electrical conductivity of CFRP is anisotropic as the estimated conductivities are between 10 S/m – 100 S/m in the transverse direction and 5,000 S/m and 50,000 S/m in the longitudinal direction.

Impact damages on CFRP are produced by a drop test apparatus with a hemispherical bumper head illustrated in Figure 3.5. The samples are categorised by the impact energy W , which can be obtained by

$$W = mgh \quad (3.5)$$

where m is the mass of hammer, g is the acceleration due to earth gravity and h is the height of the hammer. Although the type of defects occurred in the sample might be different depending on the impact energy, the common defects of low impact damage include surface dent, matrix crack, delamination and fibre breakage [204].

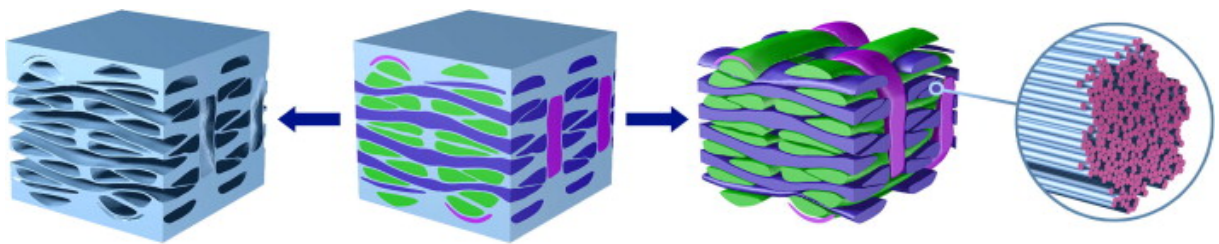


Figure 3.4 Structure of 3D woven composites composed of a matrix of polymer (blue) and carbon fibre bundles in different directions (other colours) [205].

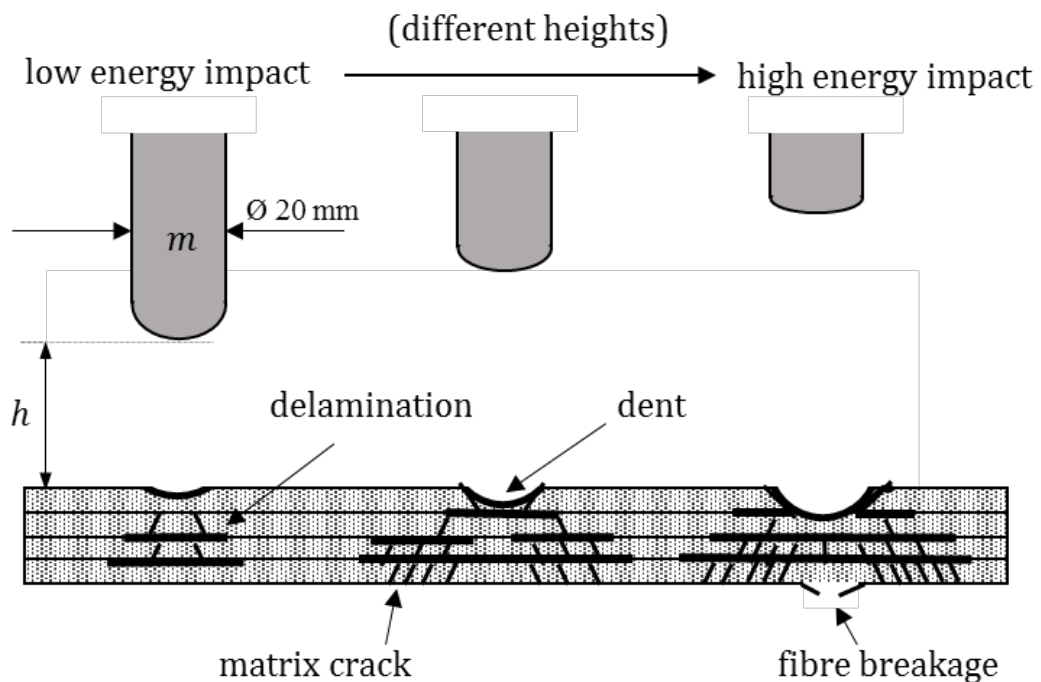


Figure 3.5 Defects of impact damage at different impact energies

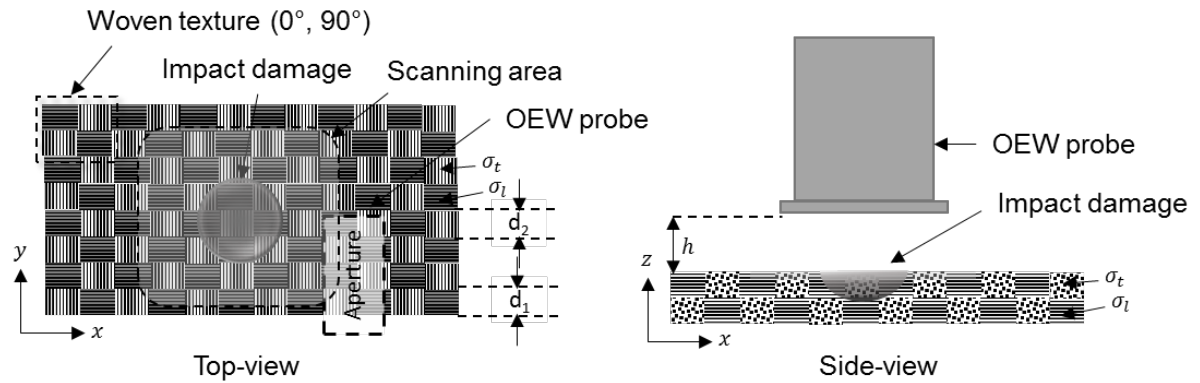


Figure 3.6 Model of woven CFRP with impact damage

The model of woven CFRP with impact damage for microwave NDT&E using open-ended waveguide is presented in Figure 3.6. In order to obtain the area of impact damage, the probe will perform C-scan over the impact damage area. Due to the high contrast in conductivity at different fibre directions (i.e., transverse and longitudinal), the spectral image obtained from the impact area of woven CFRP will reveal both texture and fibre defect. This makes it difficult to characterise and quantitative evaluation of associated defect in the impact area, unusually, at low impact energy where the defect size is comparable to the unit cell texture. Moreover, the C-scan process requires a certain lift-off to prevent from surface scratching, and thus introduces blurring effect to the image and it requires image enhancement method such as SAR to improve the sharpness (focus) of the obtained responses.

3.2.3 Glass Fibre Reinforced Polymer with Flat-bottom hole defects

Glass fibre reinforcement plastics have become widely used for many applications due to their inherent corrosion resistance. However, methods to assure reliability and structural health monitoring are still not well established, particularly for installed pipes with limited one side access and operation time. In most cases, visual inspection is not applicable to detect internal defects, especially for opaque coated composites. Although, microwave and THz methods have been proved for the capability of detecting internal defects (e.g., delamination) in flat surface GFRP composites [70], [140], [141], only a few works studied into coated GFRP pipes where their coating layer and surface curvature are still the major challenges of these techniques. Ghasr et al. [95] investigated using microwave multilayer characterisation technique by means of Euclidean distance between any two complex reflection coefficients to estimate the GFRP pipe liner and wall thickness. Full-wave simulation results showed that pipe curvature introduces significant errors in thickness estimation. Moreover, the rough surfaces of real structures introduced a new source of error in the form of an air gap (lift-off) between the probe and wall surface.

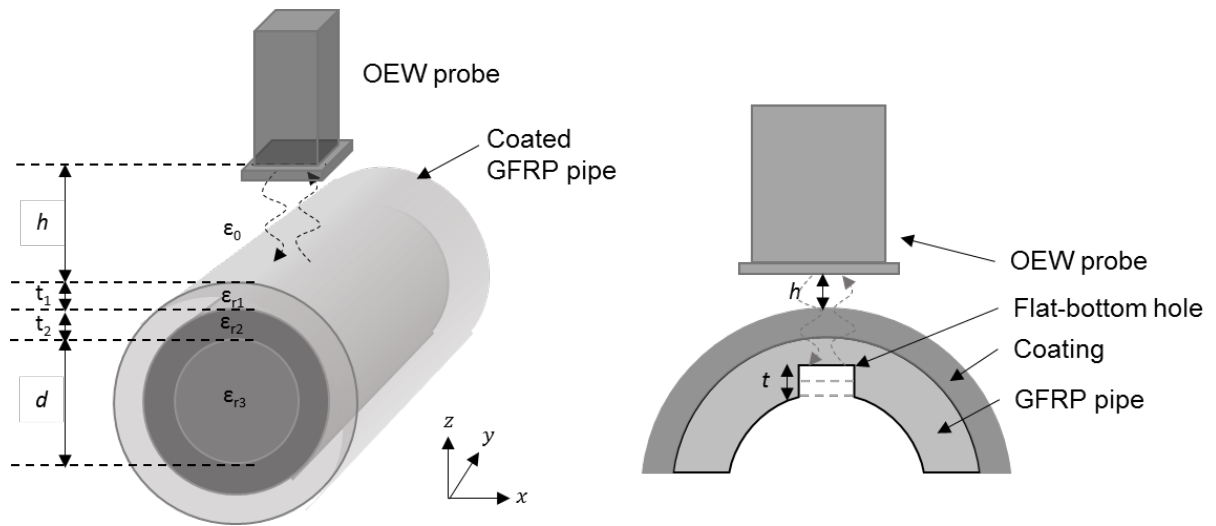


Figure 3.7 A model of GFRP pipe with FBH defect

The model of GFRP pipe with four different depths of flat-bottom-hole defects is presented in Figure 3.7. The dedicated GFRP pipe in this work is composed of 14 layers fibreglass composites with a thermal barrier coating, has a total thickness of a 13 mm. The GFRP pipe is cut to an arch portion and scanned by microwave open-ended waveguide over the defect area. The FBHs at different depths: 2.5, 5.0, 7.5 and 10 mm, are machined on the inner surface of the GFRP. It is worth mentioning that this sample has been investigated by long pulse excitation tomography with configurations described in [37], [206]. Only the shallowest defect H1 was revealed in the results due to the adverse effect of the thermal coating layer and low heat conductivity of GFRP.

3.3 Design and Implementation of Microwave NDT&E System

According to the challenges of microwave NDT and multilayered models described in Section 2.2.5 and Section 3.2, respectively, a microwave NDT&E system using an open-ended waveguide probe is designed and implemented as follows.

3.3.1 Design of Microwave NDT&E System

The system diagram of microwave NDT&E using open-ended waveguide probe is presented in Figure 3.8. It comprises hardware modules include a computer unit, an x-y scanner (step resolution of 0.1 x 0.1 mm), a signal generator and standard open-ended rectangular waveguide probe (frequency range between 8-26.5GHz). The computer unit contains a data acquisition module, a storage device and corresponding software to control the operation. In common measurement operation, the control unit sends a position to the x-y scanner to employ probe at specific x and y position over the sample. Once the probe is in position, the control unit sends a trigger signal to the signal generator to emit excitation signal (i.e., a wideband signal) and

measure the response of the sample under test (SUT) via the open-ended waveguide probe. Consequently, the reflected signal or a ratio between excitation and reflected signals are obtained and sent to a data acquisition of the computer unit. The data acquisition captures the response, then sends it to display in a visualisation software and store in the storage device. In the individual scanning position, the obtained wideband response is presented in the form of magnitude and phase plots. The format data storage is dependent to the scanning operation (i.e., A-, B- or C-scan), the sample responses are stored in form of a spectral vector or a multi-dimensional matrix of spectral response with the spatial position x and y . Once the scanning process and data storage are completed, the further off-line signal processing processes including feature extraction, quantitative analysis and visualisation are involved. The obtained data will be analysed through the feature extraction process to facilitate enhancing of interesting parameters while eliminating redundancy and reducing uncorrelated dimensionality in the measurement data. The features calculated from the feature extraction process are then send to visualisation process. Based on the type of sample and acquired measurement data, the results can be displayed in terms of images or 3-D volumetric with enhancement using imaging methods (e.g., SAR and tomography). The image results of spatial features such as impact damage and flat-bottom hole can be useful for quantitative evaluation for location and sizing, whilst simple features such as steel corrosion progress can be directly analysed based on the feature values without visualisation process.

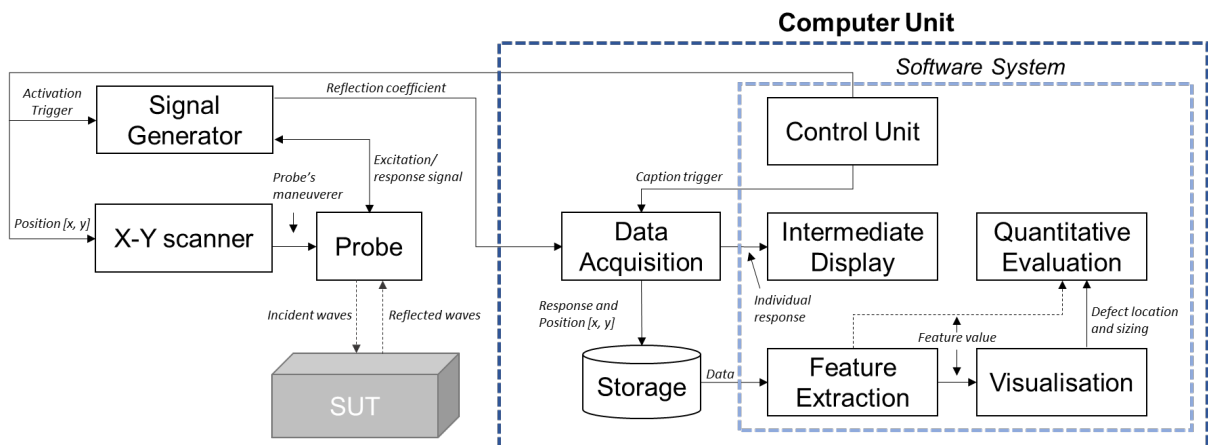


Figure 3.8 System diagram of Microwave NDT using open-ended waveguide probe

3.3.2 Implementation of Microwave NDT&E System

Based on the system designed in the previous Section, the microwave NDT&E system using open-ended waveguide probes is configured from available hardware components. Software for

control, data acquisition, signal processing, and data analysis are written in MATLAB scripts. The implementation details of these are as follows.

3.3.2.1 System Configuration

Based on the system design described in section 3.3, the equipment setup of microwave NDT&E system using open-ended waveguide probe is presented in Figure 3.9. The major hardware components are composed of a personal computer with Windows operating system and MATLAB software, an X-Y scanner High-Z S-720, a vector network analyser (VNA) Agilent PNA E8363B. The computer is connected to the scanner controller by the parallel port interface (LPT), while connected to VNA by general purpose interface bus (GPIB). The control software for the scanner and VNA is written in MATLAB script based on manufacturer provided libraries. Prior to the measurement, the VNA will be calibrated together with the measurement coaxial cable using an electronic calibration kit (with a terminal of open, short and load).

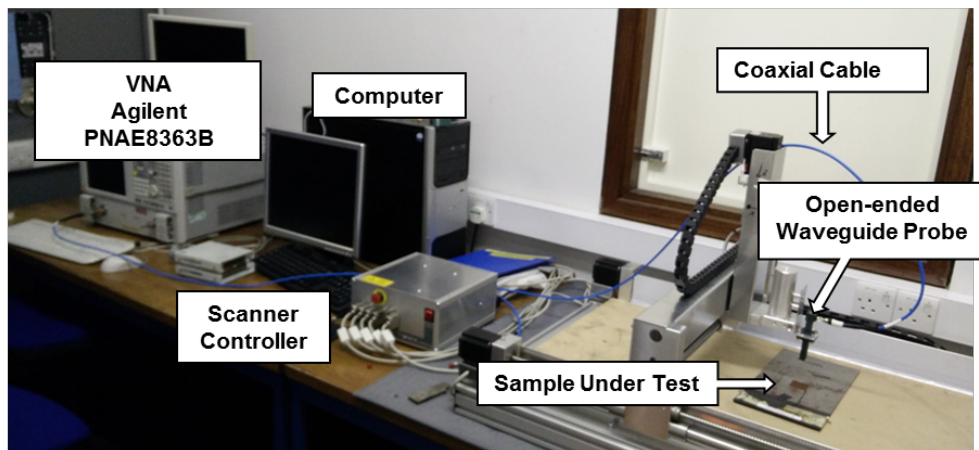
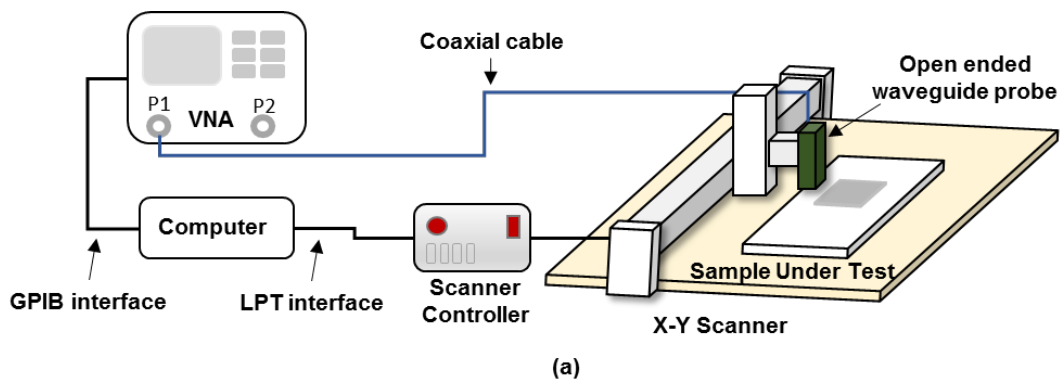


Figure 3.9 Microwave NDT using open-ended waveguide system configuration (a) system illustration and (b) actual system implementation

3.3.2.2 Measurement Mechanism

The scanning script written in MATLAB has been programmed to synchronise between the scanning operation of the X-Y scanner and the measurement of VNA as described in Figure 3.10. Once the scanning operation begins, the scanner will initiate its position at the origin ($x = 0$ and $y = 0$). Then, the control software sends a command to trigger the VNA to capture the response at the current x and y position and save it to computer memory. Following this, the program will check the current position of x and if it is not exceeding the width X then increase the x position by Δx , otherwise reset x position and increase y position by Δy . The scanning operation is repeated until the y position is equal to the length Y . Finally, the responses obtained at each iteration are saved in a storage device for further signal processing and data analysis. Figure 3.11 shows the graphical user interface (GUI) of the control unit software. Prior to the scanning operation, the user will input the scanning sizes of X and Y , step sizes by Δx and Δy , scanning speeds and saving filename on the left pane of the program window. During scanning operation, the magnitude and phase responses of the individual scanning position are displayed in the status pane of the program window.

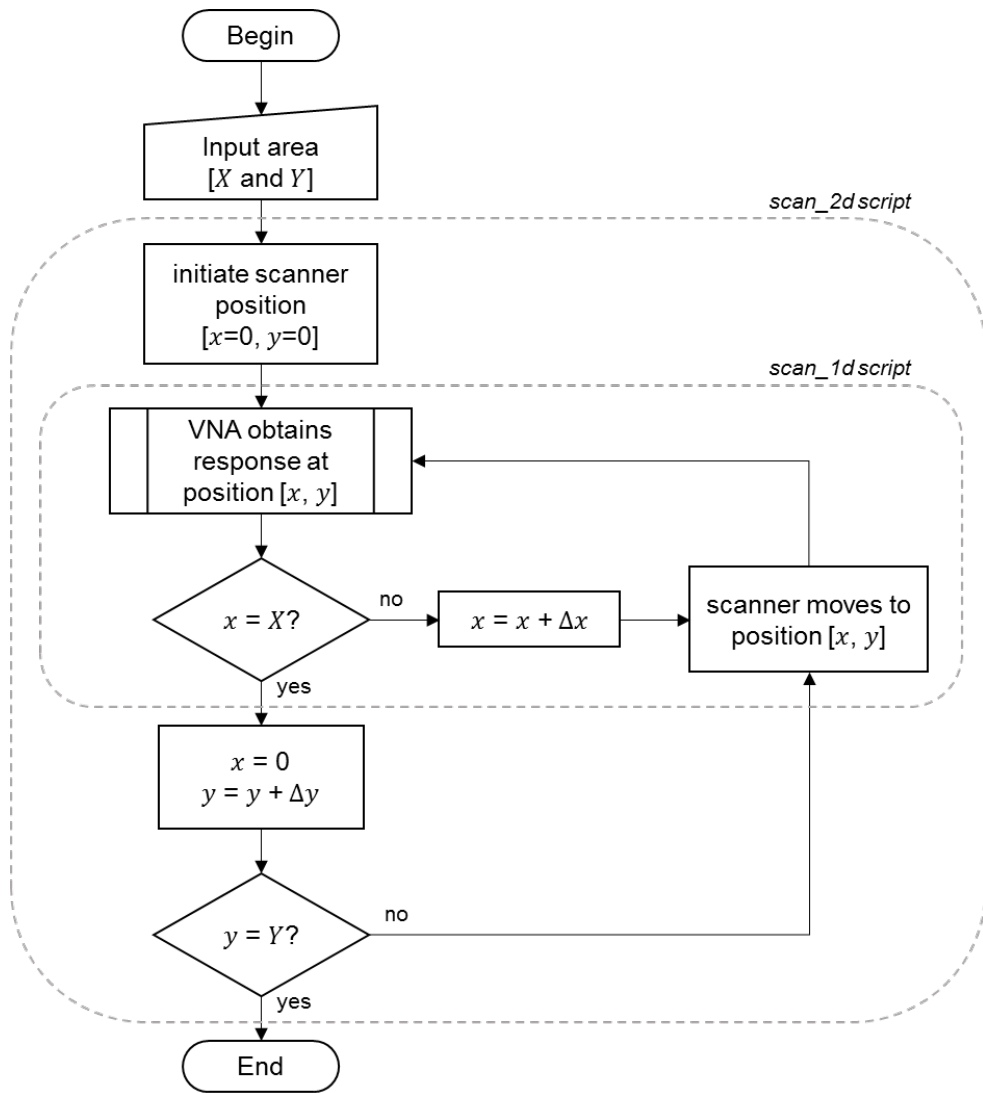


Figure 3.10 Flowchart of C-scan operation of microwave NDT&E system

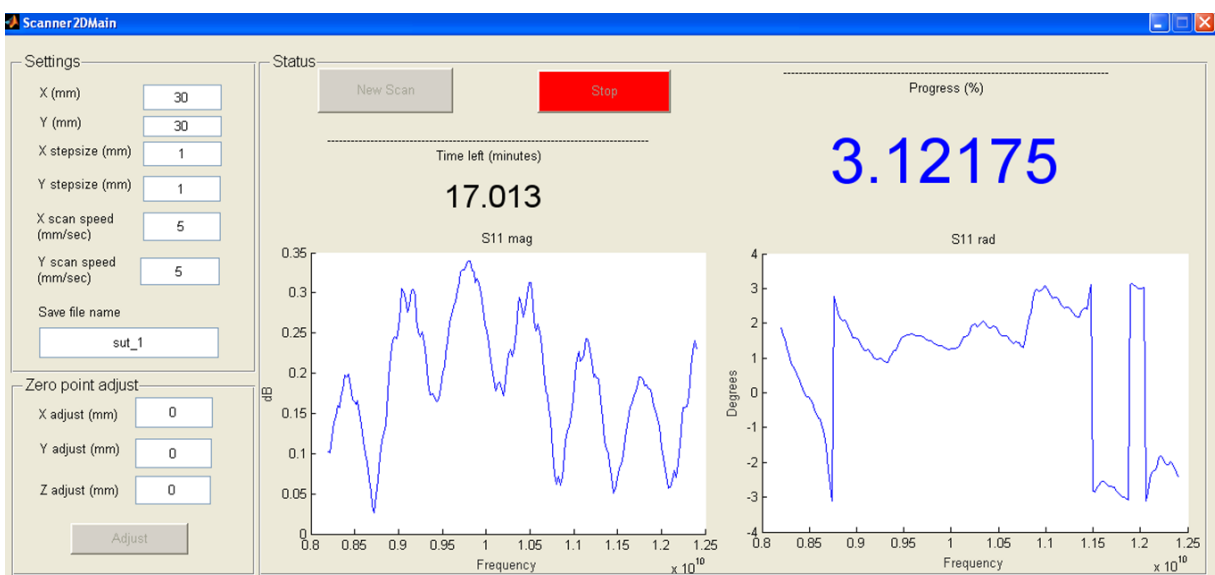


Figure 3.11 Graphical user interface (GUI) of microwave NDT&E system

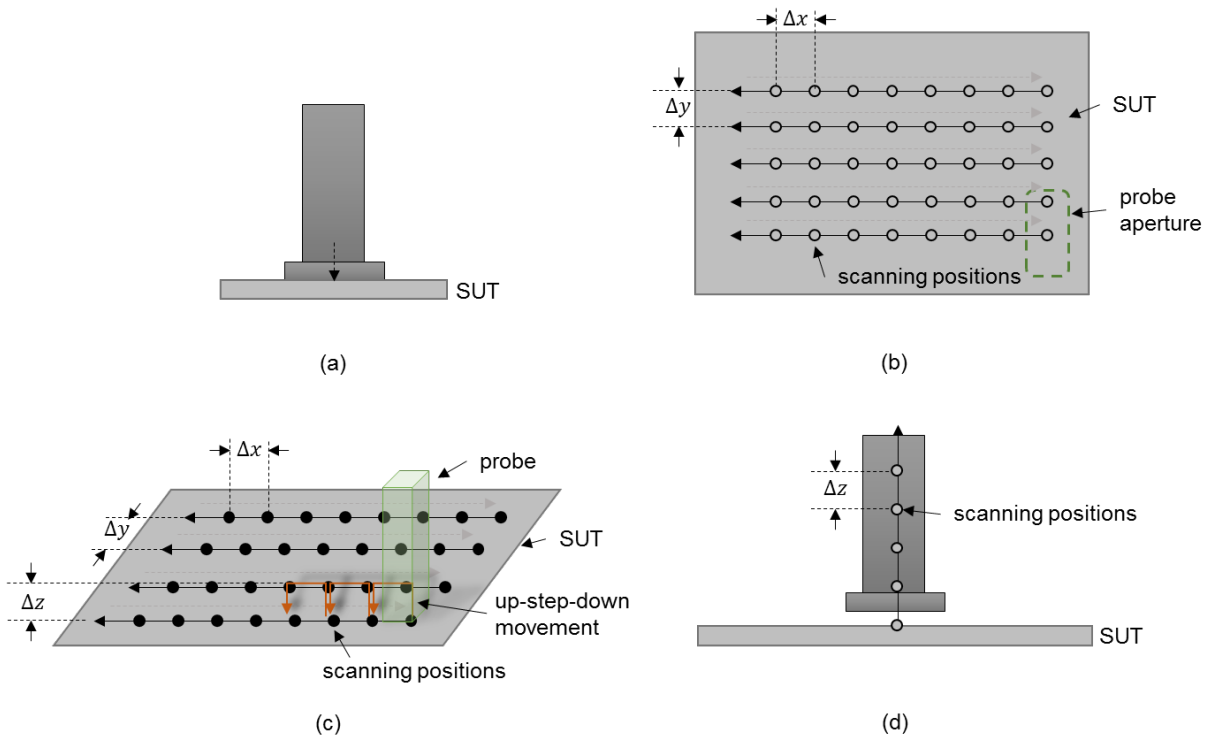


Figure 3.12 Four scanning operation modes: (a) probing (A-scan), (b) raster scanning (C-scan), (c) raster probing and (d) lift-off

In order to obtain responses from different geometric samples, four scanning operation modes including probing, raster scanning (C-scan), raster probing and lift-off, have been developed. The four scanning modes are presented in Figure 3.12. Among the four scanning modes, only the probing and raster scanning modes were practically used to obtain the data that analysed in this work. The rest have been used for feasibility studies. The raster probing mode has been exploited to mitigate the influence of lift-off while scanning an area. In the operating cycle of this mode, the probe will be lifted, stepped to the next position and dropped on the sample surface leaving no gap between the probe and the sample surface while obtaining the response. The lift-off mode elevates the probe position in step of Δz . It has been used to investigate the lift-off effect and analyse the optimal lift-off distance between the probe and particular samples.

3.3.3 Feature Extraction

Feature extraction transforms raw data into lower dimensions of informative signatures with the elimination of redundancy and uncorrelated information. The appropriated feature extraction methods should be concerned depending on the properties of data or signals. In this work, the data types obtained from microwave NDT&E system are in two formats: a wideband spectrum from probing (A-scan) and a spatial-spectral matrix (C-scan) includes scanning position $[x, y]$ and the corresponding wideband spectrum. The feature extraction applied in this works are listed as follows.

3.3.3.1 Fast Fourier Transform

Fast Fourier transform (FFT) is one of the standard methods to convert and analyse signals between time domain and frequency domain. The mathematical formulations of FFT and inverse FFT are the same as discrete Fourier transform (DFT), which are

$$X(e^{j\omega}) = \sum_{n=0}^{N-1} x(n)e^{-j\frac{2\pi}{N}kn}, k = 0, \dots, N-1 \quad (3.6)$$

$$x(n) = \frac{1}{N} \sum_{k=0}^{N-1} X(e^{j\omega})e^{j\frac{2\pi}{N}kn}, k = 0, \dots, N-1 \quad (3.7)$$

In equation (3.7), the N dimension is a power of two determined by the window size of the acquired signals. Based on the VNA selected in this project, the number of sampling frequencies can be configured to be 201, 401, 801 and 1601 and thus the N values are chosen to be 256, 512, 1024 and 2048, respectively.

3.3.3.2 Frequency domain Features

The primary features of spectral response are frequency domain features including peak frequency, peak frequency magnitude, average magnitude and average phase angle. Demonstrated in Figure 3.13, the peak magnitude and peak frequency are the standard features, especially, for applications of material characterisation as the resonant responses is varying by the microwave material properties including permeability μ , permittivity ε and conductivity σ (as the imaginary part of permittivity ε'') related to loss tangent. The average magnitude and average phase are useful in applications of microwave imaging [74], [207] where the dimensions of magnitude and phase of the spectrum are reduced to a pixel intensity in a reconstructed image. To reconstruct a feature image from the spatial-spectral responses, the average magnitude $\hat{g}(x, y)$ and average phase $\hat{\theta}(x, y)$ at pixel (x, y) are calculated as follows

$$\hat{g}(x, y) = \frac{1}{N} \sum_{i=1}^{i=N} |g_i(x, y)| \quad (3.8)$$

$$\hat{\theta}(x, y) = \frac{1}{N} \sum_{i=1}^{i=N} \angle g_i(x, y) \quad (3.9)$$

where i is a frequency index of the wideband signal $g_i(x, y)$ and N is a number of sampling frequencies.

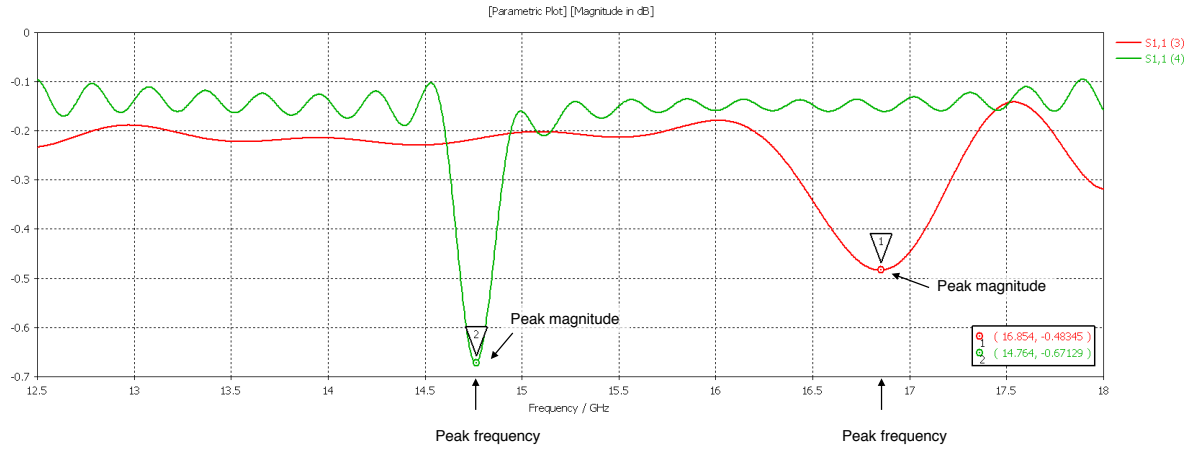


Figure 3.13 An example of microwave reflection coefficient response with peak magnitude and peak frequency features

3.3.3.3 Time-of-flight Feature

Time-of-flight is achieved by measuring the time difference or time delay between the transmitted and received signal directed towards layers or targets within a structure [208]. The depth of the objects or layers corresponds to the travel time between the transmitting and receiving signals [209]. The technique can be extended to microwave inspection. In this case, the transmitting waves from the waveguide probe are sent and the scattered reflection waves are obtained at a specific delay [154].

To accurately estimate the time-of-flight feature of the target, the reference signal is required. The reference signal can be calculated by known characteristics of excitation signals, antenna/probe radiation and transmit/receive channel. However, it is more practical to obtain the reference signal from a reflected signal of a plate of (nearly) perfect conductive reflector [210]. In the process of time-of-flight feature extraction, the reflected signal in time-domain (or inverse Fourier transform of wideband S11 in frequency domain) is preliminarily adjusted for the zero-timing reference eliminating early time interferences such as antenna coupling leakage and the dominant responses of surface reflection. Following this, the reflected signal $s[n]$ is applied with the matched filter of the reference signal $r[n]$, which is implemented by cross correlation as follows

$$f(n) = \sum_{n=0}^{N-1} s(n) * r(n) \quad (3.10)$$

where N is window size of the obtain signal, n is an index of discrete time domain signal. Envelopes of $f(n)$ are obtained by discrete Hilbert transform (DHT) calculated as following

$$DHT\{f(n)\} = g(k) = \begin{cases} \frac{2}{\pi} \sum_{n \text{ odd}} \frac{f(n)}{k-n}, & k \text{ even} \\ \frac{2}{\pi} \sum_{n \text{ even}} \frac{f(n)}{k-n}, & k \text{ odd} \end{cases} \quad (3.11)$$

The results of Hilbert transform are analytic signals of $f(n)$, which is the complex envelope of the original signal. Here, targets are identified from the presence of peaks and time-of-flight feature is extracted based on the peak magnitude and time at the peak position. The summary process of time-of-flight feature extraction is presented in Figure 3.14.

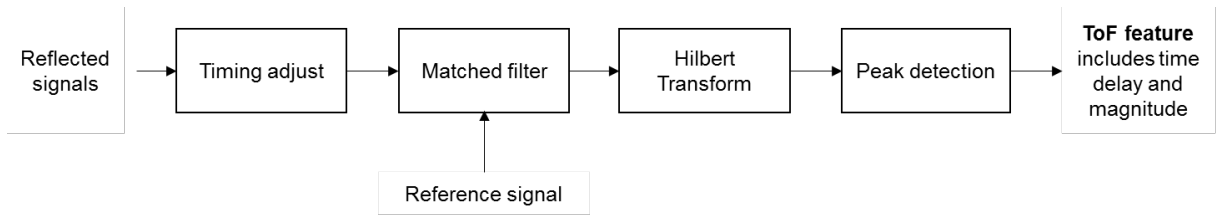


Figure 3.14 Time-of-flight feature extraction process for time domain signals

3.3.3.4 Principal Component Analysis

Principal component analysis has been widely used in feature extraction to reduce the data dimensions, while preserving prominent features and the correlation between the process variables. To extract dominant features (principal components, PC) as patterns from a multivariate training dataset, PCA decomposes principal components as a set of eigenvectors space retaining the maximum variance with minimizing the reconstruction error. The corresponding eigenvalues are scalar representing the degree of variance within the eigenvectors. The rank of eigenvalues represents the significant variance of the corresponding eigenvectors in the data set.

The process of PCA is shown in Figure 3.15, including two significant stages: training and testing. In the training stage, covariance matrices of sampling data of each sample sets are formed by subtraction of mean value from each of the data dimension resulting in a dataset of zero means. For M observations and N variables, the mean value is calculated by

$$\bar{X} = \frac{1}{M} \sum_{n=1}^M X_n \quad (3.12)$$

where X_n is the N dimensional column vector of the n -th observation. Then, the covariance matrix is calculated by

$$C = \frac{1}{M} \sum_{n=1}^M [(X_n - \bar{X}) \cdot (X_n - \bar{X})^T] = \frac{1}{M} A \cdot A^T \quad (3.13)$$

where

$$A = [(X_1 - \bar{X}), (X_2 - \bar{X}), \dots, (X_n - \bar{X})] \quad (3.14)$$

Since the data has N dimensions, the covariance matrix will be $N \times N$. The covariance matrix is decomposed to retrieve a matrix of eigenvectors, which is a set of principal components by

$$e_i = A\lambda_i \quad (3.15)$$

Once eigenvectors or principal components are found, then, they are sorted by eigenvalues in descending order. It is usual to ignore the low rank principal components (less significant PC). Only a few most significant PCs will be selected for contribution to the feature signals, and thus the data dimensions are reduced to lower dimensions. Finally, the feature signals can be identified as a linear combination of these PCs.

In the testing stage, the original data from the testing dataset are projected by the obtained transition matrix (projection matrix) yielding feature values of lower data dimensions. Figure 3.16 and Figure 3.17 show the feature value/image obtained from the projection of the transformation vector (selected significant PC) for the sampling spectrum of A-scan and C-scan, respectively.

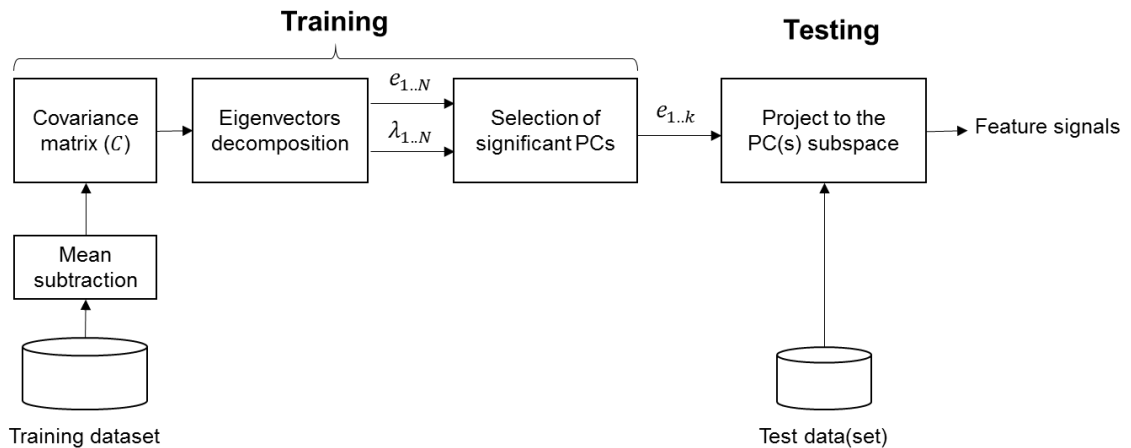


Figure 3.15 PCA for feature extraction

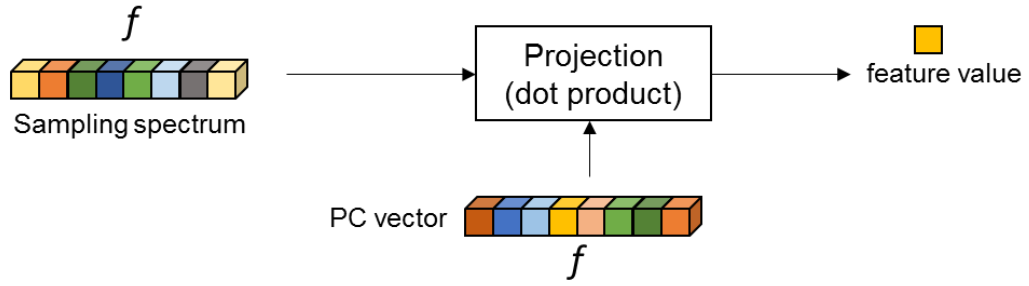


Figure 3.16 PC feature value extraction of a single spectrum response

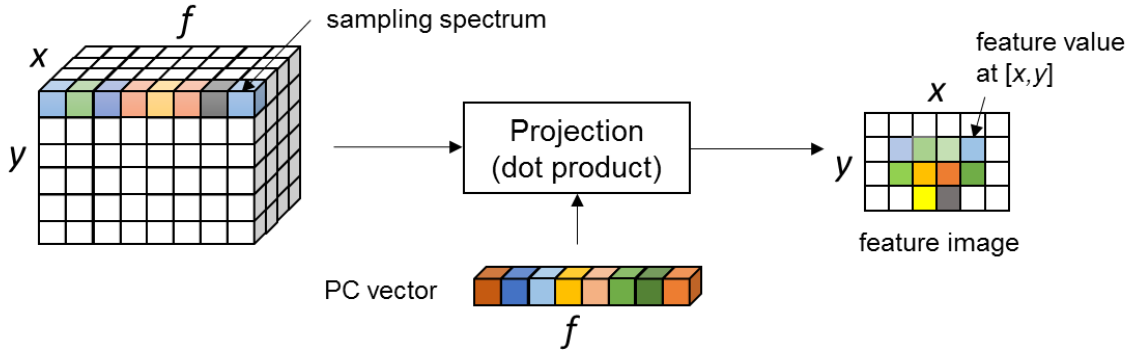


Figure 3.17 PC feature image extraction of spatial-spectral responses

3.3.4 Synthetic Aperture Radar Imaging

3.3.4.1 2-D SAR

Typical measurement setup for microwave imaging system is shown in Figure 3.18. Measurements using a monostatic OEW probe are performed on the $x'-y'$ plane over the target located on the $x-y$ plane with constant lift-off distance z_0 . The measurements at the aperture of a single probe position is considered as a real aperture, while combining the measurement of the scattered electric field at multiple locations is considered as synthetic aperture. The scattered responses obtained from the probe aperture and target are different depending on the lift-off distance. Compared with typical SAR application in remote sensing, SAR imaging for microwave NDT can operate closer to the target with tiny aperture size (open-ended waveguide), and thus the scanning area and positions are considerably known. Hence, the SAR imaging in NDT application is considered as a *re-focusing* technique. For a single frequency operation, each scanning position (x', y', z_0) , the OEW probe sends a set of sinusoidal signals at frequency f . Assuming that a target position $(x, y, 0)$ reflects incident waves with reflectivity function $g(x, y)$ and the measurement at the probe aperture is a reflectivity function $r(x', y')$. Based on the process of plane wave decomposition for spherical wave or ω - k algorithm [211], the reflectivity at the target position is given by

$$g(x, y) = \mathcal{F}_{2-D}^{-1}[R(k_{x'}, k_{y'})e^{-jz_0k_z}]$$

$$= \sum_{m=0}^{M-1} \sum_{n=0}^{N-1} R(k_{x'}, k_{y'}) e^{-j2\pi\left(\frac{k_{x'}}{M}x + \frac{k_{y'}}{N}y\right)} \quad (3.16)$$

$$R(k_{x'}, k_{y'}) = \mathcal{F}_{2-D}[r(x', y')] \quad (3.17)$$

$$\mathcal{F}_{2-D}[r(x', y')] = \frac{1}{MN} \sum_{m=0}^{M-1} \sum_{n=0}^{N-1} r(x', y') e^{-j2\pi\left(\frac{k_{x'}}{M}m + \frac{k_{y'}}{N}n\right)} \quad (3.18)$$

where $R(k_{x'}, k_{y'})$ is reflectivity in the wavenumber domain and k_z is the wavenumber in z axis related to frequency by the following equation

$$k_z = \sqrt{\left(\frac{4\pi f}{c}\right)^2 - k_x^2 - k_y^2} \quad (3.19)$$

From equation (3.19), k_z at edge frequencies of Ku-band probe (18 - 26.5 GHz) with $z_0 = 1$ mm are demonstrated in Figure 3.19. It can be seen that the increasing of frequency will increase wavenumber frequency in both k_x and k_y axes (circle). In case of wideband excitation, the OEW probe transmits swept frequencies $f \in [f_{min}, f_{max}]$, a step frequency Δf , and the number of frequencies $N = (f_{max} - f_{min})/\Delta f + 1$. The 2-D SAR can be done by calculating as a piece-wise for each frequency index i as the process presented in Figure 3.20.

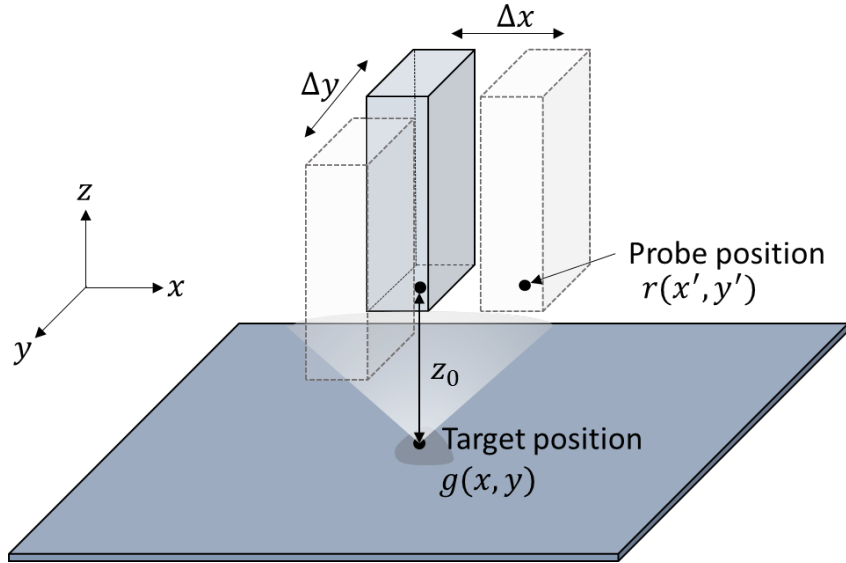


Figure 3.18 A monostatic OEW probe C-scan for 2-D SAR imaging

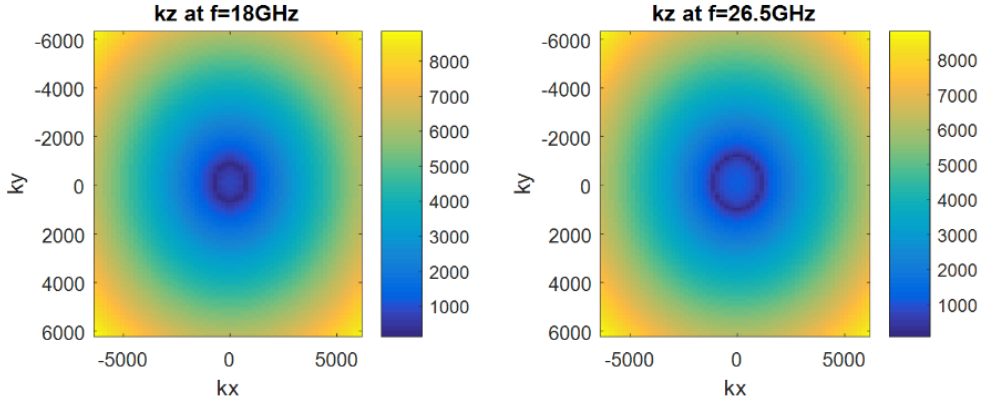


Figure 3.19 Dispersion in $|k_z|$ for plane wave decomposition using ω - k algorithm

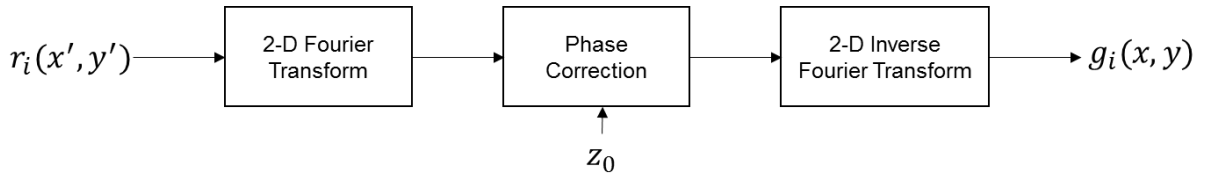


Figure 3.20 2-D SAR processing for wideband signal

3.3.4.2 SAR Tomography

SAR tomography imaging or tomographic SAR is a visualisation technique that facilitates estimation of target depth using time information derived from wideband signals. The time information is given by the reflected waves from the discontinuity of dielectric properties or consistency of metallic objects. In order to obtain time information, the excitation signal is configured to be either impulses or equivalent wideband signal using a frequency sweep generator. Presented in Figure 3.21, the OEW probe sends wideband signals with frequencies $f \in [f_{min}, f_{max}]$, a step frequency Δf , and the number of frequencies $N = (f_{max} - f_{min})/\Delta f + 1$. The wideband reflectivity of the target position and aperture positions are denoted by $g(x, y, f)$ and $r(x', y', f)$, respectively. The initial processes of SAR tomography is similar to that of 2-D SAR imaging, however, the results are in form of 3-D spatial-temporal matrix by applying additional inverse discrete Fourier transform of the $g(x, y, f)$ as demonstrated in [74]. Therefore, the 3-D SAR tomography processing (see Figure 3.22) is given by

$$g(x, y, t) = \mathcal{F}_{3-D}^{-1}\{\mathcal{F}_{2-D}[r(x', y', f)]e^{-jz_0k_z}\} \quad (3.20)$$

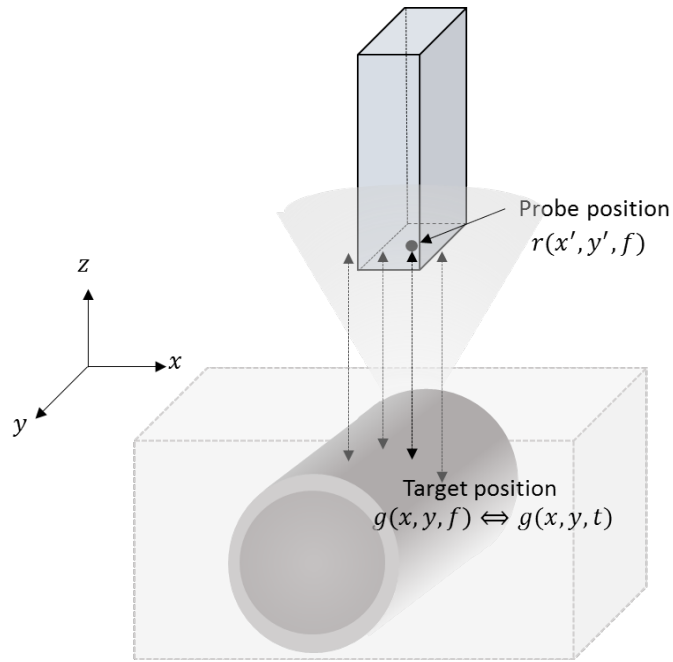


Figure 3.21 A monostatic OEW probe C-scan for SAR Tomography

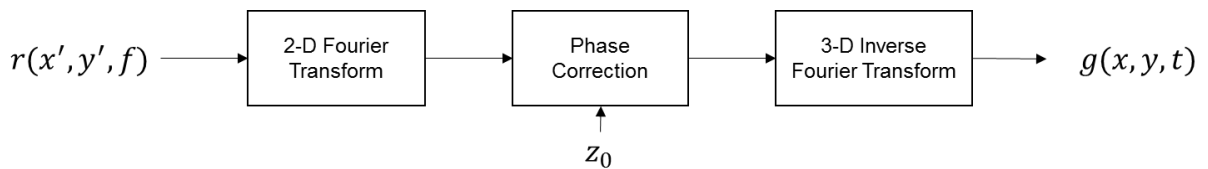


Figure 3.22 SAR-tomography processing

3.4 Chapter Summary

This chapter described the theoretical background of microwave NDT&E system for multilayered structures. Geometric configuration topologies based on three dedicated models are discussed. The design and development of microwave NDT&E system used in this thesis have been thoroughly explained and identified.

The following chapters of the thesis will demonstrate the experimental studies carried out and the efficient solutions developed to overcome the challenges identified. Interesting results with critical discussion are provided.

Chapter 4 Steel Corrosion Stages Characterisation

In the previous chapter, the theory related to microwave NDT using open-ended waveguide was outlined. This section will look into the experimental studies of characterisation capabilities for steel corrosion progression stages. Firstly, the corrosion models and corrosion progression samples used in this experimental study have been outlined along with the signal processing and feature extraction methods. In order to determine the progression of corrosion related to the thickness and permeability changes, the feature extraction methods and the selection of the features for both the coated and the uncoated samples are discussed further. All the features are extracted, compared and validated.

The first study demonstrates the ability of microwave open-ended waveguide system to not only distinguish between corroded and non-corroded steel, but also different corrosion progresses based on the characteristic of resonant responses. The second study is focused more into feature extraction method for corrosion progression features of the coated and uncoated corrosion samples which were naturally exposed in the marine atmospheric area in different times. Then, several principal component features have been investigated and compared followed by the selection of the principal components upon which most correlated to corrosion progression in comparison to the principal components. Finally, to analyse the influences of surface texture and surface roughness, the results from other principal components at different probe orientation are further discussed and explained.

4.1 Open-ended Rectangular Waveguide Measurement

Based on the microwave responses of the corrosion [105], two sizes of open-ended waveguide probes: WR-62 and WR-42 operating in a frequency range between 9.5 – 26.5 GHz, have been chosen in our experiment. The specification of WR-62 and WR-42 probes and the cut-off frequencies calculated by Equation (3.1) are shown in Table 4.1.

Table 4.1 The properties of WR-62 and WR-42 probes in the TE_{10} mode

Probe no.	Dimensions $a \times b$ (mm)	Normal operating frequencies (GHz)	Cut-off frequency (GHz)
WR-62	15.80 x 7.90	12.4 – 18.0	9.5
WR-42	10.67 x 4.32	18.0 – 26.5	14.1

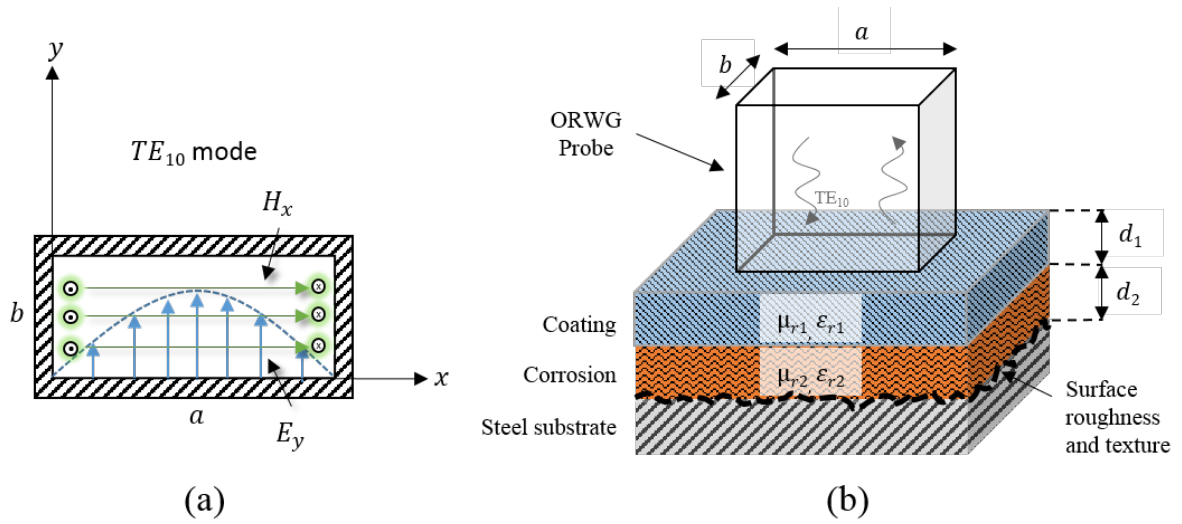


Figure 4.1 (a) Open-ended waveguide field distribution in TE_{10} mode, and (b) a corrosion model of corrosion under coating

In this work, the open-ended waveguide probes are excited in the dominant TE_{10} mode. Reflection coefficient (S_{11} or Γ) related to a coupling between the termination impedance of the probe Z_{WG} and impedance at the interface of the testing sample Z_{in} is given by

$$\Gamma = (Z_{in} - Z_{WG}) / (Z_{in} + Z_{WG}) \quad (4.1)$$

The model of corrosion undercoating is considered as two dielectric layers backed by the metallic substrate as illustrated in Figure 4.2. The interaction between the layered structure and incident waves occurs in the near field of the probe where the electrometric field responses are complex. In general, the reflection coefficient is a function of probe dimensions a and b , operating frequency f , relative permittivity ϵ_{r1} and ϵ_{r2} , relative permeability μ_{r1} and μ_{r2} , and layer thicknesses $d1$ and $d2$. As mentioned in the previous section, many investigators have methodically worked towards developing full-wave models to describe the complex interaction of nearfields of a waveguide probe with layered structures. In contrast to the model-based inversion, this work is based on experimental studies of spectral responses obtained from corrosion progression samples. A statistical-based PCA method is not intended to determine actual parameters such as corrosion thickness and its material properties but is applied for feature extraction of a multivariate parameter such as corrosion progress. It is expected that the selected PCA based features can be used for quantitative non-destructive evaluation of the corrosion progression stages regardless of model analysing and parameters estimation. Three sets of dedicated samples are used for PCA training and testing robustness of selected PC-based features.

4.2 Corrosion Samples

To study corrosion progress together with the influences of the coating layer and surface condition, three dedicated sets of samples were selected. The samples have been prepared as follows.

4.2.1 Uncoated Corrosion Samples

The uncoated corrosion samples shown in Figure 4.2, were prepared as follows: firstly, a plate of un-corroded mild steel (S275) was cut into pieces of 300 mm x 150 mm x 3 mm (length x width x thickness). After cutting, the whole plates were covered with plastic tape excluding the central area of 30 mm x 30 mm to let corrosion develop. Finally, they were exposed to the marine atmosphere at different periods of 1, 3, 6, 10, and 12 months (UP1, UP3, UP6, UP10, and UP12). It is noted that the sample UP0 used in this study is a measurement of the un-corroded area of the UP1 sample.

4.2.2 Coated Corrosion Samples

Initially, these samples were prepared using the same process as of the UP samples. They were coated by non-conductive (dielectric) paint with the average thickness of 100 μm resulting in products of coated corrosion progression samples (CP1-CP12) as shown in Figure 4.3. It is noted that the sample CP0 is a measurement of the coating area without corrosion of the CP1 sample.

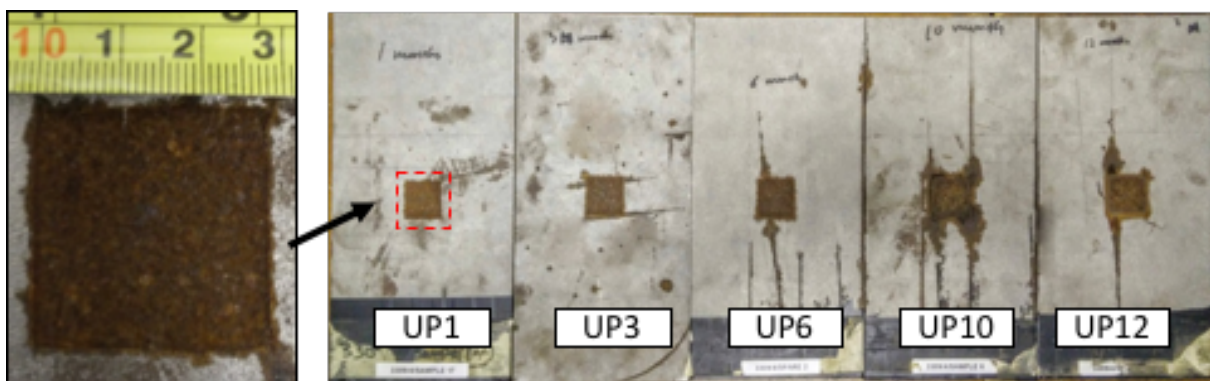


Figure 4.2 Uncoated corrosion progression samples

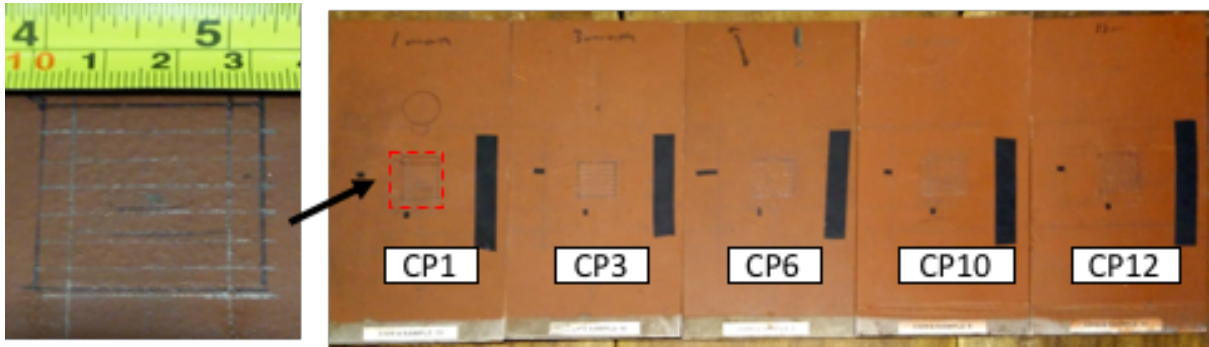


Figure 4.3 Coated corrosion progression samples

4.2.3 Surface Preparation Samples with Corroded Surface

The surface preparation samples shown in Figure 4.4, were prepared as follows: initially, three out of four steel plates (US2-US4), sizing of 300 mm x 100 mm, were placed in an environmental test chamber, which simulates marine atmospheric condition for a month to accelerate the corrosion progress over the samples. Following this, the surface of each sample has been treated differently according to Steel Structures Painting Council (SSPC) standard [212]. The final products of samples with different surface roughness are measured by laser profilometry. The US sample properties are described in Table 4.2.

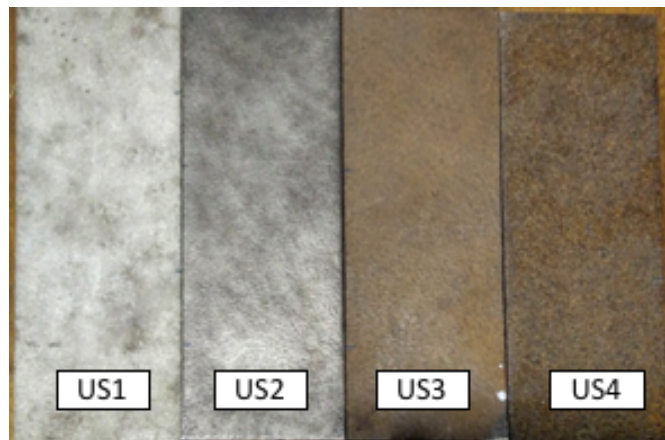


Figure 4.4 Surface preparation samples range

Table 4.2 Properties of surface preparation samples

Sample No.	Preparation Method	Average Thickness (mm)	Average Roughness (μm)	Presence of Corrosion
US1	SP10	4.077	18.3	No
US2	SP11	3.898	16.1	No
US3	SP2	4.142	29.1	Yes
US4	Unprepared	4.429	56.7	Yes

4.3 Experimental Setup

Equipment setup of microwave ORWG system for corrosion stages characterisation is shown in Figure 3.9. The hardware system is composed of an X-Y-Z scanner (High-Z S-720), a vector network analyser (Agilent PNA E8363B) and a computer connected to the VNA through a general propose interface bus and through to the scanner via a parallel port interface. The scanner has been programmed to deploy the waveguide probe positioning over the testing samples. Before the measurement, the VNA together with the coaxial cable was calibrated using a calibration kit (open, short and load). The calibration results are used to compensate the cable characteristic and delay of the channel.

Table 4.3 Measurement parameters

Parameter	Value
Type and number of samples	UP – uncoated corrosion progression (6) CP – coated corrosion progression (6) US – uncoated surface preparation (4)
Probe no. / frequency range	WR-62 / 12.0 -18.0 GHz (UP and US) and 9.5 - 18.0 GHz (CP) WR-42 / 18.0 - 26.5 GHz
Frequency points	1601
Probe orientation	0° and 90°

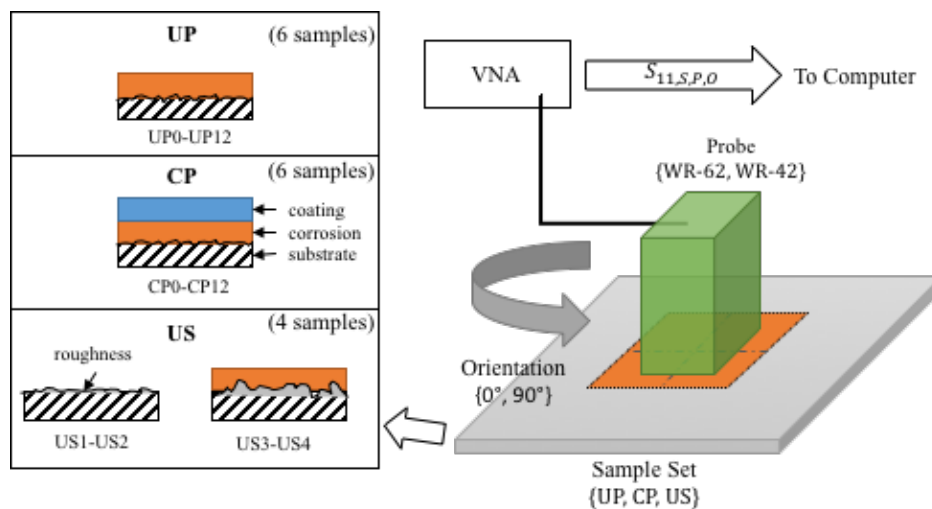


Figure 4.5 experiment for obtaining reflection coefficients over corrosion samples

Three experiments with three sets of samples are conducted in this study as described in Table III. For each set of samples, reflection coefficients are sampled ten times at slightly different positions (about 0.2 mm) of the corrosion patch centre with 0° and 90° orientations using WR-62 and WR-42 probes. Amount of measurements performed for each set calculated by a number of samples in each set × probes × orientations are 240, 240 and 160 for samples UP, CP and US, respectively. In these sampling data, seven out of ten are used for PCA training; while the rest are used to test selected principal components. It is noted that the operating frequency of WR-62 probe of CP samples is extended to the cut-off frequency at 9.5 GHz to capture the shifted frequency responses caused by the coating material. It is known that the operating frequency closing to the cut-off is not recommended, as it is highly dispersive due to an abrupt change of phase velocity or group delay. However, the quantities analysed in this work are only the magnitude response $|S_{11}|$, which is independent to phase variation and thus invariant to the phase dispersion. Moreover, unlike pulsed radars, the operation of VNA will transmit single frequency or very narrow band FMCW signals at a time in a sweeping manner. Therefore, the obtained magnitude responses from VNA are unlikely to be affected by waveguide dispersion.

4.4 Experimental Results and Discussion

In this section, reflection coefficient spectra obtained from three sample sets are presented. Three most contributed principal component PC1-PC3 are chosen to test for feature extraction of corrosion progression. The projected values of PC1-PC3 to testing data are analysed. Finally, we discuss other measurement influences such as probe orientation and surface condition.

4.4.1 Spectral Responses of Corrosion

The magnitude responses obtained from 7 slightly different sampling positions of UP and CP samples with different probes and orientations are shown in Figure 4.6 and Figure 4.7. It can be seen that the spectra of the WR-62 probe, Figure 4.6 (a)-(f) and Figure 4.7 (a)-(f), show single resonant responses while that of the WR-42 probe, Figure 4.6 (g)-(l) and Figure 4.7 (g)-(l), show multiple resonances and ripples. Also, the variations of response in the resonant region are significantly higher than the flat response region. The differences in the responses of two probes are caused by the interaction between signal coherence, thickness and material properties at different probe dimensions and operating frequencies. Moreover, the unwanted ripples could be generated by the interrogation between the sample and the edge of unmodified finite flange probe [213]. Besides, it is found in general that the influence of probe orientation is very little in the beginning progress up to 6 months and becomes more significant in the 10 and 12 months.

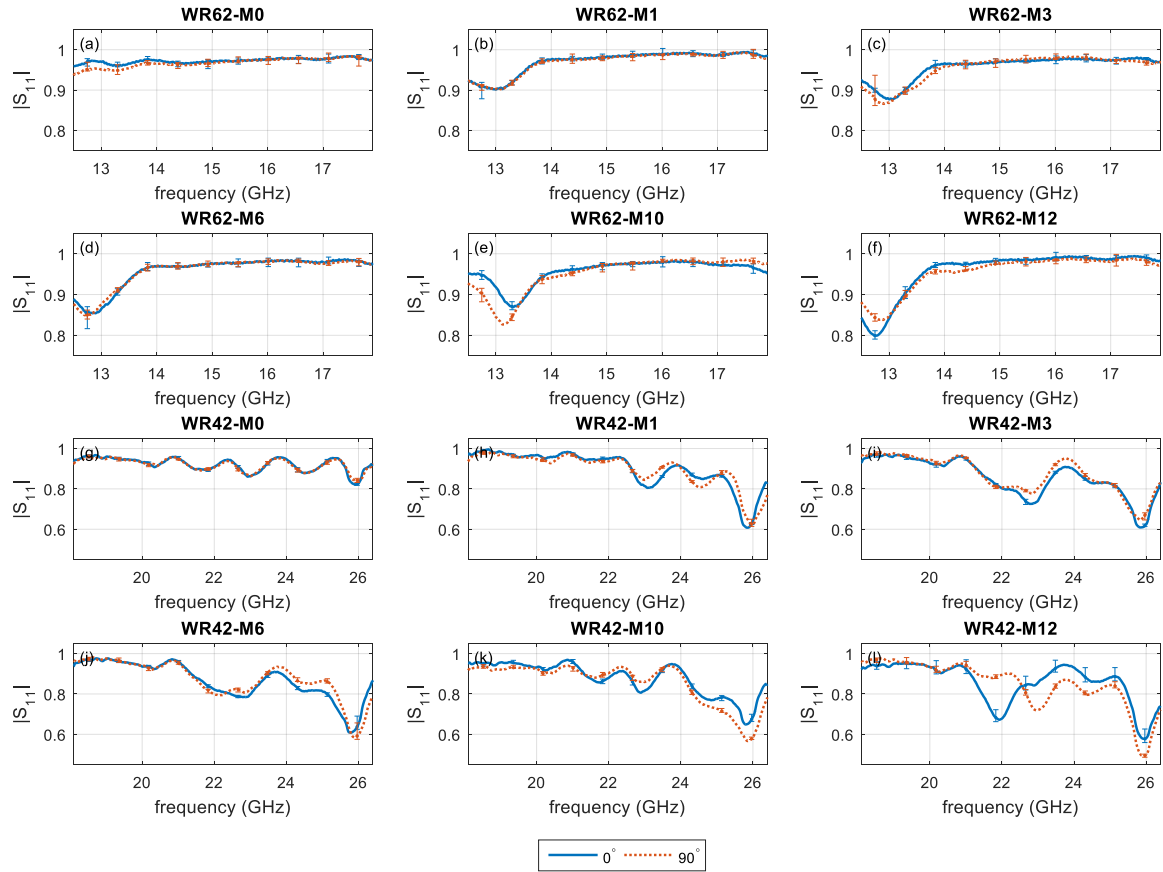


Figure 4.6 Average magnitude responses of UP samples obtained by WR-62: (a) M0, (b) M1, (c) M3, (d) M6, (e) M10, (f) M12 and WR-42: (g) M0, (h) M1, (i) M3, (j) M6, (k) M10, (l) M12.

To study the influences of the coating layer only, reflection coefficients are obtained from the CP samples in the area outside corrosion patch. The sampling data are labelled as C1-C12 according to the CP1-CP12 samples. Although these samples have been painted with the same coating material, the thicknesses of the coating layer in each sample may be varying due to the manufacturing uncertainty. From the responses of the WR-62 probe shown in Figure 4.8(a), it is found that the resonant frequency of all sampling data is consistent at around 10.5 GHz demonstrating highly dependent on the coating material, whilst resonant magnitudes are varied by coating thicknesses. On the other hand, the responses of the WR-42 probe in higher frequency shown in Figure 4.8(b) demonstrate complex responses of multiple resonances similarly to that of the CP samples.

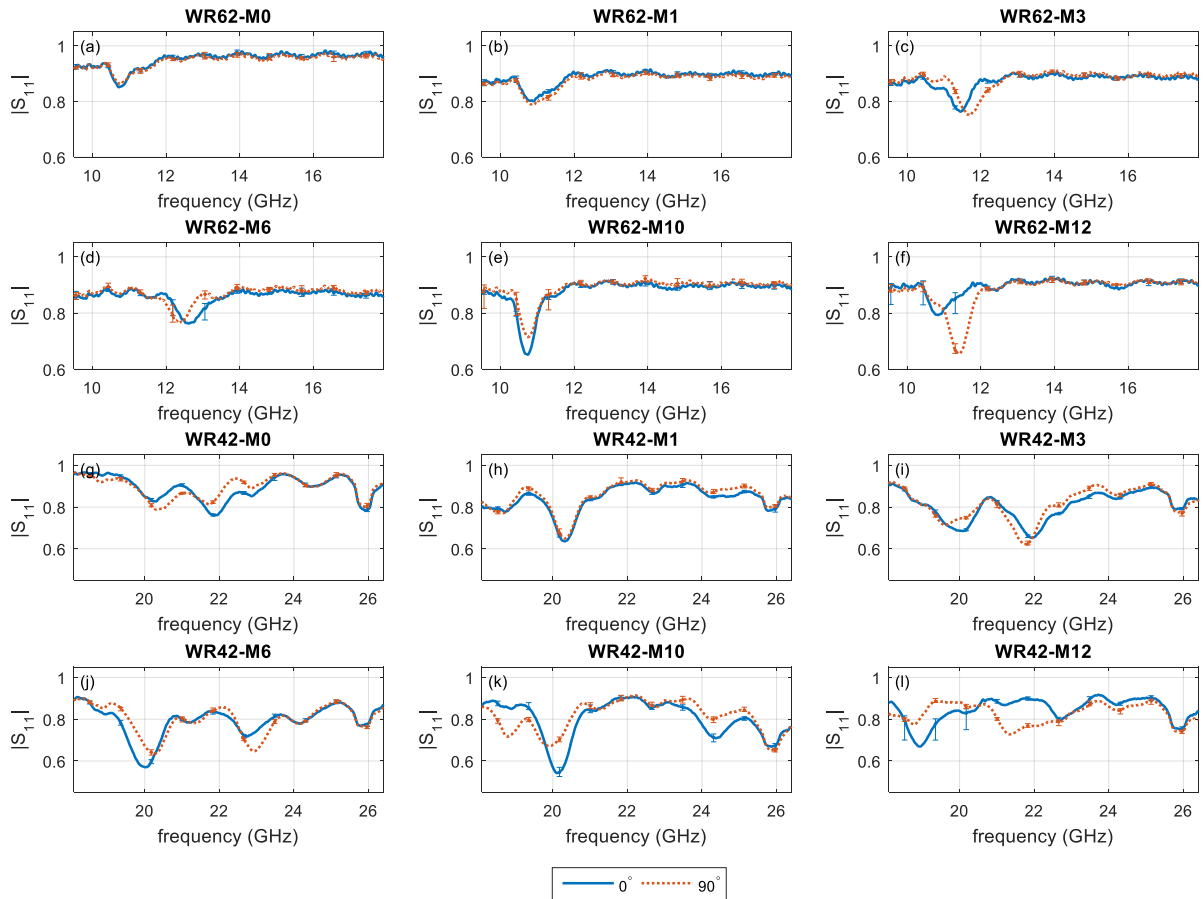


Figure 4.7 Average magnitude responses of CP samples obtained by WR-62: (a) M0, (b) M1, (c) M3, (d) M6, (e) M10, (f) M12 and WR-42: (g) M0, (h) M1, (i) M3, (j) M6, (k) M10, (l) M12.

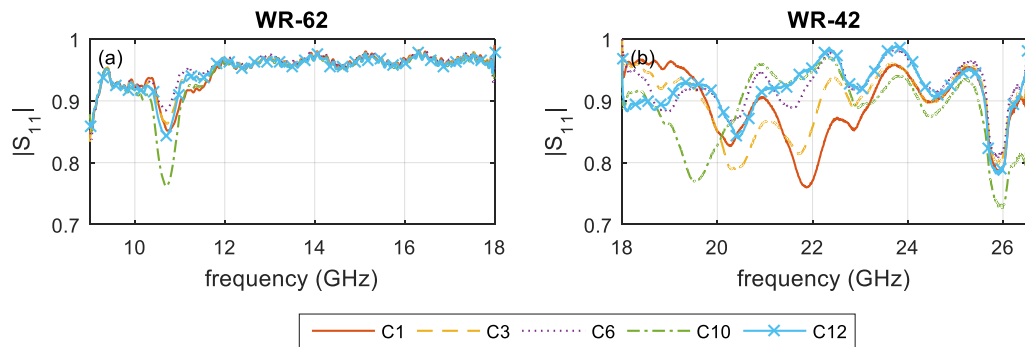


Figure 4.8 Average magnitude of the reflection coefficients of the coating layer from CP samples (C1-C12) measured by (a) WR-62 and (b) WR-42.

In the study of the surface influence of US samples, the responses of WR-62 probe plotted in Figure 4.9(a)-(d) show no significant variation at different orientations. However, the samples US3 and US4, which are the samples with presences of corrosion, demonstrate strong resonant response similar to that of the UP samples. Figure 4.9(e)-(h) show responses of US samples

measured by the WR-42 probe. Moreover, the influence of orientation is only recognisable in the samples US3 and US4 which are corroded samples.

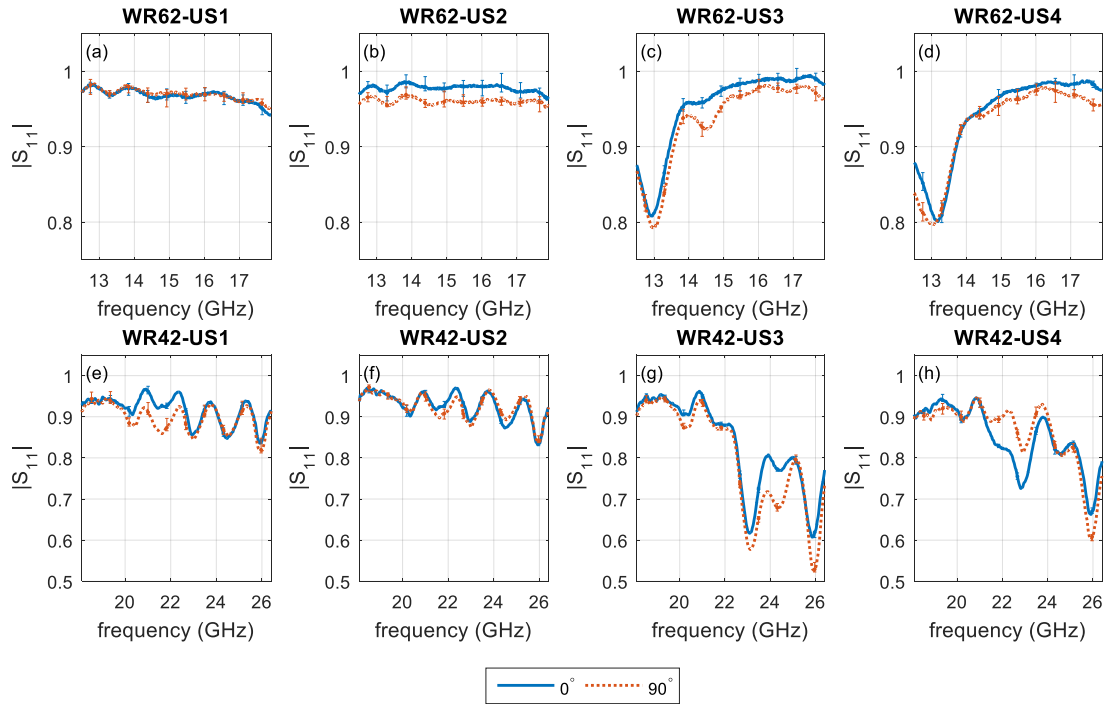


Figure 4.9 Average magnitude responses of US samples obtained by WR-62: (a) US1, (b) US2, (c) US3, (d) US4 and WR-42: (e) US1, (f) US2, (g) US3, (h) US4.

Nevertheless, it is difficult to analyse the complex responses of spectral feature (1601 frequency components) and identify distinguish parameters. Hence, PCA is applied to extract major principal components from the training responses. It is expected that one of the obtained principal components can be used to extract a feature that represents corrosion progression.

4.4.2 PCA for Feature Extraction of Corrosion Progress

To extract the corrosion progression parameter from the training data, the PCA method is applied to decompose principal components. The process of PCA shown in Figure 4.10 includes two significant steps: training and testing. In training step, covariance matrices of sampling data of each sample sets are formed and categorised by the measurement probe and then calculate roots of eigenvectors e_i and corresponding eigenvalues λ_i using Eigenvector decomposition. The eigenvectors sorted by descending order of eigenvalues are called principal components. According to the cumulative percentage of variances $(\lambda_i / \sum_{i=1}^n \lambda_i)$, usually, only a few most contributed k principal components are chosen to test for the major contributed parameter. In the testing step, the sampling data from the testing dataset are projected to the k chosen PCs. The projected value, which is a linear combination between PC coefficients and sampling data,

represents a PC feature. One of the major PCs having its projected values most correlated among corrosion datasets will be chosen for feature extraction of the corrosion progression. Besides, the influences of inhomogeneity in material and surface conditions are also studied through comparison of PC features at 0° and 90° .

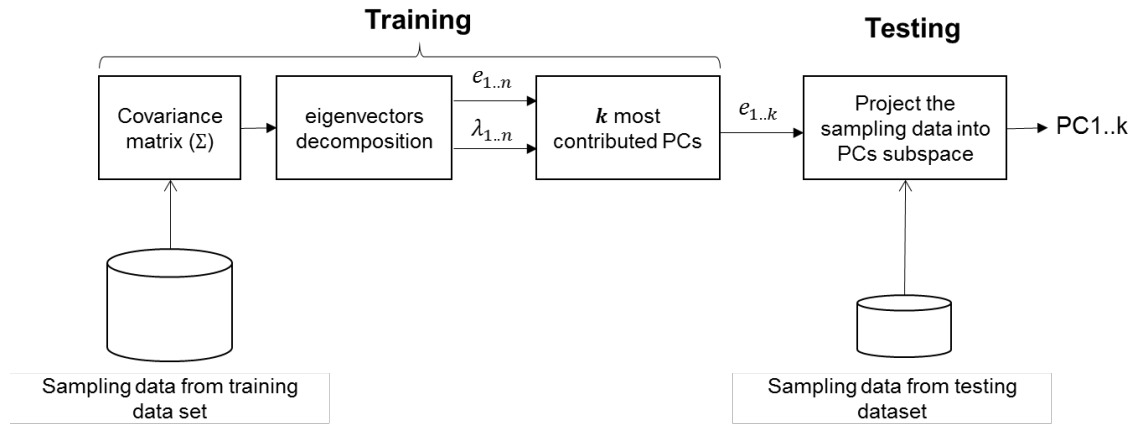


Figure 4.10 PCA for feature extraction of corrosion progression

PCA is applied to extract and analyse the significant contributed parameters from high-dimensional features (1601 sampling frequency points). The summations of the percentage of variance of the first three principal components of each dataset are higher than 90%, therefore in our study, only PC1-3 are selected for feature extraction. The high percentage of variance of the first three PCs also indicates that the sampling data in each dataset are significantly correlated and should be sufficient to extract the significant contributed parameter. To identify the corrosion progression features from the selected PCs, three sampling data from the test dataset are projected to the selected PC1-3 vectors of their own set.

4.4.3 PCA Results Comparison and Discussion

The projected values of PC1-3 are plotted in Figure 4.11; the standard deviations of projected values based on 6 sampling data in each progression (3 sampling by 2 orientations) are shown in Table IV. Concerning orientation, it is found that the deviations of PC1-3 features between 0 to 6 months are insignificant. Whilst the variations are stronger in 10 and 12 months, specifically, the UP samples. The results may be explained by the fact that corrosion at the surface of UP10 and UP12 have been flaked-off. Thus, it introduces random roughness and inhomogeneity in these samples.

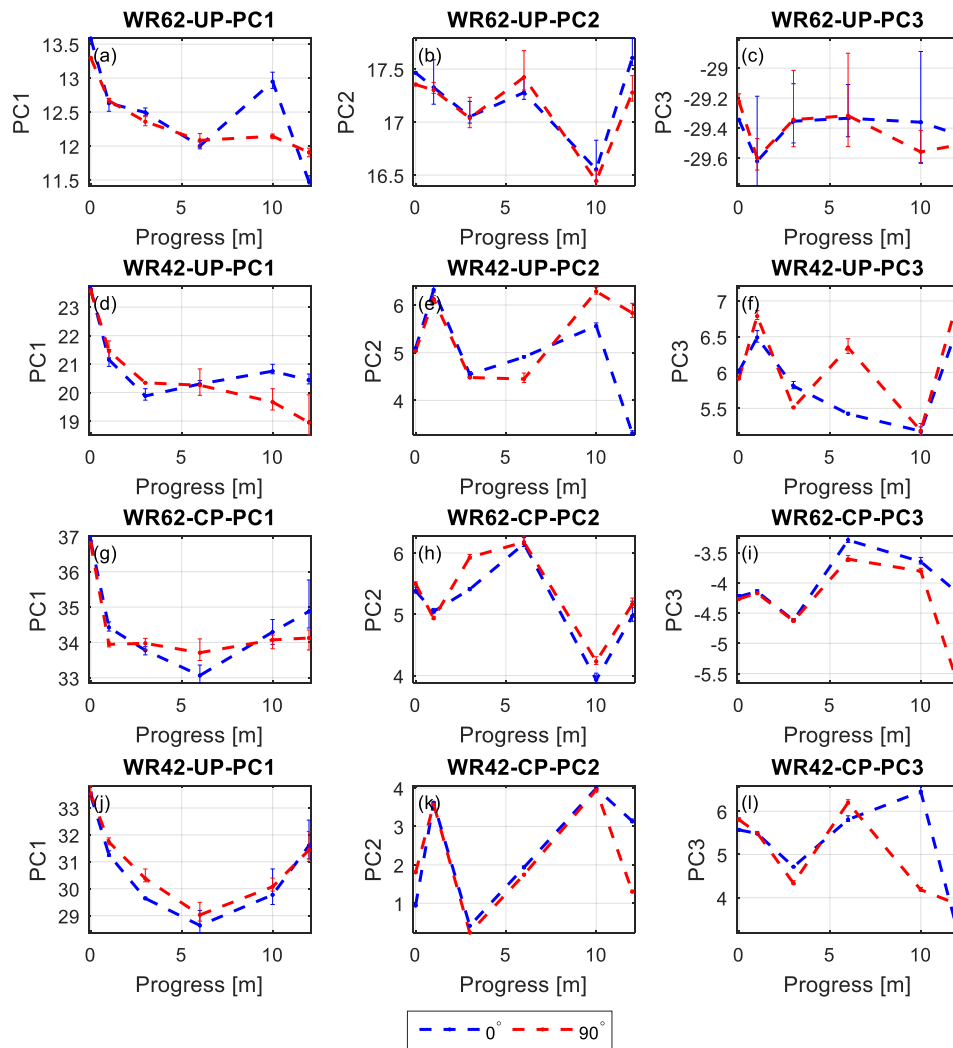


Figure 4.11 PC1-PC3 projected values of UP samples: (a) WR-62 PC1, (b) WR-62 PC2, (c) WR-62 PC3, (d) WR-42 PC1, (e) WR-42 PC2, (f) WR-42 PC3; PC projected values of CP samples: (g) WR-62 PC1, (h) WR-62 PC2, (i) WR-62 PC3, (j) WR-42 PC1, (k) WR-42 PC2 and (l) WR-42 PC3.

Table 4.4 Standard deviations of uncoated (UP) and coated (CP) corrosion samples at 0° and 90°

Sample	PC	Probe No.	M0	M1	M2	M6	M10	M12
UP	PC1	WR-62	0.16	0.07	0.09	0.09	0.45	0.25
		WR-42	0.05	0.24	0.27	0.2	0.62	0.88
	PC2	WR-62	0.06	0.09	0.08	0.12	0.11	0.2
		WR-42	0.03	0.11	0.04	0.26	0.4	1.38
	PC3	WR-62	0.07	0.16	0.13	0.15	0.19	0.14
		WR-42	0.06	0.17	0.16	0.51	0.04	0.21
CP	PC1	WR-62	0.13	0.28	0.17	0.45	0.29	0.67
		WR-42	0.11	0.27	0.42	0.31	0.39	0.39

Sample	PC	Probe No.	M0	M1	M2	M6	M10	M12
	PC2	WR-62	0.07	0.06	0.29	0.05	0.17	0.14
		WR-42	0.47	0.02	0.1	0.11	0.04	1
	PC3	WR-62	0.03	0.02	0.02	0.18	0.09	0.81
		WR-42	0.13	0.02	0.21	0.22	1.24	0.33

The deviations of PC1-3 features extracted from the three test samples are shown by min/max lines in Figure 4.11. It is found, in general, that deviations are quite noticeable in particular the PC1 features. The discrepancy could be attributed to higher variation in the resonant region representing corrosion responses. Moreover, it is evident that the deviation of PC2 and PC3 features in Figure 4.11(b) and (c) are relatively high. It is due to the high correlation and least complex responses of UP samples obtained by WR-62 probes demonstrated in Figure 4.6(a)-(f). Hence, PC1 mainly contributes to the percentage of variance while the lower PCs could be regarded as the noise subspaces.

Interestingly, the plots of PC1 projected values against corrosion progress of UP and CP samples of both probes demonstrated in Figure 4.11(a), (d), (g) and (j), render highly correlated curves that could represent the common parameter, which is corrosion progress. The agreement between PC1 projected values indicates that the PC1 features are independent of the probe and coating parameters (i.e., operating frequency f , probe dimensions a/b , coating thickness and properties). Moreover, it is found that the characteristic of the PC1 features is in line with the previous corrosion study using ultra high frequency radio frequency identification (UHF-RFID) and PCA of the same samples [214]. In the low frequency electromagnetic method such as PEC [22], a corrosion progression feature has been found corresponding to corrosion thickness and metal loss affecting the average conductivity and permeability. Although the corrosion feature of PEC demonstrates a monotonic relationship to the corrosion progress, its sensitivity is low due to the influence of the conductive substrate. In contrast, microwave is sensitive to changes in dielectric properties caused by the chemical process [10], [215]. The measurement results are related to the impedance matching between probe aperture and the dielectric layers including coating and corrosion layers with little influence of the conductive substrates (microwaves are totally reflected at the metallic interface). Nonetheless, microwave signals are more sensitive to the structural influences such as material inhomogeneity or surface roughness [216], [217], hence an advanced data analysis method is required for feature extraction.

For US samples, the plots of PC1-3 projected values and the corresponding standard deviations are shown in Figure 4.12 and Table 4.5. It is obvious in the results that the PC1 represents

corrosion feature as demonstrated by distinct values between US1/US2 and US3/US4. However, the influence of orientation is insignificant in PC1 but can be noticeable in PC2 and PC3 features. It is worth to continue investigating in the future work with more dedicated surface samples (e.g., surface roughness and manufacturing process with different directional texture).

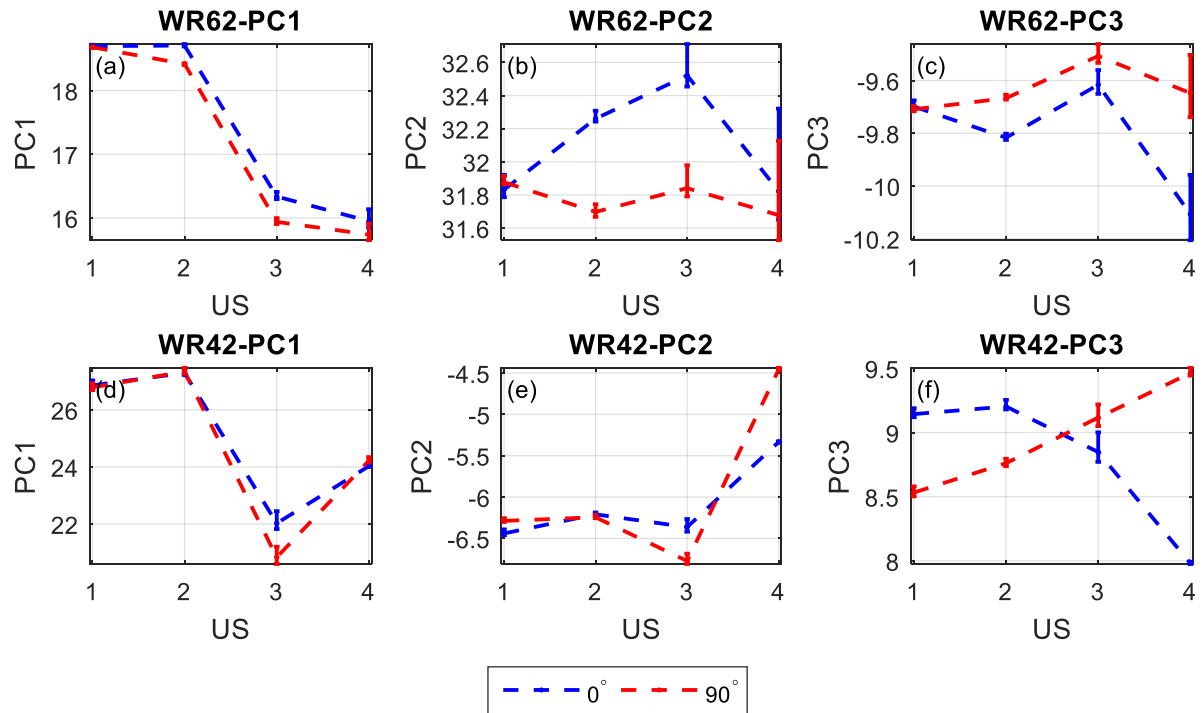


Figure 4.12 PC1-PC3 projected values of US samples: (a) WR-62 PC1, (b) WR-62 PC2, (c) WR-62 PC3, (d) WR-42 PC1, (e) WR-62 PC2, (f) WR-62 PC3.

Table 4.5 Standard deviations of uncoated surface preparation (US) samples at 0° and 90°

Sample	PC	Probe No.	US1	US2	US3	US4
US	PC1	WR-62	0.02	0.16	0.22	0.18
		WR-42	0.09	0.08	0.68	0.11
	PC2	WR-62	0.04	0.31	0.38	0.26
		WR-42	0.09	0.02	0.23	0.48
	PC3	WR-62	0.01	0.08	0.06	0.26
		WR-42	0.34	0.24	0.16	0.81

4.5 Chapter Summary

In the first study, two microwave open-ended rectangular waveguide probes are investigated with coated/uncoated corrosion progression and surface preparation samples for corrosion

stages characterisation. The responses of obtained reflection coefficients are analysed for corrosion progression feature using PCA. Unlike the model-based regression methods, our proposed method is not intended to identify actual corrosion parameters such as thickness and complex dielectric properties of corrosion. As the PC-based feature is only used as an indicator of changes of the corrosion progression stages. The microwave inspection method using open-ended waveguide probe and PCA is a promising tool for steel corrosion stages characterisation. The interaction between ORWG probe and corrosion layer is highly sensitive as resulting in variation of resonant responses. PCA is applied to extract the corrosion progression feature from the responses. It is found that the PC1 features are independent of probe and coating parameters and can be used to characterise corrosion progression stages.

Based on the investigation of ORWG probes at different operating frequencies, it is found that the responses from WR-62 probe operating at a frequency range between 9.5 GHz – 18 GHz are steadier for both coated and uncoated corrosion. The WR-42 probe, on the other hand, gives multiple resonances and is sensitive to other influences such as surface roughness as indicated in the PC3 features of the US samples. As indicated in Figure 4.11(a), (d), (g) and (j), a turning point at around 6 months is found of the PC1 features. The initial falling trend is likely to be related to the increasing of corrosion thickness in early corrosion stages, whereas the influence of material properties becomes stronger and causes reverse inclination in the latter stages.

Chapter 5 Detection and Characterisation of Impact Damage on Woven CFRP

In the previous chapter, a case study of the characterisation of steel corrosion under coating was investigated based on homogenous layered structures. This section will extend the microwave NDT study for capabilities to detect and characterise defect within inhomogeneous composite; i.e., impact damage on the woven carbon fibre reinforced composite. Firstly, models woven CFRP with different structures are studied using numerical simulation to understand the influences of woven carbon parameters such as yarn width, thickness, gap and number of laminate layers. Secondly, experimental studies of C-scan over woven CFRP with impact damage are undertaken to study an optimal scanning step size. The experimental results are also compared with the simulation results to study the relationship between impact damage and structural changes within the composites. Finally, the feature extraction framework for impact damage with the elimination of texture influence is presented.

5.1 Simulation Studies of Woven CFRP models

This work investigates microwave responses of woven composites through simulation and experimental studies of microwave OEW measurement in K-band (18-26.5 GHz). Models of woven CFRP and composite structures shown in Figure 5.1, are developed for simulation studies upon the relationship between microwave open-ended waveguide responses and CFRP structural parameters (i.e., width, gap, thickness and number of layers). The S11 responses are obtained by CST frequency domain solver in frequency range between 18-26.5 GHz.

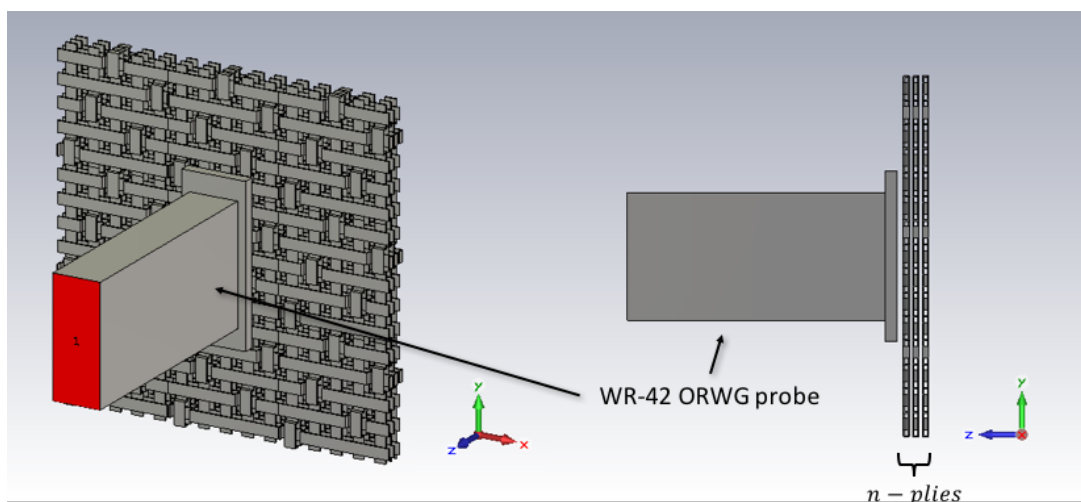


Figure 5.1 Simulation models of three plies 5HS CFRP and open-ended waveguide

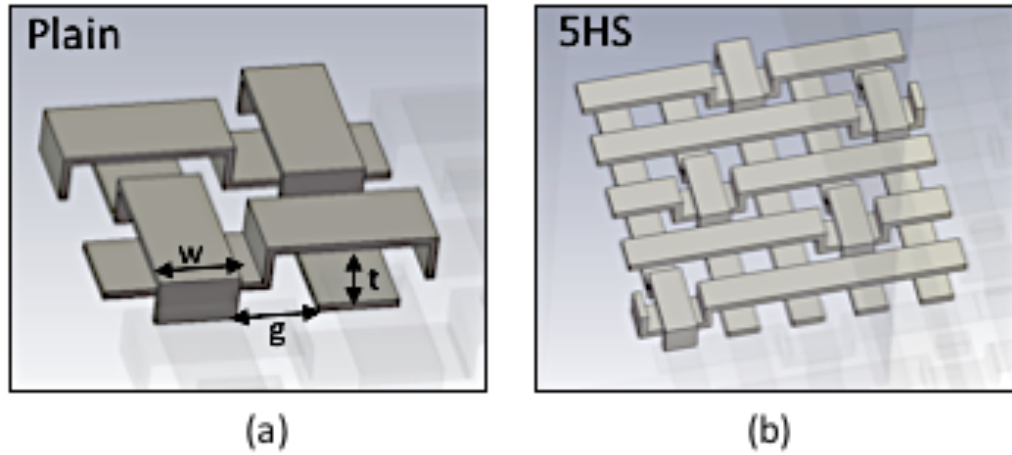


Figure 5.2 Unit Cell model of CFRP weave: (a) Plain and (b) 5 Harness-satin

Three simplified woven carbon composite models (i.e., grid, plain and 5 harness satin or 5HS) are utilised in the simulation with WR-42 open-ended rectangular waveguide (ORWG) measurement. Scattering parameters S_{11} as microwave responses are obtained from each parametric study. Due to the fact that carbon fibre is a highly conductive material, the microwave responses are assumed to be solely from the carbon bundles represented by perfect conductors in free space ($\epsilon_r=1$).

Figure 5.2 shows unit cells of woven CFRP models with plain weave and 5HS weaving structures, respectively. Assumingly, the thickness of fibre bundles is defined as 0.1 mm in all simulation models. The CFRP structural parameters studied in the simulations are width w , the gap between bundles g , ply thickness t and number of laminate layers (plies) n .

5.1.1 Grid Model ($t=0$)

In this simulation, we only investigate the effect of parameters w and g in the $x - y$ plane, which define the size of planar gap between fibres. The grid models with different w and g values: $\{w=0.5, g=1; w=1, g=1; w=1, g=0.5\}$ and $t=0$ are simulated. Figure 5.3 shows the microwave responses obtained from computer simulation. All three responses demonstrate a single-band resonant response, which are in line with the LC equivalent circuit theory of inductive grid structure [129]. When the gap between fibres is decreased, the capacitance of the CFRP structure will increase, and thus lower the resonant frequency ($f_c = 1/2\pi\sqrt{LC}$).

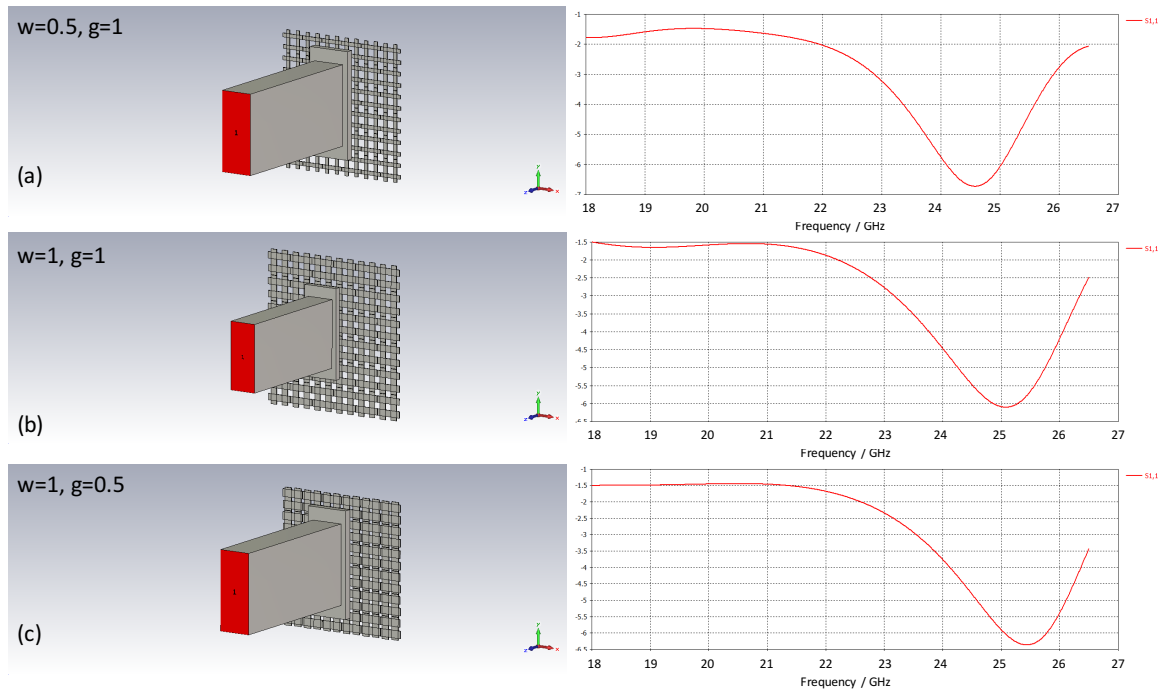


Figure 5.3 Responses of grid models (a) $w=0.5\text{mm}$, $g=1\text{mm}$, (b) $w=1\text{mm}$, $g=1\text{mm}$, (c) $w=1\text{mm}$, $g=0.5\text{mm}$

5.1.2 Plain and 5HS models

In this simulation, we investigate the effect of ply thickness t in plain and 5HS woven CFRP composites relating to the gap between overlapping fibres within a ply. Both models are simulated with $t = \{0, 0.25 \text{ and } 0.5\text{mm}\}$, $w = 1 \text{ mm}$ and $g = 1 \text{ mm}$. Figure 5.4 shows the 3D plain weave models and S_{11} responses obtained from CST simulation. At $t = 0$, the microwave response shows single-band behaviour like that of the grid structure. Increasing of t causes decreasing of resonant frequency as well as introduces multiple resonant/ripple responses. It is due to the increasing of the gap between overlapped fibres, which is equivalent to the interfacial capacitance of weft and warp fibres. Moreover, the wavy structure of weft and warp fibres also emphasise such high order responses as demonstrated in form of multiple resonances/ripples. The simulation models and S_{11} responses of 5HS weave models are shown in Figure 5.5. Like that of the grid and plain weave, the microwave response of 5HS weave at $t=0$ show a single-band resonance. Also, the resonant frequency is increased due to an increasing of t , like the plain weave structure. We also found that both woven structures generate microwave responses differently. It is suggested that the understanding of this phenomena will lead us finding such ‘EM signatures’ of woven CFRP textures.

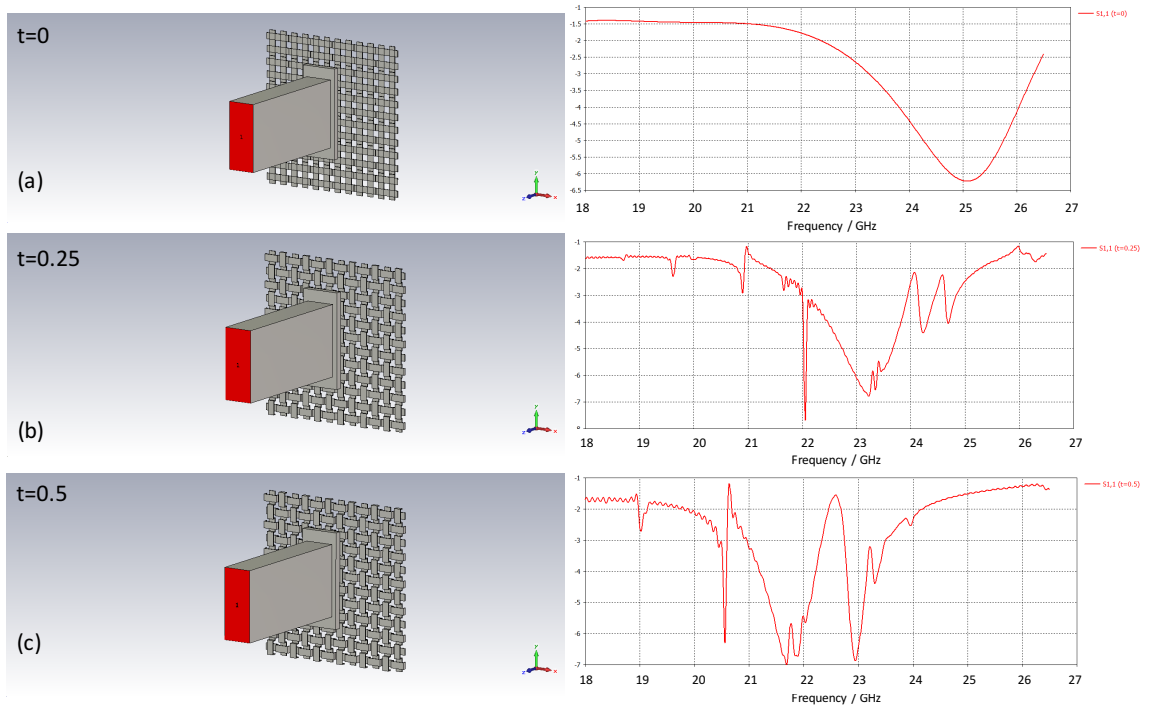


Figure 5.4 Responses of Plain weave models: (a) $t=0\text{mm}$ (b) $t=0.25\text{mm}$, (c) $t=0.5\text{mm}$

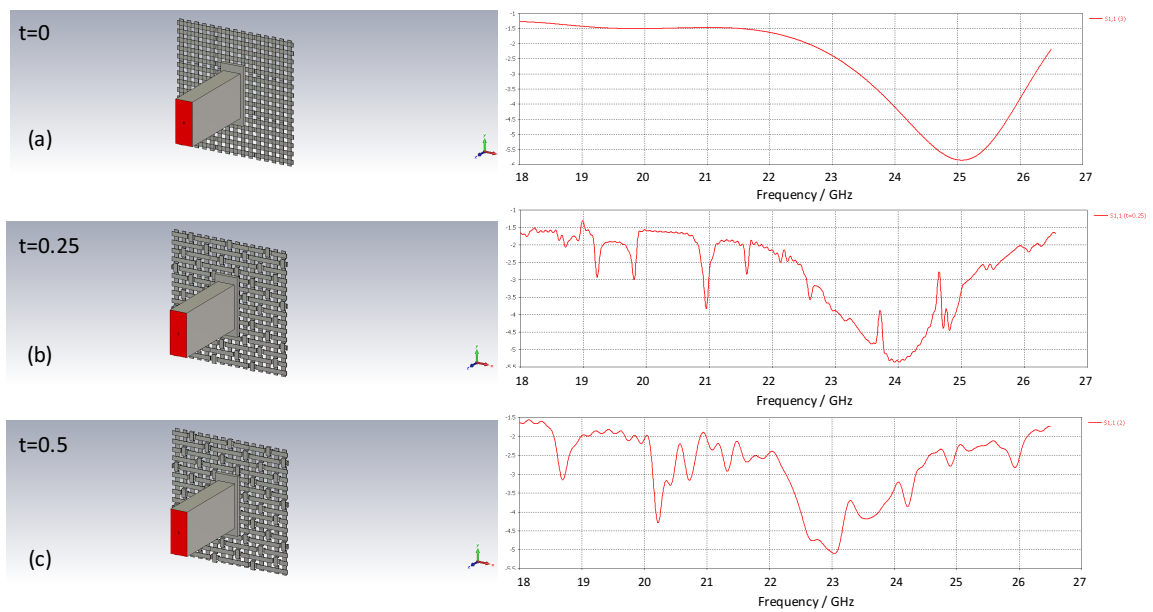


Figure 5.5 Responses of 5HS weave models: (a) $t=0\text{mm}$ (b) $t=0.25\text{mm}$, (c) $t=0.5\text{mm}$

5.1.3 5HS with Multi-ply model

In this simulation, we investigate the influence of a number of woven plies of 5-harness statin woven CFRP. The 5HS weave models with a number of plies of $n = \{1, 2 \text{ and } 3\}$, $w=1\text{mm}$,

$g=1\text{mm}$ and $t=0.4\text{mm}$ are simulated. Figure 5.6 shows the multi-ply 5HS woven composite models and their responses. There is no significant change of the main resonant lobe, however, increasing the number of ply layers causes an increasing number of resonances/ripples. Similarly, the multi-band FSS structure where a number of layer equivalent to the amount of cascading equivalent circuit which increase the order of the responses.

5.1.4 Discussion on Simulation Results

The EM responses of woven CFRP models with plain and 5HS structures and their structural parameters are investigated through simulation studies. It is found that the increase of gap and ply thickness will lower the resonant frequency. The textile structures of woven CFRP and number of laminate layer strongly affect the EM responses on which CFRP with more wavy texture or number of layers tend to generate higher resonant/ripple responses (see Figure 5.7 and Figure 5.8). In the next section, an experimental study of impact damage on woven CFRP will be undertaken and compared with the simulation study.

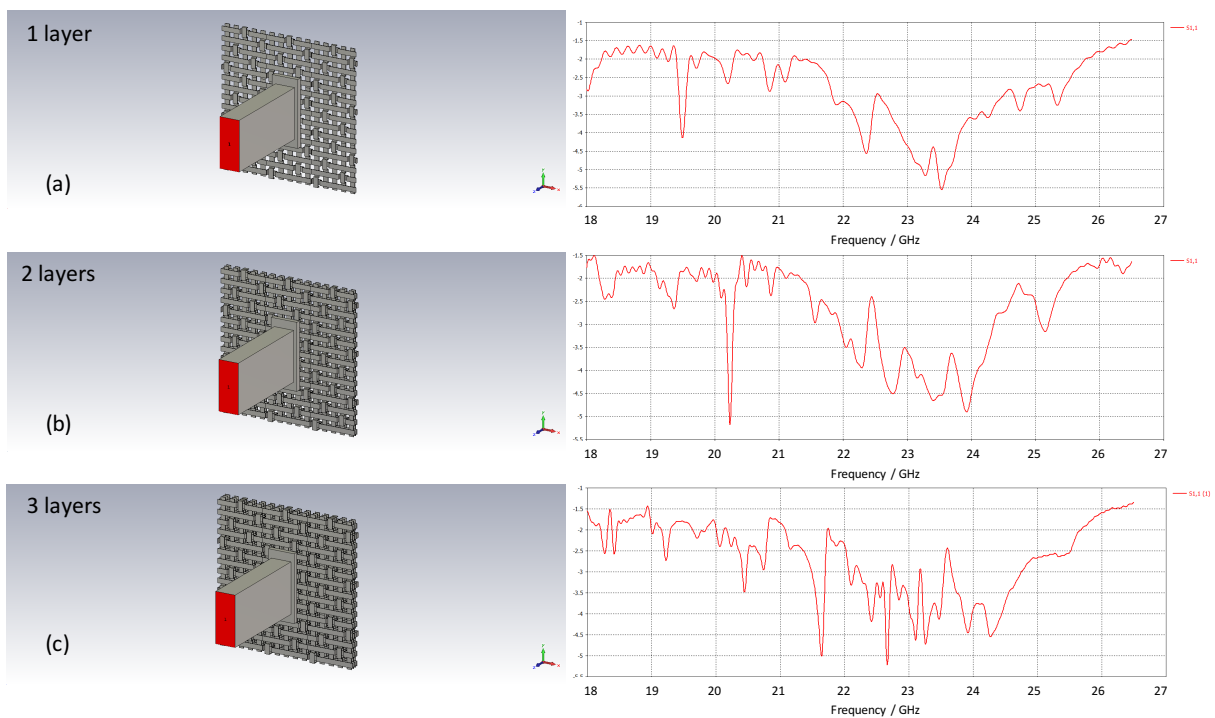


Figure 5.6 Multi-ply 5HS weave model and their response: (a) $n=1$ (b) $n=2$, (c) $n=3$

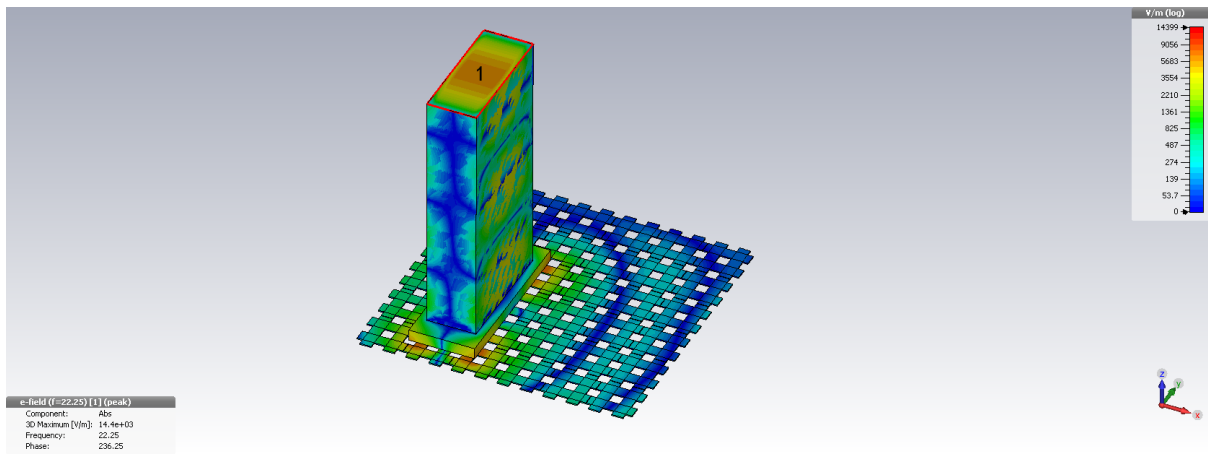


Figure 5.7 E-field distribution on the CFRP with a grid model

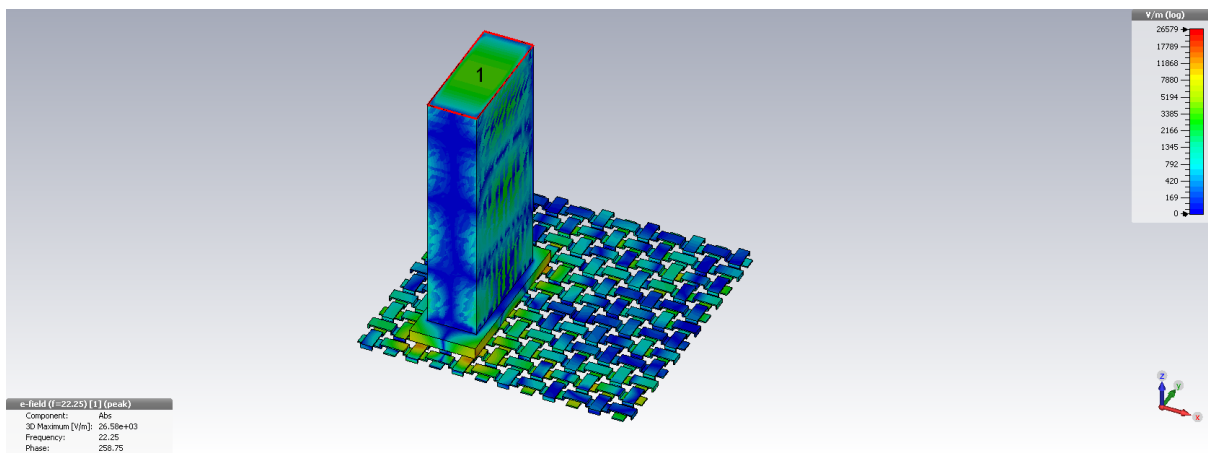


Figure 5.8 E-field distribution on the CFRP with a plain weave model

5.2 Experimental Studies

This study investigates the impact damage and fibre texture on 5HS woven CFRP composite using an open-ended waveguide probe operating in K-band (18-26.5 GHz). The images of impact damage are obtained by scanning (C-scan) over three different energy impact samples. Based on inhomogeneity and layered characteristic of CFRP, texture and depth information are studied as well.

5.2.1 Woven CFRP with Impact Damage Samples

Referred to Section 3.2.2, the CFRP sample plate is composed of 12 layers of 5 harness satin carbon fibre woven with balanced woven fabric [218]. The polymer matrix is made of Polyphenylene sulphide (PPS), a chemical and thermal resistive thermoplastic resin system produced by TenCate Advance Composites, Netherlands. The electrical conductivity of CFRP is around 10 S/m – 100 S/m in the transverse direction and 5,000 S/m and 50,000 S/m in the longitudinal direction. The CFRP plates were cut into dimensions of 100 x 130 mm² with the average thickness is 3.78 mm. To produce a sample, we use a drop-weight impact test apparatus according to ASTM D7136 standard with a hemispherical bumper head having a diameter of

20 mm and weight of 2.045 kg. The samples are categorised by the impact energy. The amount and type of defects might be different depending on the impact energy. The common defect types include surface dent, matrix crack and fibre breakage [204].

5.2.2 Measurement Setup

The experimental environment setup is presented in Figure 5.10. We use an X-Y scanner to hold and deploy the waveguide probe over the sample with constant lift-off at 0.1mm. A vector network analyser (Agilent PNA E8363B) measures reflection coefficient (S_{11}) through a coaxial cable connected to the probe via SMC connectors. A computer program written in MATLAB® together with Scanner Controller and GPIB interface card are used to control and synchronise probe location and S_{11} measurement. Prior to the measurement, we calibrate the VNA together with the coaxial cable using a calibration kit (open, short and loaded). The calibration results are used to automatically compensate the cable characteristic and channel delay (due to the cable length) of the measurement results. According to parameters in Table 5.1, the VNA transmits signals in a sweeping manner, and capture wideband reflection coefficients from the same port (P1). The VNA obtains S_{11} from the waveguide probe at different locations, in an area of $30 \times 30 \text{ mm}^2$ in X and Y directions.

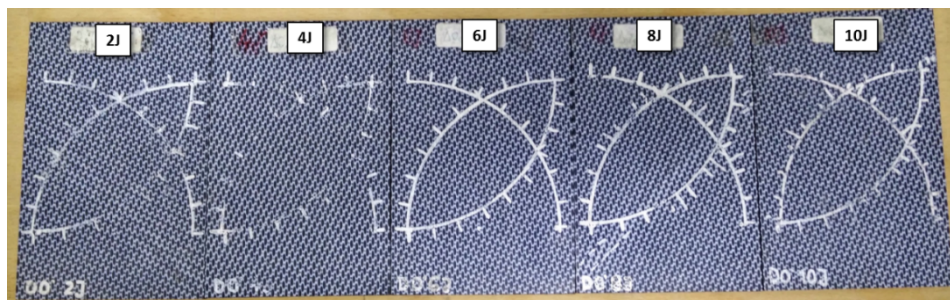


Figure 5.9 Woven CFRP with impact damage ranging from 2J to 10J

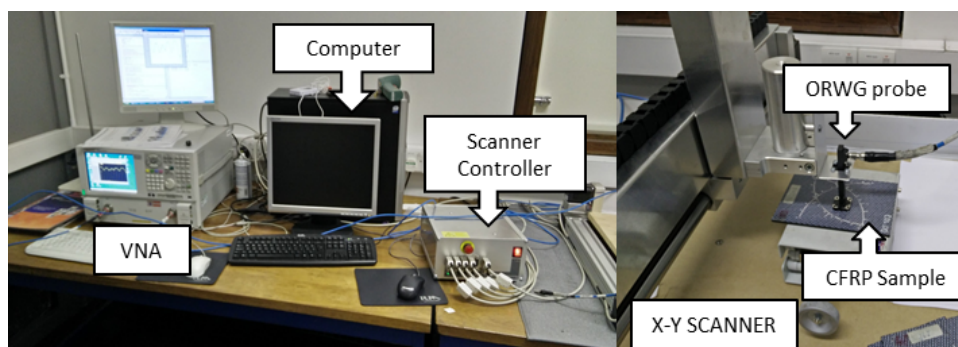


Figure 5.10 Measurement setup for CFRP inspection

Table 5.1 Measurement parameters of CFRP impact damage detection and texture inspection

Parameter	Value
Sweeping frequency range	18-26.5 GHz (K-band)
Number of points in linear swept	1601 ($\Delta f=3.5$ MHz)
Waveguide inner dimension (a × b)	10.668 mm x 4.318 mm
Impact damage	2J, 4J, 6J, 8J and 10J
Scanning step size	a/2, a/4, a/10 and a/20
Delay time between sample	1 second

5.2.3 Experiment results

In this section, responses of texture and impact area, optimisation of scanning step size, and data analysis using PCA are discussed.

5.2.3.1 Spectral Responses of woven CFRP with impact and non-impact areas

In order to estimate the effect of impact on the structural parameter of woven CFRP composite, the spectral response of impact and non-impact areas are compared. The 6J sample is investigated in this experiment with the smallest scanning step size of 0.5 mm ($a/20$). Figure 5.11(a) shows the reconstructed image of 6J sample scanned using average magnitude feature. The scanning area cover non-damage (left) and impact damage (right). The image is reconstructed from the average magnitude feature described in section 3.3.3.2, [123] and [124]. We select areas of 5 x 5 mm² of both texture and damage areas (50 sampling positions each) to calculate the average microwave response of both areas. Figure 5.11 (b) and (c) show plots of minimum, maximum and average microwave responses of non-impact and impact area, respectively. It can be seen, in general, that the variation of microwave responses in the impact area is found to be higher than the area of non-impact damage. Moreover, the response of texture with impact damage area is somewhat shifted to the higher frequency as presented in Figure 5.11 (d). It could be suggested that the impact damage alters the internal structure of the CFRP. The shifting of microwave response in the damaged area implies decreasing of the capacitance value of the equivalent circuit, and thus the gap between fibres are narrowed. The suggestion is also in line with mechanical studies of impact damage on CFRP [219]–[221], where the damage causes structure compression and deformation of fibres/matrix that could narrow the gap between two interfacial conductive fibres/layers resulting in the capacitance lost [222].

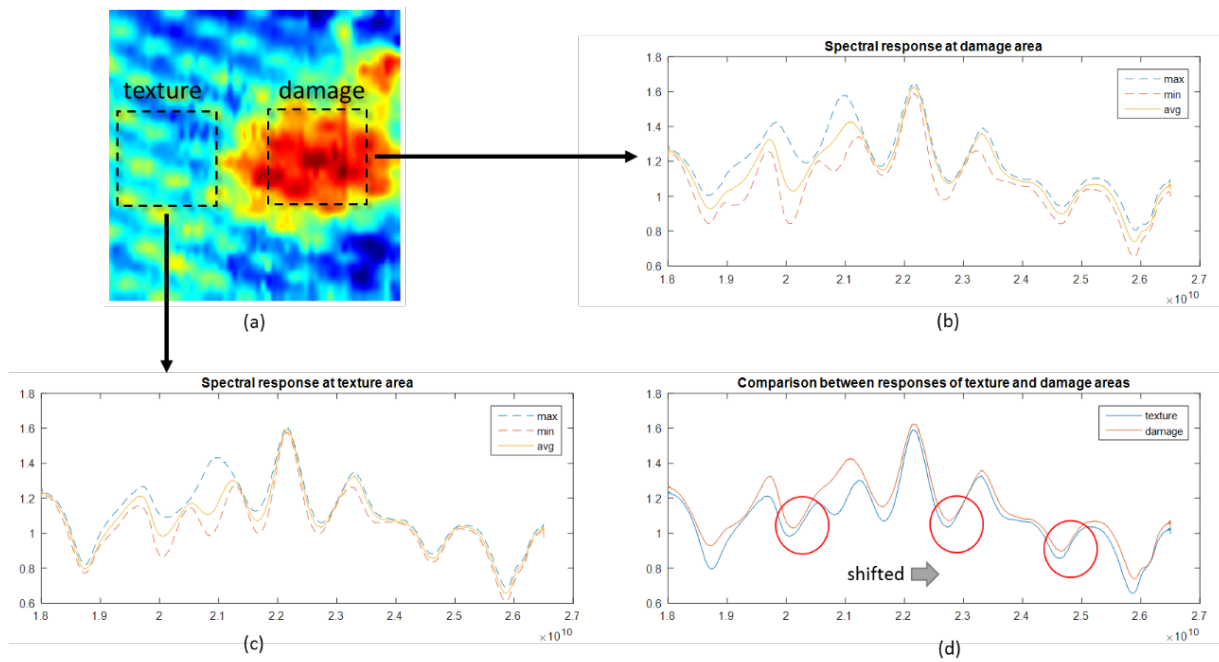
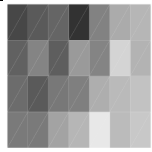
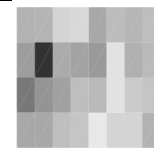
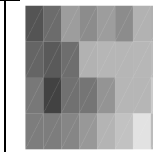
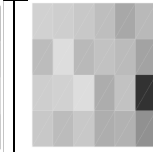
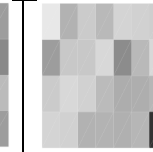
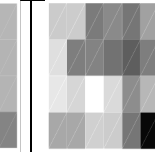
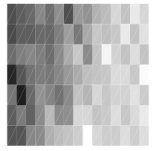
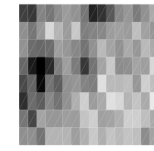
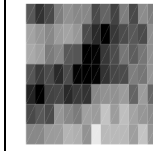
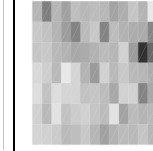
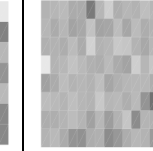
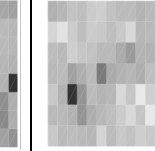
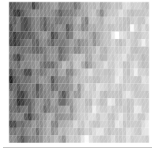
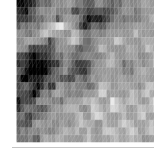
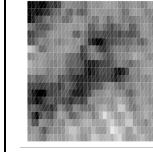
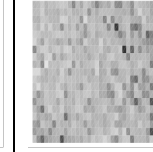
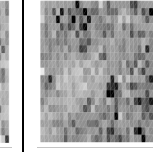
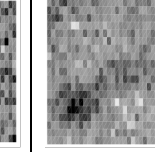
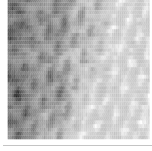
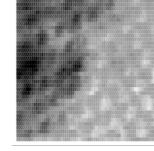
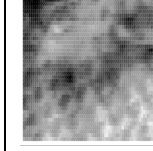
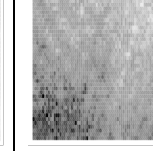
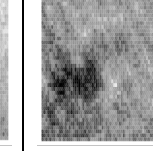
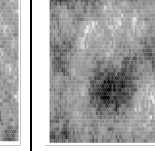


Figure 5.11 Microwave responses of 5HS CFRP sample with and without impact damage: (a) a reconstructed image of 6J sample, (b) response of non-impact, (c) response of impact damage, (d) average responses from non-impact and impact damage.

5.2.3.2 Optimal Scanning Step Size

Scanning step size is an essential parameter for C-scan as a trade-off between scanning time and spatial resolution. In this section, the optimal scanning step size for detection of impact damage and woven texture are investigated with 4J, 6J and 10J samples. The images of the defect and fibre texture obtained from three different energy impact samples with various Δx and Δy scanning step sizes at 19 GHz and 26.5 GHz are presented in Table 5.2. The images reconstructed at both frequencies display different defect and texture as complex responses from simulation study in section 5.1.3. It is noted that the impact damage of the 4J sample is not clearly revealed by the simple imaging technique. Comparing the images of different step sizes in both tables, it is found that defects are revealed in the scanning step size of $a/4$ and below. Considering the defect areas (shadow), we have found that the area of the defect is significantly larger than the impact area. It could be suggested that the impact does not only harm the surface but also causes internal defects (e.g., delamination) within the material. To inspect the fibre texture, the step size of $a/10$ and smaller are recommended as they are clearly revealed in the images.

Table 5.2 The images of woven CFRPs with impact damage 4J – 10J at scanning step size ranging from $a/2$ to $a/20$.

	19 GHz			26.5 GHz		
	4J	6J	10J	4J	6J	10J
$\Delta y = a/2$						
$\Delta y = a/4$						
$\Delta y = a/10$						
$\Delta y = a/20$						

5.2.3.3 2-D SAR Imaging of Woven CFRP

Microwave NDT&T using raster scan (C-scan) technique requires a specific gap between the waveguide probe and the sample, therefore without SAR correction, the reconstructed image from the probe spatial responses may be out of focus. SAR imaging uses the relative position between the probe/antenna and the sample to reveal the spatial distribution with focusing of the targets. Figure 5.12 presents the reconstructed images of woven CFRP with 6J impact damage with and without 2-D SAR correction. The 2-D SAR technique is described in 3.3.4.1.

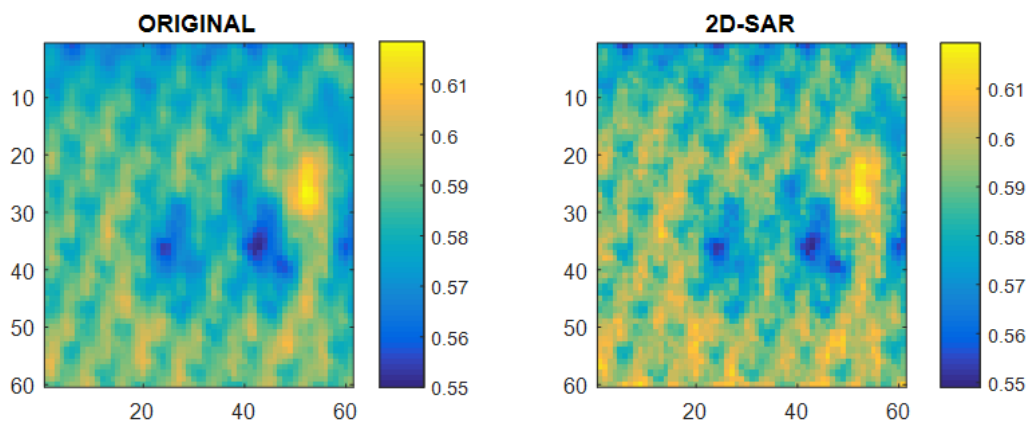


Figure 5.12 Reconstructed images of 6 J impact damage sample using average magnitude feature: (left) original (right) with 2-D SAR correction.

5.3 Feature Extraction of Impact Damage

5.3.1 Framework for Feature Extraction of Impact damage

The proposed feature extraction framework is shown in Figure 5.13. There are two major steps to extract the impact damage, the offline PC modelling and the feature extraction. In the offline PC modelling, firstly, the data obtained by the scanning system is re-focused based on the lift-off parameter using 2D SAR techniques. Next, due to undulated fade-in and fade-out of texture along the increasing of frequency, we reduce the redundancy by selecting only the responses at frequencies given local maxima and minima of the different response between the impact and non-impact areas. It is noted that the frequency selection process does reduce not only the redundancy and complexity of the feature analysis in offline training but also the number of sampling frequency in real-time measurement. Then, the responses at selected frequencies are analysed for principal components based on PCA method. The obtained principal component coefficients are tested by projected with the training data resulting in feature images of different PCs. Finally, the image representing the highest contrast between impact and non-impact areas is chosen as the PC based model for feature extraction of the impact damage.

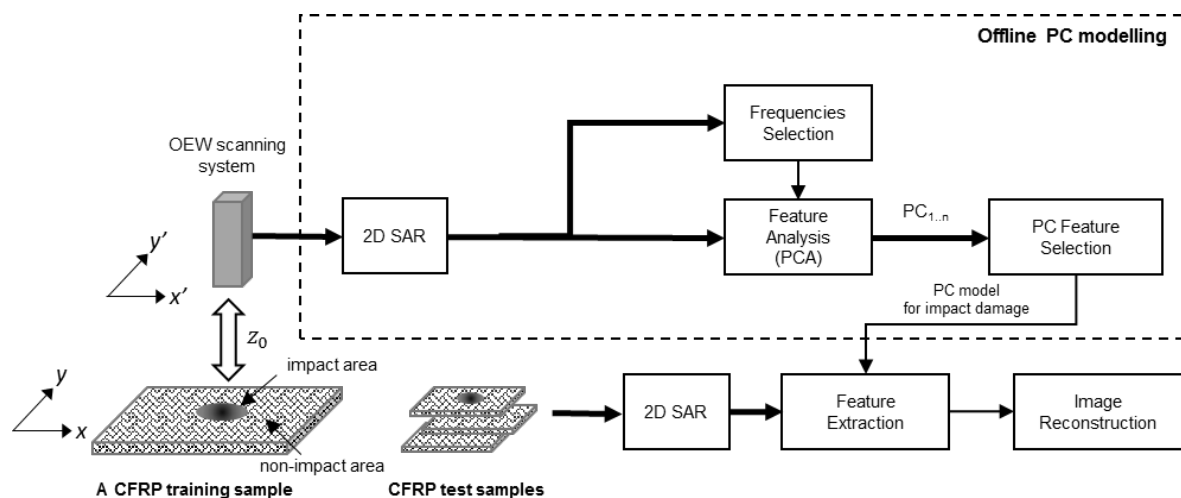


Figure 5.13 the framework for PC based feature extraction of impact damage.

The feature extraction in the measurement process can be in offline or online. The sampling data in the offline process are usually in the form of uniform sampling of the full area with a certain scanning step size, whilst the online data are usually in the form of uniform or non-uniform sparse samples. Similar to the off-line training, the obtained sampling data is firstly re-focussed by 2D SAR process. The focused data are then projected to the PC based model resulting in the impact damage image. In case of non-uniform samples, the non-uniform fast Fourier transform (NUFFT) is used to improve the performance of the 2D SAR process together with the natural interpolation to reconstruct the full detail image in the image reconstruction process.

5.3.2 Frequency Selection and PCA feature

The sampling responses from 6J sample are selected as a training dataset and analysed using PCA. Based on the wideband configuration of the open-ended waveguide scanning system, the sampling data contains a set of frequency spectra with corresponding x and y position as presented in Figure 3.17. Based on multiple resonances/ripples responses shown in Figure 5.11, only magnitude at significant frequencies: $f_1=18.62$ GHz, $f_2=20.03$ GHz, $f_3=21.48$ GHz, $f_4=22.70$ GHz, $f_5=23.40$ GHz, $f_6=24.77$ GHz, $f_7=25.44$ GHz, $f_8=26.01$ GHz, are selected for PCA analysis. A set of principal components are obtained by the PCA process described in Section 3.3.3.4. Following the projection of principal component to the sampling data, the reconstructed images of the first six principal component (PC1-PC6) are displayed as in Figure 5.14. The corresponding percentage of variances of each PC are shown in Table 5.3. It can be seen from the PC1 image that it is nearly identical to the image reconstructed from the average magnitude feature shown in Figure 5.12. The image contains both impact damage and strong woven texture. Image of PC6, on the other hand, clearly shows impact damage with little effects of texture. Therefore, the PC6 is selected to be used for feature extraction of impact damage.

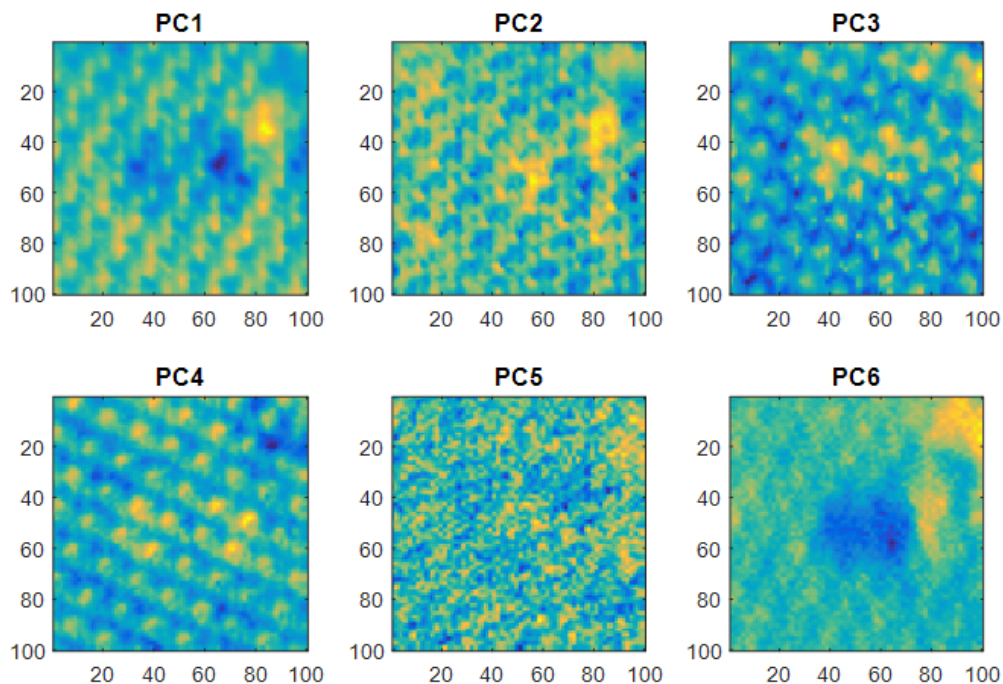


Figure 5.14 Reconstructed images based on features extracted from PC1-PC6

Table 5.3 Principal Components PC1-PC6 from spectral responses over the scanning area

PC	PC1	PC2	PC3	PC4	PC5	PC6
Percentage of variance	44.66	23.03	16.46	9.59	3.14	1.67
Commutative Percentage of variance	44.66	67.69	84.15	93.74	96.88	98.55

5.4 Quantitative Evaluation of Impact Damage on Woven CFRP

To evaluate the capability of the system for characterising impact damage at different impact energies, the PC6 is projected to the test samples of woven CFRP composite with impact damage ranging from 2J to 10 J. The reconstructed images of the impact samples based on the PC6 feature are shown in Figure 5.15. The impact damage can be clearly seen in the samples with the impact energy of 4J and above, while there is no evidence on the 2J sample. Finally, the impact energies can be characterised by the area of the defect using an image segmentation method such as k-mean clustering [223] as demonstrated in Figure 5.16.

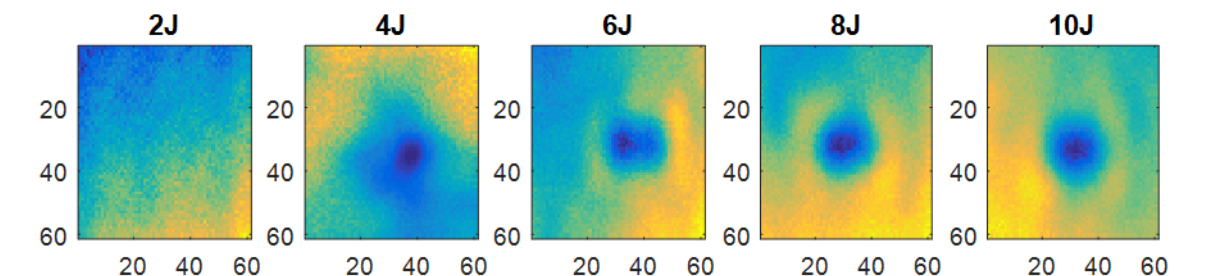


Figure 5.15 Images of impact damages of 2J to 10J samples presented by PC6 features.

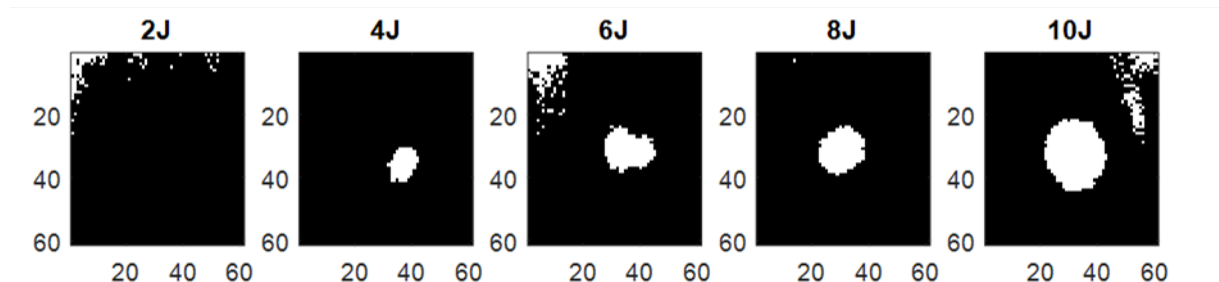


Figure 5.16 k-mean clustering of impact damage at 2J to 10J samples

5.5 Chapter Summary

In this chapter, a microwave (K-band) open-ended rectangular waveguide probe scanning system is used to scan woven CFRP samples with different impact damages ranging from 2J to 10J. The simulation studies of woven composites with different textures demonstrated the complex responses of the composite structures caused by fibre parameters (e.g., width, length, gap, etc.) and a number of stratified layers. Measurement parameters such as scanning step size and probe lift-off are investigated for optimal values for impact damage and woven texture imaging. It is found that the constant lift-off at 0.1mm, the scanning step size of $a/8$ is sufficient for detection of impact damage, while imaging of fibre texture needs a step size of $a/10$ and below. Moreover, 2-D SAR algorithm improves time image focus by phase distortion correction as a function of probe lift-off.

Finally, the wideband reflection coefficients are obtained over the samples and analysed for the impact damage feature with separation of texture influences. The PCA is applied to the training sample (6J) to extract the significant principal components. Based on projection results, the PC6 is selected for the feature extraction of impact damage on woven CFRP composites. The impact energies at the CFRP can be characterised by the impact area based on k-mean clustering method.

Chapter 6 Detection and Evaluation of Flat Bottom Hole Defects on Coated GFRP Pipe

To overcome the challenge of pipe curvature, we propose to use principal component analysis and synthetic aperture radar - tomography for microwave inspection of flat bottom holes in GFRP pipes. In the previous two chapters, PCA has been utilised to characterise steel corrosion stages of coated steel sample and extract impact damage feature from the woven composite texture. The results showed that PCA could successfully characterise steel corrosion stages and impact damage on CFRP by mitigating the dominant effect of the coating layer of coated steel plate and variation of weaving texture in CFRP along with others (e.g., surface roughness and inclination). Although PCA may reveal the FBH defects in GFRPs, the PC feature values are the results of extensive dimension reduction, and thus it loses crucial information (i.e., frequency spectrum or time sequence) to determine the defect depths. SAR-tomography will be utilised as a complementary method to verify the location of FHB found by PC feature and facilitate evaluation of defect depth. SAR-tomography or tomographic SAR is an imaging technique allows reconstructing reflectivity profiles in the elevation (depth) by using several responses acquired with different probe positions. However, the major challenge of SAR-tomography is the requirement of high computation power. Therefore, for the sake of real-time capability for FBH characterisation (regardless of 3-D reconstruction), in this work, we initially apply PCA to gain the region of interest and then only use SAR-tomography within a limited area to verify defect location and facilitate estimation of the defect depth.

6.1 GFRP Pipe Composite Model

Figure 6.1 shows an open-ended rectangular waveguide probe obtaining reflection coefficient Γ (or scattering parameter S_{11}) over a GFRP Pipe sample with FBH defect. We configured the rectangular probe to operate in the dominant TE_{10} mode, frequency range of K-band (18 - 26.5 GHz). Assumably, the probe transmits and receives electromagnetic waves of the same dominant TE_{10} mode. Although it is known that the higher modes can be produced by an interrogation with the sample, it usually affects the result for only less than 3% [63] and will be discarded by further signal processing and data analysis.

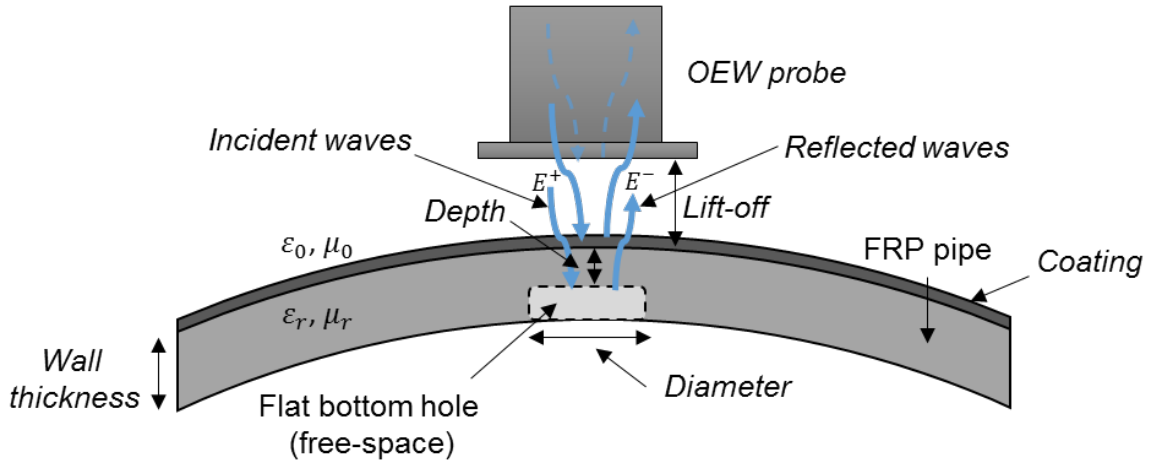


Figure 6.1 Microwave Open-ended Waveguide for GFRP pipe scanning

The reflection coefficient can be written in terms of reflected wave E^- over incident wave E^+ ($\Gamma = E^-/E^+$) or impedance matching between probe and layers of material under test as follows.

$$\Gamma = \frac{Z_{in} - Z_{WG}}{Z_{in} + Z_{WG}} \quad (6.1)$$

$$Z_{in} = \eta_i \frac{Z_{i-1} + \eta_i \tanh(\gamma_i d_i)}{\eta_i + Z_{i-1} \tanh(\gamma_i d_i)} \quad (6.2)$$

$$\eta_i = \eta_0 \sqrt{\mu_{ri}/\epsilon_{ri}} \quad (6.3)$$

$$\gamma_i = j(2\pi f/c) \sqrt{\mu_{ri}/\epsilon_{ri}} \quad (6.4)$$

where Z_{in} is the intrinsic impedance of the first incident layer (free-space), Z_{WG} is the intrinsic impedance of the waveguide termination, i is layer number, d_i is thickness, η_i and γ_i are complex intrinsic impedance and propagation constant, ϵ_{ri} and μ_{ri} are complex permittivity and complex permeability. It can be seen from equation (6.1), (6.2) and the GFRP model in Figure 6.1 that the complexity of reflection coefficient is increasing by a number of material layers, upon which the reflected waves are generated in each layer interfaces.

6.2 FRP Pipe Samples

In experiments, we investigate a dedicated GFRP sample with four FBH defects (H1-H4) with different depths. The GFRP sample is an arch portion size of 130 x100 mm of a GFRP pipe with a diameter of 130 mm. The FBHs are machined on the inner surface of the GFRP sample as shown in Figure 6.2. The GFRP sample is composed of 14 layers fibreglass composites with a thermal barrier coating, has a total thickness of 13 mm. The specifications of the FBH defects and GFRP sample are summarised in Table 6.1.

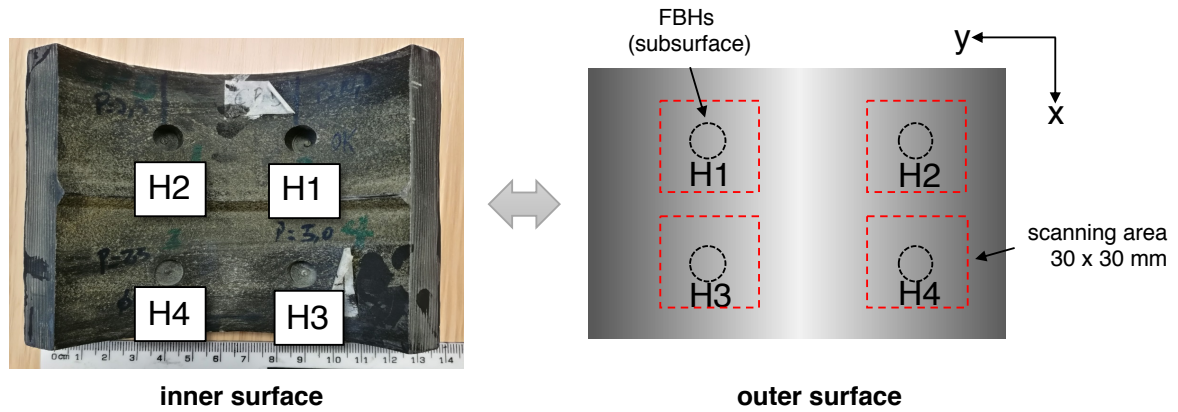


Figure 6.2 The GFRP pipe sample with 4 FBHs

Table 6.1 GFRP pipe sample parameters and values

Parameter	Value
Wall thickness	13 mm
Number of GFRP layers	14 (approx. thickness of 0.9 mm per layer)
Defects	4 FBHs (H1-H4) at the inner surface
FBH diameter	10 mm for all FBHs
FBH depth from outer surface	H1 = 4.0 mm H2 = 5.5 mm H3 = 8 mm H4 = 11.5 mm

6.3 Experiment Setup for FRP Pipe Inspection using Open-ended Waveguide Probe

The equipment setup and experiment scenario of microwave OEW scanning system are illustrated in Figure 6.3 and Figure 6.4, respectively. The OEW probe was performing C-scan over the defect areas by means of an X-Y scanner (CNC Step High-Z S720T). In each x-y position, the vector network analyser (Agilent PNA E8363B) captured a wideband reflection coefficient and sent it to store in PC. Once C-scan is completed, the storage data will be processed by PCA and SAR tomography algorithms implemented in MATLAB. The detailed specifications of measurement parameters are listed in Table 6.2.

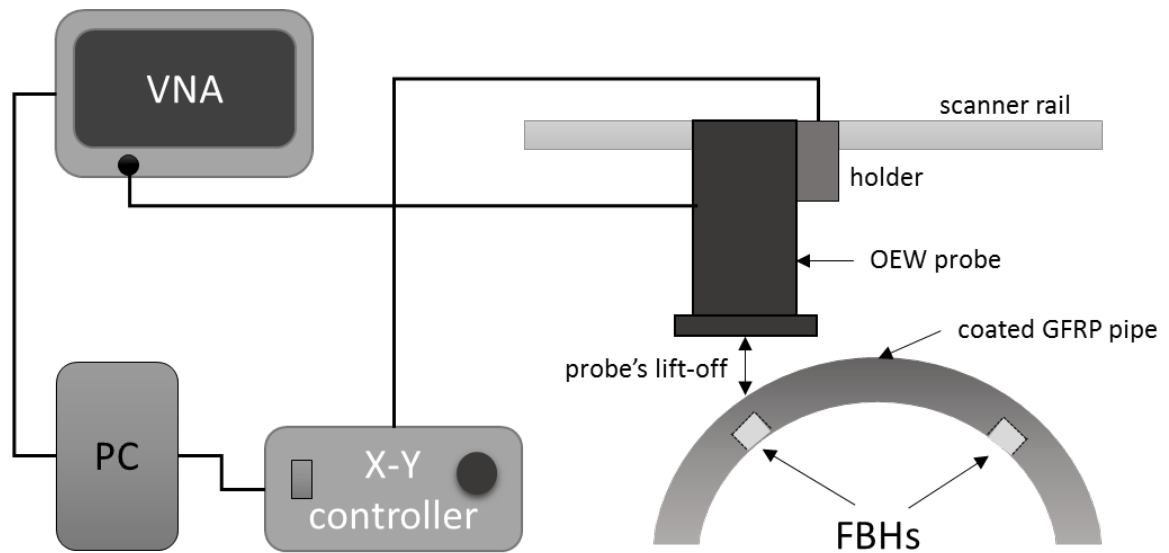


Figure 6.3 Equipment setup for OEW scanning system of GFRP pipe

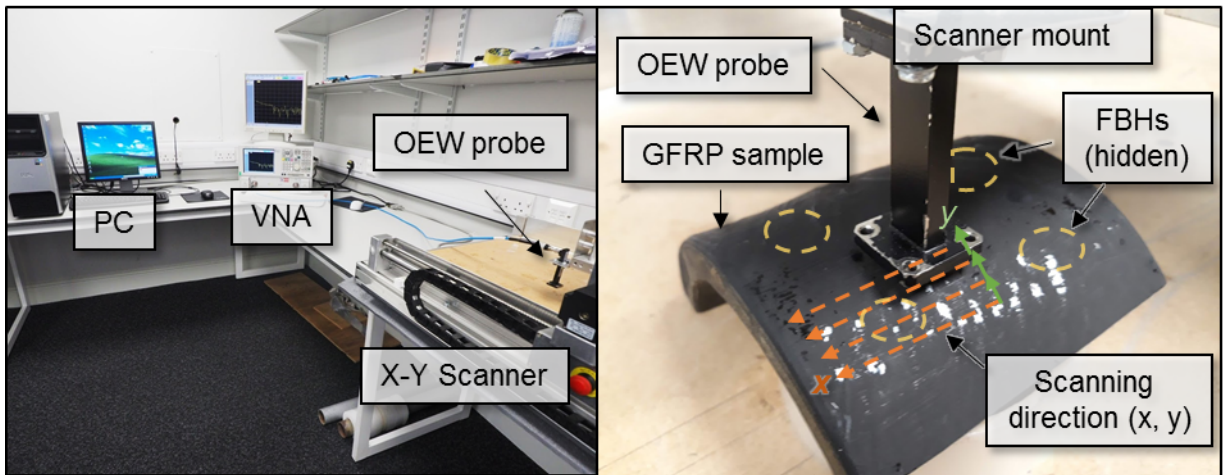


Figure 6.4 Measurement setup for scanning GFRP pipe sample

Table 6.2 OEW Measurement Parameters and values

Measurement Parameter	Value
OEW Probe dimensions	WR-90 (10.668 x 4.318 mm)
Scanning area	30 x 30 mm (raster scan)
Frequency range	18.0 -26.5 GHz (K-band)
Bandwidth	7.5 GHz
Number of the sampling frequency	201 ($\Delta f = 37.5$ MHz)
Lift-off (from the highest point of sample)	$z = 1$ mm
Scanning step sizes	$\Delta x = \Delta y = 1$ mm
Delay time between sample	1 second

6.4 Experiment Result and Validation

6.4.1 Magnitude and Phase Features Images

Prior to PCA and SAR tomography processing, the sampling data were investigated by two primary features: average magnitude (AM) and average phase (AP). Shown in the first two columns of Figure 6.5, it is evident in the results that both features cannot correctly reveal the defect area of FBHs. It is due to the dominant effect of lift-off variation along the pipe circumference as evidenced by a gradient area (from dark blue to bright yellow) along the y-axis.

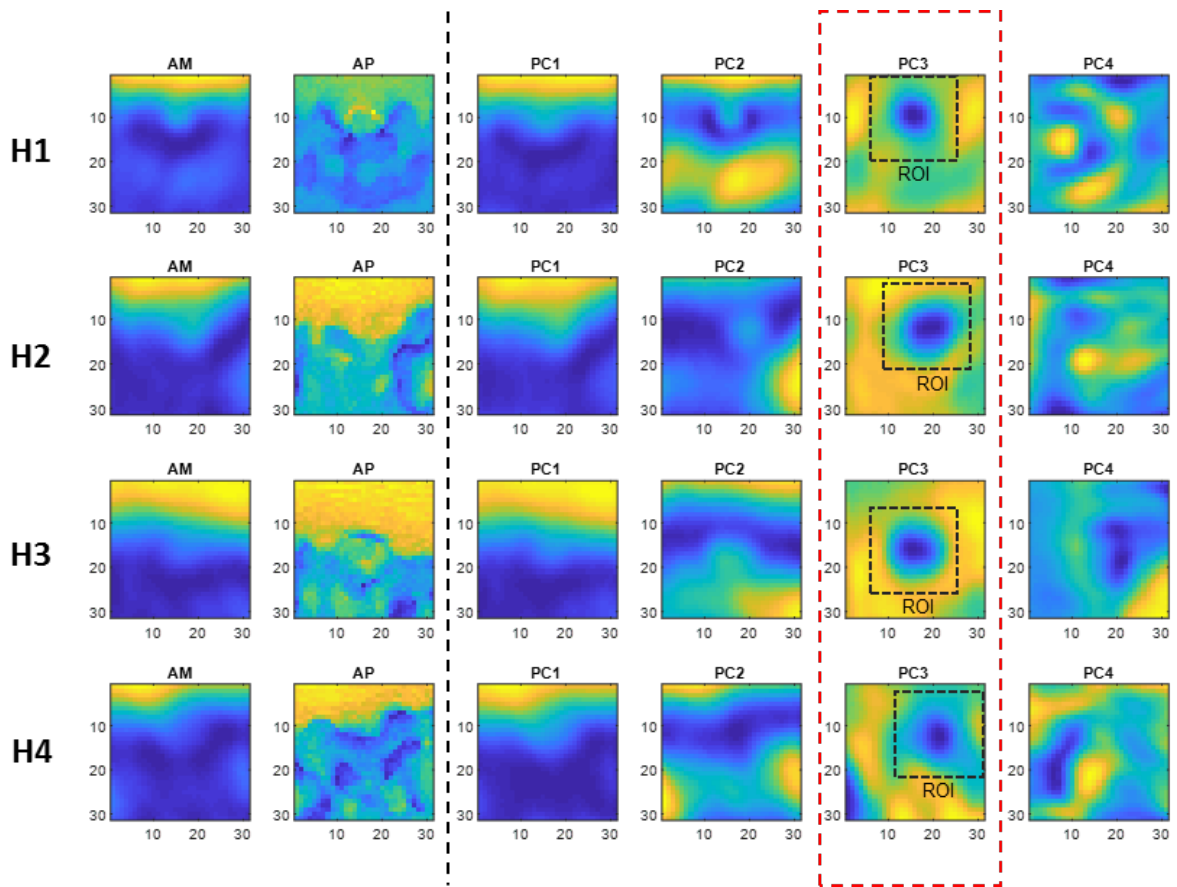


Figure 6.5 Images of FBHs reconstructed by features: average magnitude (AM), average phase (AP), and principal components (PC1-PC4) with ROI.

6.4.2 PC Feature Images

From PCA processing mentioned in Section 3.3.3.4, the reconstructed images of FBHs from first four PC features (PC1-PC4) are shown on the right section of Figure 6.5. Similar to AM and AP features, the images of the first two principal components (PC1 and PC2) characterise the effect of lift-off variation between probe and sample. By contrast, as the PC1 and PC2 are mitigated, PC3 feature clearly reveals the defect area of FBHs. The PC4 feature images, however, do not show any relation with the FBHs or the sample structure. It can be concluded that the effects of lift-off are only associated with the PC1 and PC2. According to the known

size of FBH (10 mm), ROIs with a perimeter of 20 x 20 mm, of PC3 images are extracted and positioned at the centre of the FBH.

Although PC3 feature could reveal the FHB defects, the major drawback of PCA (and other statistics-based methods) is the results strongly depend on the training dataset and their variance. There is no guarantee that the PC3 will always represent the FBH features. For instance, if we scan the FBH under a flat GFRP sample, it is likely that the FBH feature will present in lower PC orders (i.e., PC1 or PC2). Therefore, one of the challenges of using PCA is to select the right PC that is associated to the anticipating feature. Assuming the results in the first row of Figure 6.5 are from a blind sample with unknown defect size and location, it is impossible to decide whether PC3 or PC4 to represent FBH as both images show potential feature (a circle on contrast background). Moreover, PC feature is a result of data dimensional reduction and thus opposing to further analysis (e.g., depth).

6.4.3 SAR Tomography

We apply the SAR tomography-imaging algorithm discussed in Section 3.3.4, to verify the FBH location found in the ROI of PC feature images. Compared to PCA, SAR tomography demands much higher processing power as the computation of 3-D data. SAR tomography required ~ 1.821 s, while PCA required only ~ 0.456 ms for calculating the same sampling area of 60 x 60 mm with 201 sampling frequencies using a PC with processor Intel Core i5-6500@3.20 GHz and RAM of 16 GB. The results of SAR tomography, nonetheless, retain timing information, which could be useful for FBH depth determination. Figure 6.6 shows the cross-section tomography in $x-t$ plane and time sequential images in $x-y$ planes of FHB defects at time sequence = 106, 107 and 108, which are time $t = 6.24, 6.28$ and 6.33 ns, from top to bottom respectively. From images in the $x-t$ planes, layer interfaces (e.g., GFRP pipe surface) are presented by consistent stretched lines along x -axis, while the shorter lines/dots represent the FBH defect around the centre. It can be observed in tomography of H1 and H2 that the FHBs occur at $t = 6.24$ ns, whereas the FHBs of H3 and H4 reveal at $t = 6.28$ ns. Noticeably, the FHBs found in tomography image at selected time t are verified with that of the PC3 feature images obtained in the previous process.

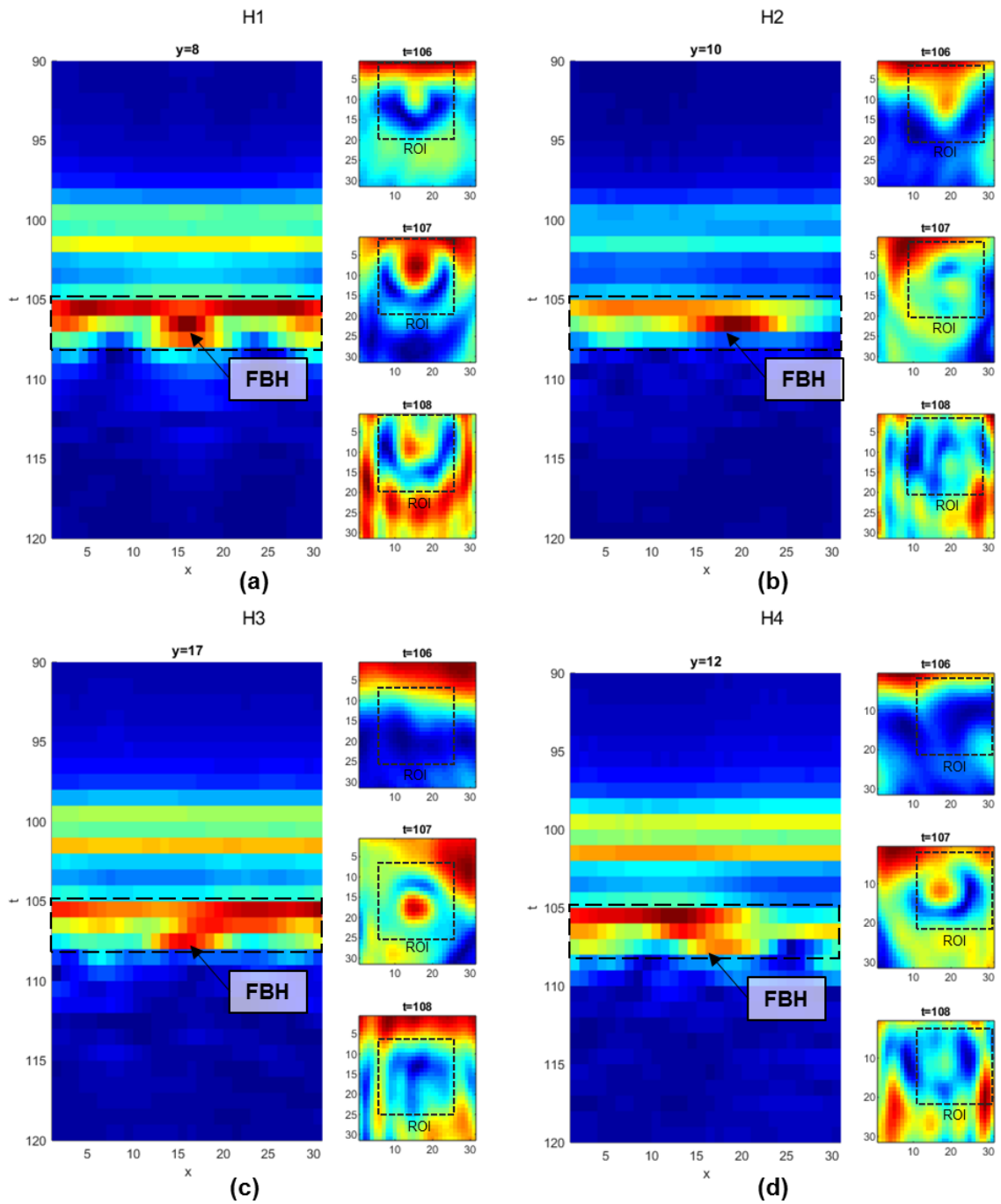


Figure 6.6 Tomography representing the location of FBHs: (a) H1, (b) H2, (c) H3 and (d) H4

6.5 Quantitative Evaluation of Flat Bottom Hold Defects

Following the detection process, FBHs are evaluated for estimation of location, size and depth. Figure 6.7 shows the evaluation process of FBH based on PC and tomography features. Location and diameter of FBH can be analysed by the PC3 feature and SAR tomography images, while the FBH depth requires further study for time-of-flight (or time delay) feature.

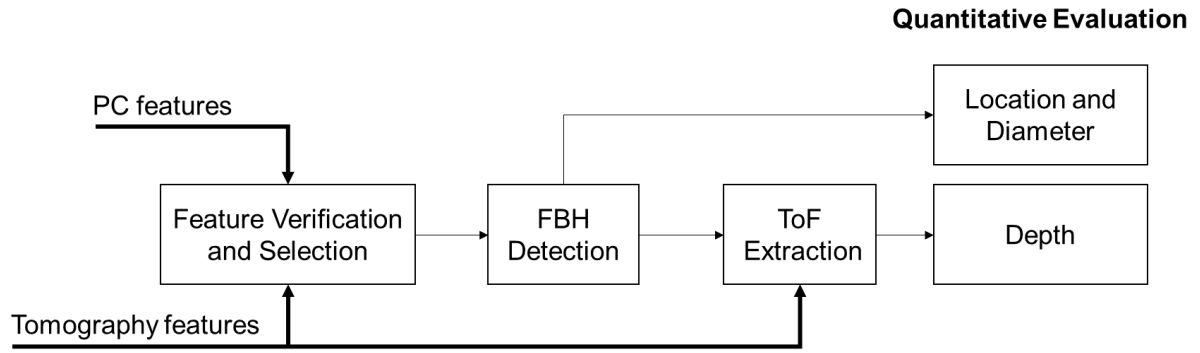


Figure 6.7 Process block diagram of FBH evaluation based on PC and tomography features

6.5.1 Quantitative Evaluation of Location and Size

Table 6.3 shows FBH locations calculated by PC3 and SAR tomography features, which are the point where the PC3 and SAR tomography images give their maximum value. In general, both defect shape and locations from PC3 and tomography features are found to be nearly identical except for the deepest FBH defect, H4.

To evaluate the diameter of FBHs, the PC3 and SAR tomography values are positioned and normalised according to ROI. The normalised values are in the range from 0 to 1 and thus the threshold of FBH area is set at half of the scale (0.5). Figure 6.8 shows the cross-section plots over the FBHs of centered and normalised PC3 and tomography features. As a whole, PC3 features show smoother curves across the FBH diameter, while the tomography features show steeper responses with overshoots around the edges of FBH area. Table 6.4 shows diameters and percentage error calculated by the distance between two projecting points at the threshold level of normalised features to the x-axis. It can be seen in the table that diameter values of PC3 feature increases by enhancing the FBH depth. It could be suggested that the layer of GFRP above the FBH contributes to the dispersion of the response and enlarge the FBH area of the PC3 feature. However, there is no trend for the diameter and error of the tomography feature. In addition, the percentage errors of tomography feature are significantly higher than that of the PC3 feature in most defects.

Table 6.3 Locations of FBH determined from PC3 and tomography

Feature	Location [x, y]			
	H1	H2	H3	H4
PCA (PC3)	[16, 9]	[19, 12]	[15, 16]	[21, 12]
SAR tomography	[16, 8]	[19, 10]	[15, 17]	[18, 12]
Diff. distance	1	2	1	3

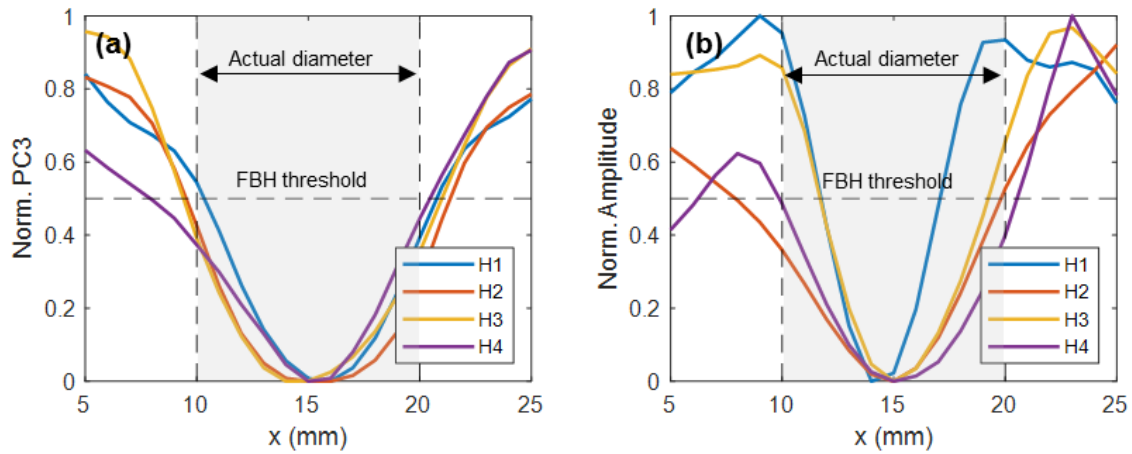


Figure 6.8 Cross section plot of FBHs by ROI centred and normalised of (a) PC3 feature and (b) SAR tomography feature

Table 6.4 FBH size of PC3 and tomography features

Feature	Diameter (actual value = 10 mm)							
	H1		H2		H3		H4	
	val.	%err	val.	%err	val.	%err	val.	%err
PC3	10.6	6	11.6	16	12.0	20	12.5	25
SAR Tomography	9.1	-9	12.0	20	6.4	-36	10.5	5

6.5.2 Quantitative Evaluation of Depth

To identify the defect location in time signal, the critical parameter to be considered is the range resolution, which is the minimum distance upon which two reflected signals can be distinguished. The range resolution of wideband response is calculated by

$$\Delta R = \frac{c}{2B} \quad (6.5)$$

where B is the signal bandwidth, c is the speed of electromagnetic waves. The speed of electromagnetic waves in free-space is around 3×10^8 m/s, whereas in GFRP (is around half of the free-space. Therefore, with the signal bandwidth of 7.5 GHz (18 GHz – 26.5 GHz), the range resolution in free-space and glass fibre are ~ 20 mm and 10 mm, respectively. According to the dimensions of the sample given in Table 6.1, the reflected signals from GFRP surface and the FBH location are hardly distinguishable. However, the solely reflected signal FBH can be revealed by the subtraction of the background and the FBH depth can be estimated by the relative time position of the reflected signal.

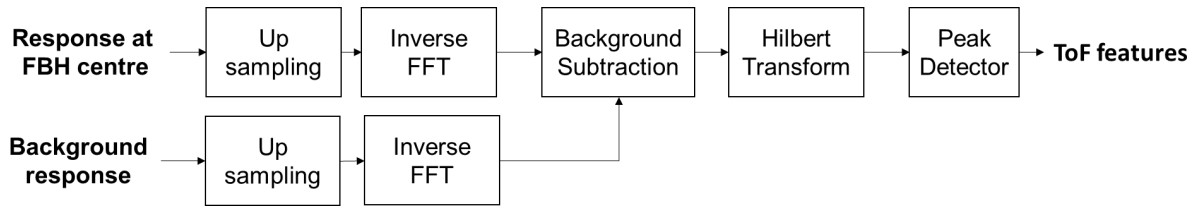


Figure 6.9 Process block diagram of ToF feature extraction from FBH response

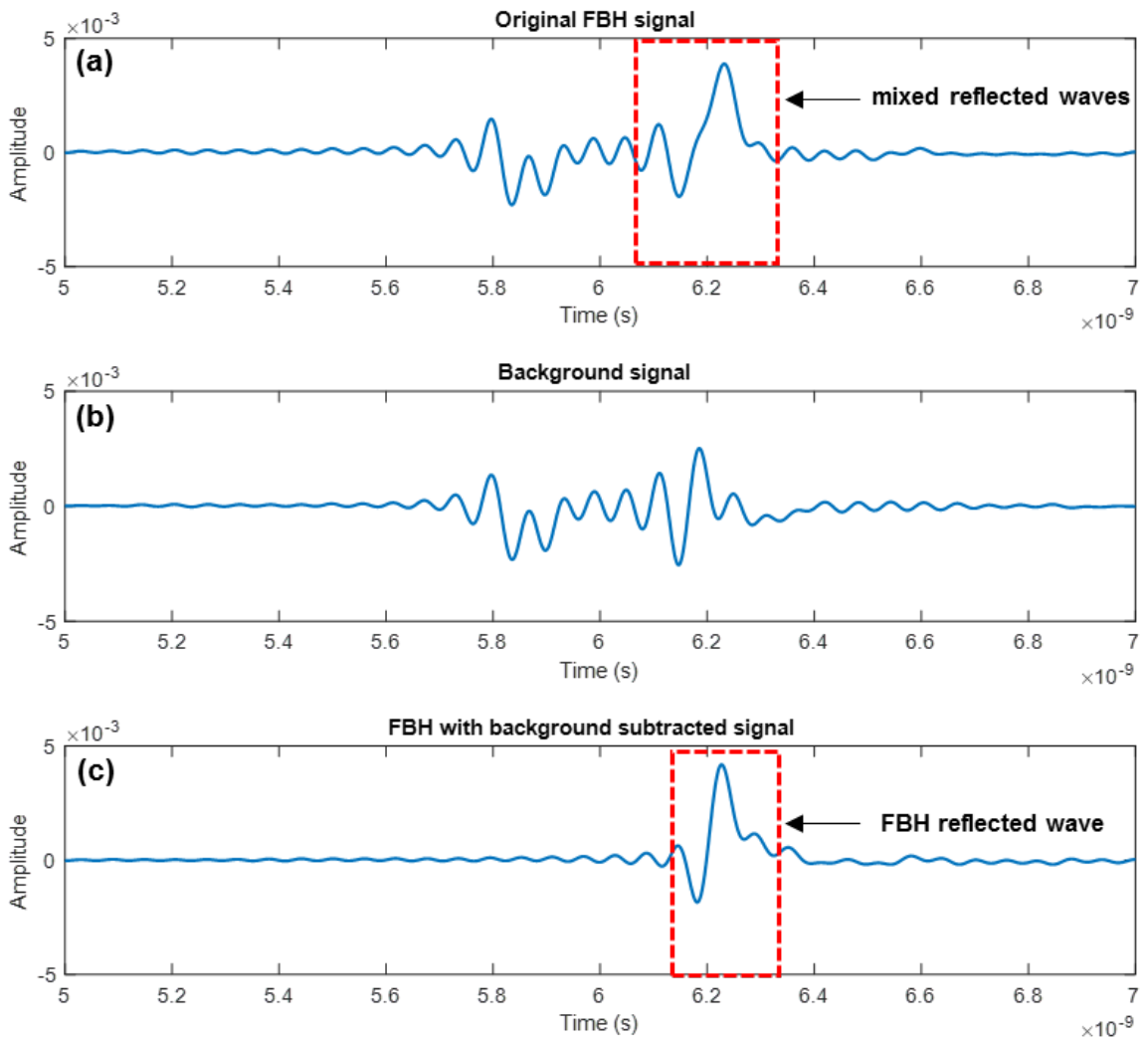


Figure 6.10 Time-domain signal at H1 centre: (a) original (b) background (c) background subtracted

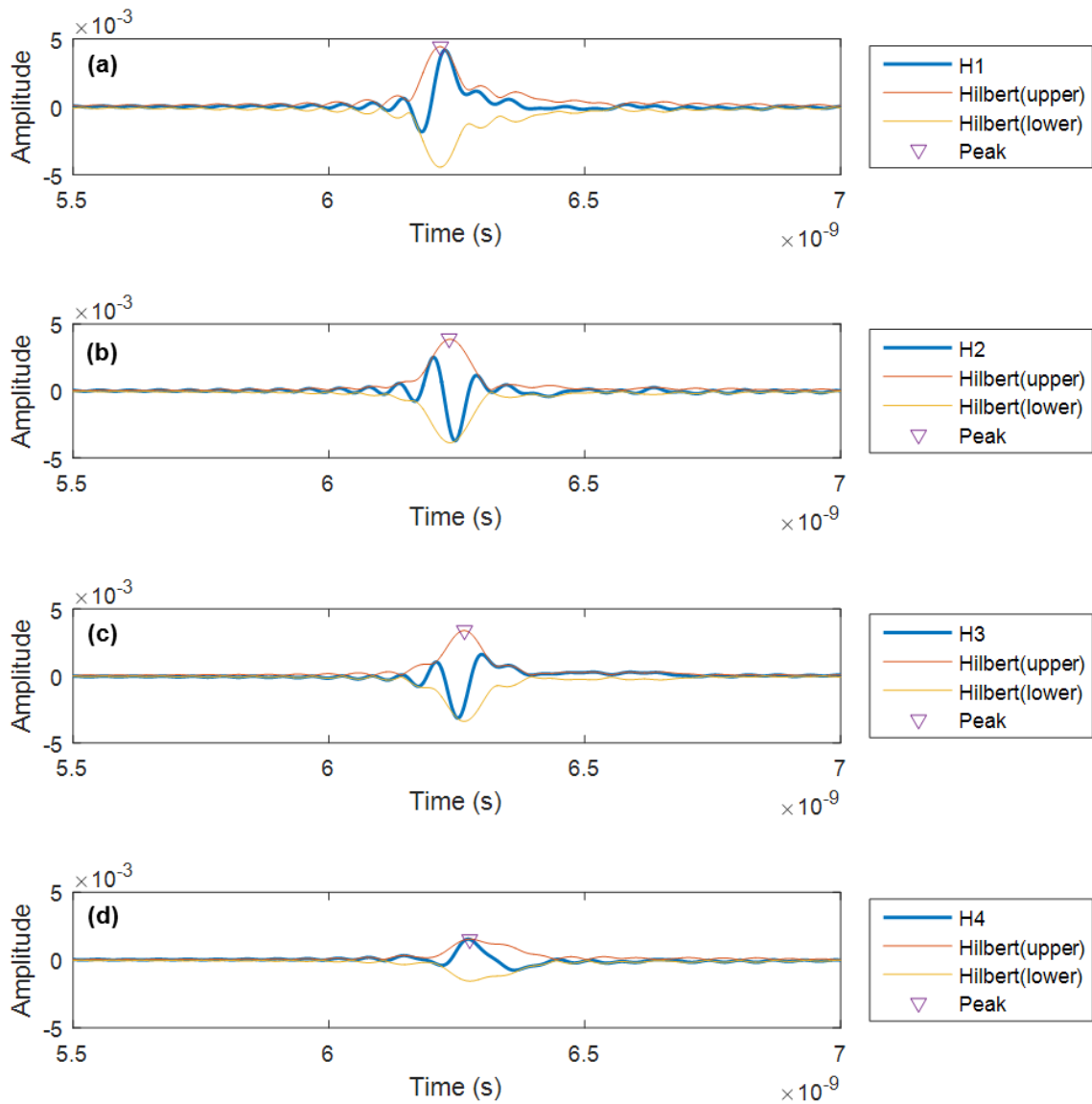


Figure 6.11 Reflected signals of FBHs: (a) H1, (b) H2, (c) H3 and (d) H4

Figure 6.9 shows the process for time-of-flight extraction for FBH depth estimation. The original FHB response is taken from the spectral response at the centre location of FBH and the background response is calculated from an average of spectral responses, excluding the ROI area, with the same probe height (the same y position). Prior to background subtraction, both responses are upsampling from 2^8 to 2^{14} samples by zero padding to improve timing resolution in the next process. Then, both spectral responses are converted into time-domain signals using inverse fast Fourier transform. To obtain the FHB reflected signal, we subtract the background from the original FHB signal as illustrated in Figure 6.10. Based on the proposed configuration, the time-domain signals of all FBH are essentially aligned, and thus the relative time-of-flight (ToF) between each reflected signals can be used to characterise depths of FBHs. Next, Hilbert transform is applied to the FBH reflected signals to obtain the envelopes as the magnitude of

their analytic signals. The time positions of reflected signals are located by the peak point of the Hilbert envelope as shown in Figure 6.11. Time and magnitude values at peak positions are listed in Table 6.5. Interestingly, it is found in the comparison of four reflected signals that their dispersion and attenuation increase by the increasing of defect depth. Finally, the capability for defect depth characterisation is demonstrated in the plot of ToF features (i.e., peak time and peak magnitude) against the FBH depths demonstrated in Figure 6.12. The graphs demonstrate that the relation between ToF features and the defect depth are monotonic and almost linear. It can be concluded that ToF of microwave reflected signal is a promising feature for characterisation of FBH depths.

Table 6.5 Time-of-flight features from FBHs

FBH depth (mm)	H1 = 4.0	H2 = 5.5	H3 = 8.0	H4 = 11.5
Peak time (ns)	6.217	6.232	6.266	6.277
Peak magnitude	4.44	3.84	3.38	1.55

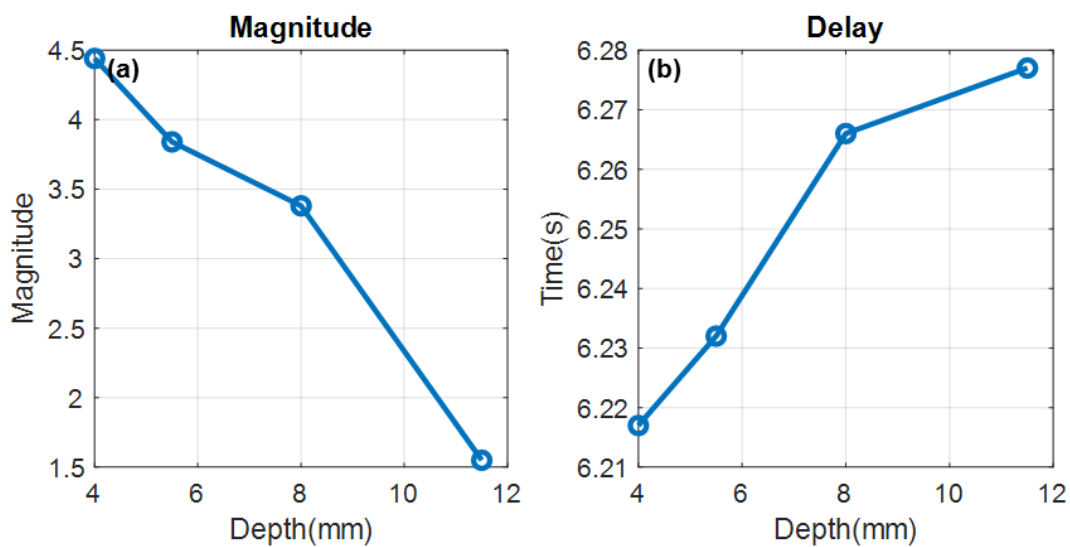


Figure 6.12 Time-of-flight feature against defect depth: (a) amplitude, (b) time delay

6.6 Chapter Summary

In this chapter, a novel application of microwave NDT for detection and characterisation of FBH defect in coated GFRP pipes is proposed. Initially, PCA is applied to search for ROI of FBHs and verify their locations using SAR tomography. The detected FBHs are evaluated for location, size and depth. It is found that PCA and SAR tomography are promising methods to overcome the adverse effect of pipe curvature. PCA factorise the data into a few principal components then only the correlated principal component (PC3) is selected for feature extraction of FHB. SAR tomography provides images of FHB responses with timing

information. In the quantitative evaluation of FHBs, PC feature and SAR Tomography can be verified and give location and size of the defect, whilst the depth of FHBs are estimated from relative time-of-flight of the FHB reflected signals.

Chapter 7 Conclusions and Future Work

This final chapter summarises and concludes the major contributions of this work. The suggestions for the potential improvement of the microwave NDT&E system for multilayered structures regarding future researches are outlined.

7.1 Conclusions of Major Contributions

In this project, System design and implementation of microwave NDT&E system using open-ended waveguide have been carried out based on challenges/problems of microwave NDT&E inspection for multilayered structures. Three dedicated multilayered models investigated in this work include corrosion under coating as the homogeneous dielectric layers backed by the perfect conductor, woven CFRP composites with impact damages as an inhomogeneous mixture of the conductive/dielectric compound, and thermal coated GFRP pipe with internal flat-bottom holes as layered dielectric composites with a curved surface. In each study, the significant findings and contributions of the work are concluded as follows.

The study of steel corrosion under coating demonstrates the capability of the microwave NDT&E system to inspect homogeneous layered dielectric structures backed by a conductive plate. Two microwave open-ended rectangular waveguide probes operating in Ku- and K-band are investigated with dedicated corrosion progression samples (0 – 12 months). The reflection coefficients are obtained from open corrosion and corrosion under coating by probing (A-scan) at the centre of the corrosion patch. The data are analysed for corrosion progression feature using PCA. It is found that PC-based feature can be effectively used as an indicator of the corrosion progression stages. The significant findings of the first study are summarised as follows.

1. The microwave inspection method using an open-ended waveguide probe and PCA is a promising tool for steel corrosion stages characterisation. The interactions between open-ended waveguide probe and properties of corrosion layer are highly sensitive resulting in deviation shifted in the resonant responses. PCA is successfully applied to extract the corrosion progression feature from the responses. It is also found that the PC1 features are invariant to probe parameters (i.e., aperture dimensions and operating frequency) and coating properties.
2. Following the investigation of open-ended waveguide probes at different operating frequencies, it is found that the responses from WR-62 probe operating at a frequency range between 9.5 GHz – 18 GHz are consistent for both coated and uncoated corrosion.

The WR-42 probe, on the other hand, shows multiple resonances/ripples and other influences such as surface roughness as evident in the PC3 features of the US samples.

3. A turning point of feature values is found at 6 months of corrosion progress. The initial falling trend is likely to be related to the increasing of corrosion thickness in early corrosion stages, while the influence of corrosion properties became stronger and reverse the trend in the latter stages.

In the study of woven conductive/dielectric composites, the EM responses of woven CFRP models with plain and 5HS structures are preliminarily investigated through numerical simulation. The simulation results are compared with the experimental study of 12-layers 5HS CFRP composites. It is found that an increase of the gap and ply thickness fibres will decrease the resonant frequency response; CFRP with different textile structures (e.g., plain and 5HS) and a number of plies generate different microwave responses. CFRP with wavier texture and more layers tend to generate higher resonances and ripples. Moreover, the preliminary experimental study of impact damage at 6 J on CFRP suggested that impact damage may alter the CFRP structure by narrowing the gap between fibres as demonstrated by similarity to the capacitance reducing effect causing slightly shifted of the microwave response to the higher frequency range.

In the experimental study of woven CFRP composite with impact damages, the K-band open-ended rectangular waveguide is utilised by scanning over the 5HS woven CFRP samples with impact damage at impact energies ranging from 2J to 10J. The reflection coefficient responses are obtained and analysed for optimal scanning step size and features for woven texture and impact damage visualisation. At the constant lift-off at 0.1mm, the scanning step size of $a/8$ is sufficient for detection of impact damage, while the step size of $a/20$ and below are required for visualisation of fibre texture.

The impact damage features of woven composite samples are successfully extracted by frequency selective PCA feature. It is found that the responses at different frequencies reflect distinctive information of the impact damages. The magnitude responses at eight significant frequency points were selected for feature extraction using PCA method. PCA was applied to study the training sample (6J) and extracted the significant principal components representing impact damage. Based on projection results, the sixth principal component (PC6) was selected for the feature extraction of impact damage on woven CFRP composites. The images of various impact damage samples have been reconstructed by projecting the test data to the selected PC. As results, the impact energies on the woven CFRP were characterised by the impact sizes.

The study of GFRP pipe composite with flat-bottom hole defects demonstrates the capability of microwave NDT&E scanning system for inspecting of irregular shape (curvature) and layered dielectric composites. An open-ended rectangular waveguide probe operating in K-band is utilised by scanning above the outer surface of GFRP pipe with inner flat-bottom hole defects. First, PCA is applied to search for a region of interest area of the defects and to verify their locations using SAR tomography. The detected FBHs are evaluated for location, size and depth. It is found that PCA and SAR tomography are promising techniques to overcome the adverse effect of pipe curvature (lift-off variation). PCA effectively factorise the data into a few principal components, then only the correlated principal component (PC3) is selected for feature extraction of FHB. SAR tomography provides images of FHB responses with timing information. In the quantitative evaluation of FHBs, PC feature and SAR tomography can be verified and give location and size of the defect, while the depths of FHBs are estimated from relative time-of-flight of the FHB reflected signals.

7.2 Future Work Suggestions

The proposed microwave NDT&E system together with quantitative evaluation frameworks have demonstrated the capability for inspection of various multilayered structures including homogenous layers of corrosion under coating, inhomogeneous of a compound of conductive and dielectric of woven CFRP, and dielectric laminated composite with curvature surface of thermal coated GFRP pipe. However, there are still significant challenges and problems needed to be addressed. Further investigations will focus on overcoming the challenges and problems in relation to improve the material models and extend the capability of the microwave NDT&E system and quantitative non-destructive evaluation algorithms regarding PCA and SAR methods.

The accurate models of multilayered structures of electromagnetic study should be further investigated in conjunction with PCA and SAR approaches. It is found in the literature that complex chemical compound such as corrosion is simply modelled as layered dielectric on a steel substrate. However, the chemical mixture and dimensions of corrosion change overtime as a function of environmental variables (e.g., moisture, oxygen, pH). In the early stage of corrosion, this model assumption of corrosion as the homogenous thin film could be valid. The later stages of corrosion involve geometrical variations as evident by metal loss and presences of pits in in the corrosion patch. Therefore, more parameters should be taken into consideration with the principal components extracted by PCA. For instance, with the directional properties (E-field direction) of the open-ended rectangular waveguide probe, the parameters such as

surface roughness based on material texture could be achieved by different angular scan technique.

Moreover, one may look into the correlation between multiple model parameters and the output principal components. The relationship between model parameters and principal component could be used to improve the accuracy of the offline PC training model for better characterisation and quantitative evaluation of defect and layer properties. Also, the accurate models of 3-D woven CFRP with accurate material properties (include anisotropic conductive properties of carbon fibre) and dimensions should be studied. The improvement of SAR algorithm and miniaturisation of the probe will help the reconstruction of the image with higher spatial resolution. This should overcome the challenge of BVID on woven CFRP at low energy (2J and below), where the size of the defect is comparable with the size of the woven texture. Moreover, the influences of measurement parameters such as lift-off and incident angle will be investigated to enhance the understanding of microwave responses and development of defect characterisation and parameter regression algorithms for woven composites.

For the feature extraction of multilayered composites, the future works will extend the PCA and SAR approaches and involve comparison studies between statistical based and other approaches such as analytical based and structural based approaches. The advantages and disadvantages of each approach will be analysed for better understanding and improve the feature extraction algorithms. The potential developed feature extraction could be the integration of multiple approaches by cascading, parallel processing or supervisory based algorithms. Also, it will look into more type of features and the fusion of significant features that give better sensitivity to the interesting parameters and mitigate uncorrelated influences. Advanced machine learning methods for non-linear problems such as kernel PCA will be investigated for the complex multivariate problems. Kernel PCA is a PCA extended method performing a nonlinear form of PCA in high-dimensional feature using nonlinear mapping. Unlike the conventional PCA, kernel PCA transforms original data to higher dimensional feature space and extracts a significantly larger number of nonlinear principal components allowing better extract of features.

In the further studies of visualisation based on SAR algorithm, it will investigate the advanced synthetic aperture algorithm such as autofocus algorithms that facilitates the reconstruction of 3-D volumetric data (holography) without estimation of target distance. The challenges of thin dielectric layers could be overcome by improving the bandwidth of the sweeping frequency, which equivalent to narrowing the pulse period in time-domain signal. Also, the works related to microwave and millimetre-wave single pixel camera should be taken into consideration. The

use of metamaterial lens that map targets upon a detector plane based on hardware compression technique without utilising of sensors array or requirement of mechanical target scanning technique.

For the data analysis, investigation of data compression such as compressed sensing (CS) should be taken into consideration. CS offers a reduction of the numbers of acquisition positions. Unlike the Shannon–Nyquist sampling theorem, CS can reconstruct signals from far fewer samples by finding sparse solutions to underdetermined linear systems. Therefore, it requires lower scanning time for the same scanning area, compared to that of the conventional C-scan technique. Overall visualisation process could be improved by integration of SAR with the CS technique. The quality of image reconstructed by the SAR algorithm remains sufficient by the compensation of CS, while the number of sampling positions is greatly reduced to minimise the scanning time. Moreover, the application of CS for feature extraction or supervised CS with feature extraction could be one of the future investigations.

Apart from the further investigations to overcome the current challenges and problem in microwave NDT&E technique, the topics of the internet of things (IoTs), edge computing and industrial 4.0 are currently in focus towards the direction of structural health monitoring (SHM). Therefore, the development of microwave NDT&E system with integration of embedded wireless communication network should be taken into account. With the more powerful embedded processors, the sensing unit may take responsibility for simple signal processing and feature extraction tasks, or even making a simple decision other than forwarding the information to the central unit. PCA is known to be one of the high computational efficiency methods for feature extraction and data dimensional reduction. The integration of PCA for feature extraction within the sensor unit is possible by utilising the well-trained model determined from the PCA training process with better performance computer. However, the PC offline model should be updated periodically to improve the accuracy and be able to handle the future tasks. Finally, the miniaturising of the overall microwave NDT&E system for portability and better integration with other sensing systems for multimodal sensing could be the future trend.

References

- [1] P. J. Shull, *Nondestructive Evaluation: Theory, Techniques, and Applications*. CRC Press, 2016.
- [2] Nirmalya Mukherjee, “COATING PRESENTATION,” presented at the SlideShare, Sep-2015.
- [3] L. Senni, L. Battaglini, P. Burrascano, S. Laureti, and M. Ricci, “Industrial Applications: Ultrasonic Inspection of Large Forgings,” in *Ultrasonic Nondestructive Evaluation Systems*, P. Burrascano, S. Callegari, A. Montisci, M. Ricci, and M. Versaci, Eds. Springer International Publishing, 2015, pp. 245–258.
- [4] V. Barranco, S. Feliu Jr., and S. Feliu, “EIS study of the corrosion behaviour of zinc-based coatings on steel in quiescent 3% NaCl solution. Part 1: directly exposed coatings,” *Corros. Sci.*, vol. 46, no. 9, pp. 2203–2220, Sep. 2004.
- [5] P. J. Schilling, B. R. Karedla, A. K. Tatiparthi, M. A. Verges, and P. D. Herrington, “X-ray computed microtomography of internal damage in fiber reinforced polymer matrix composites,” *Compos. Sci. Technol.*, vol. 65, no. 14, pp. 2071–2078, Nov. 2005.
- [6] P. DAVIES, D. CHOQUEUSE, B. BIGOURDAN, H. DEVAUX, and S. ROBERT, “Wave impact resistance of racing yacht composites,” *JEC Compos.*, no. 59, pp. 28–29, 2010.
- [7] S. Powell, “American Airlines: Boeing 787 Dreamliner Damaged By Hail – Returns To Beijing Airport,” *LoyaltyLobby*, 02-Aug-2015. .
- [8] H. Jiang and D. P. Kamdem, “Development of poly(vinyl chloride)/wood composites. A literature review,” *J. Vinyl Addit. Technol.*, vol. 10, no. 2, pp. 59–69, 2004.
- [9] A. R. Bunsell, J. Renard, and J. Renard, *Fundamentals of Fibre Reinforced Composite Materials*. CRC Press, 2005.
- [10] I. Kokcharov and A. Burov, “Structural integrity analysis,” *Switz. Geneva*, vol. 5, 2013.
- [11] R. Sutthaweekul and G. Y. Tian, “Steel Corrosion Stages Characterization Using Open-Ended Rectangular Waveguide Probe,” *IEEE Sens. J.*, vol. 18, no. 3, pp. 1054–1062, Feb. 2018.
- [12] R. Sutthaweekul, A. M. J. Marindra, and G. Y. Tian, “Study of microwave responses on layered woven CFRP composites,” in *2017 9th International Conference on Information Technology and Electrical Engineering (ICITEE)*, 2017, pp. 1–5.
- [13] R. Sutthaweekul, G. Y. Tian, and M. D. Buhari, “Detection of impact damage and fibre texture on CFRP using open-ended waveguide probe,” in *2016 13th International Conference on Electrical Engineering/Electronics, Computer, Telecommunications and Information Technology (ECTI-CON)*, 2016, pp. 1–6.
- [14] R. Sutthaweekul, G. Tian, Z. Wang, and F. Ciampa, “Microwave open-ended waveguide for detection and characterisation of FBHs in coated GFRP pipes,” *Compos. Struct.*, vol. 225, p. 111080, Oct. 2019.
- [15] R. Sutthaweekul, M. D. Buhari, A. I. Sunny, and G. Y. Tian, “Influence of lift-off on microwave open-ended waveguide time of flight based tire inspection,” in *2016 International Conference for Students on Applied Engineering (ICSAE)*, 2016, pp. 275–279.
- [16] C. Tang, G. Y. Tian, K. Li, R. Sutthaweekul, and J. Wu, “Smart Compressed Sensing for Online Evaluation of CFRP Structure Integrity,” *IEEE Trans. Ind. Electron.*, vol. PP, no. 99, pp. 1–1, 2017.
- [17] W. J. Cantwell and J. Morton, “Detection of impact damage in CFRP laminates,” *Compos. Struct.*, vol. 3, no. 3–4, pp. 241–257, 1985.

- [18] D. Balageas *et al.*, “Thermal (IR) and Other NDT Techniques for Improved Material Inspection,” *J. Nondestruct. Eval.*, vol. 35, no. 1, p. 18, Mar. 2016.
- [19] P. Vaara, J. Leinonen, and others, “Technology survey on NDT of carbon-fiber composites,” *Kemi-Tornio Univ Appl Sci Kemi Finl. Tech Rep*, 2012.
- [20] S. Gäbler, H. Heuer, G. Heinrich, and R. Kupke, “Quantitatively analyzing dielectrical properties of resins and mapping permittivity variations in CFRP with high-frequency eddy current device technology,” *AIP Conf. Proc.*, vol. 1650, no. 1, pp. 336–344, Mar. 2015.
- [21] L. B. Pedersen, K.-Å. Magnusson, and Y. Zhengsheng, “Eddy Current Testing of Thin Layers Using Co-planar Coils,” *Res. Nondestruct. Eval.*, vol. 12, no. 1, pp. 53–64, Mar. 2000.
- [22] Y. He, G. Tian, H. Zhang, M. Alamin, A. Simm, and P. Jackson, “Steel Corrosion Characterization Using Pulsed Eddy Current Systems,” *IEEE Sens. J.*, vol. 12, no. 6, pp. 2113–2120, Jun. 2012.
- [23] R. Grimberg and G.-Y. Tian, “High-frequency electromagnetic non-destructive evaluation for high spatial resolution, using metamaterials,” *Proc R Soc A*, p. rspa20110666, May 2012.
- [24] G. Bardl *et al.*, “Automated detection of yarn orientation in 3D-draped carbon fiber fabrics and preforms from eddy current data,” *Compos. Part B Eng.*, vol. 96, pp. 312–324, Jul. 2016.
- [25] G. Y. Tian, Y. Li, and C. Mandache, “Study of Lift-Off Invariance for Pulsed Eddy-Current Signals,” *IEEE Trans. Magn.*, vol. 45, no. 1, pp. 184–191, Jan. 2009.
- [26] L. W. Schmerr, “An Ultrasonic System,” in *Fundamentals of Ultrasonic Nondestructive Evaluation: A Modeling Approach*, L. W. Schmerr Jr., Ed. Cham: Springer International Publishing, 2016, pp. 1–13.
- [27] E. H. El Boudouti, B. Djafari-Rouhani, A. Akjouj, and L. Dobrzynski, “Acoustic waves in solid and fluid layered materials,” *Surf. Sci. Rep.*, vol. 64, no. 11, pp. 471–594, Nov. 2009.
- [28] C. B. Scruby and L. E. Drain, *Laser ultrasonics techniques and applications*. CRC Press, 1990.
- [29] M. Sgarbi, V. Colla, S. Cateni, and S. Higson, “Pre-processing of data coming from a laser-EMAT system for non-destructive testing of steel slabs,” *ISA Trans.*, vol. 51, no. 1, pp. 181–188, Jan. 2012.
- [30] W.-B. Na and T. Kundu, “Inspection of interfaces between corroded steel bars and concrete using the combination of a piezoelectric zirconate-titanate transducer and an electromagnetic acoustic transducer,” *Exp. Mech.*, vol. 43, no. 1, pp. 24–31, 2003.
- [31] M. Le, J. Kim, S. Kim, and J. Lee, “B-scan ultrasonic testing of rivets in multilayer structures based on short-time Fourier transform analysis,” *Measurement*, vol. 128, pp. 495–503, Nov. 2018.
- [32] H. Liu *et al.*, “High-frequency ultrasonic methods for determining corrosion layer thickness of hollow metallic components,” *Ultrasonics*, vol. 89, pp. 166–172, Sep. 2018.
- [33] R. Yang and Y. He, “Optically and non-optically excited thermography for composites: A review,” *Infrared Phys. Technol.*, vol. 75, pp. 26–50, Mar. 2016.
- [34] F. Khodayar, S. Sojasi, and X. Maldague, “Infrared thermography and NDT: 2050 horizon,” *Quant. InfraRed Thermogr. J.*, vol. 13, no. 2, pp. 210–231, Jul. 2016.

- [35] H. Zhang *et al.*, “A Review of Microwave Thermography Nondestructive Testing and Evaluation,” *Sensors*, vol. 17, no. 5, p. 1123, May 2017.
- [36] F. Ciampa, P. Mahmoodi, F. Pinto, and M. Meo, “Recent Advances in Active Infrared Thermography for Non-Destructive Testing of Aerospace Components,” *Sensors*, vol. 18, no. 2, p. 609, Feb. 2018.
- [37] D. P. Almond, S. L. Angioni, and S. G. Pickering, “Long pulse excitation thermographic non-destructive evaluation,” *NDT E Int.*, vol. 87, pp. 7–14, Apr. 2017.
- [38] Z. Li, A. Haigh, C. Soutis, and A. Gibson, “Principles and Applications of Microwave Testing for Woven and Non-Woven Carbon Fibre-Reinforced Polymer Composites: a Topical Review,” *Appl. Compos. Mater.*, pp. 1–18, Aug. 2018.
- [39] N. P. Avdelidis, B. C. Hawtin, and D. P. Almond, “Transient thermography in the assessment of defects of aircraft composites,” *Ndt E Int.*, vol. 36, no. 6, pp. 433–439, 2003.
- [40] J. G. Sun, “Analysis of pulsed thermography methods for defect depth prediction,” *J. Heat Transf.*, vol. 128, no. 4, pp. 329–338, 2006.
- [41] V. P. Vavilov and S. S. Pawar, “A novel approach for one-sided thermal nondestructive testing of composites by using infrared thermography,” *Polym. Test.*, vol. 44, pp. 224–233, 2015.
- [42] V. P. Vavilov and D. D. Burleigh, “Review of pulsed thermal NDT: Physical principles, theory and data processing,” *Ndt E Int.*, vol. 73, pp. 28–52, 2015.
- [43] C. Meola, G. M. Carlomagno, A. Squillace, and A. Vitiello, “Non-destructive evaluation of aerospace materials with lock-in thermography,” *Eng. Fail. Anal.*, vol. 13, no. 3, pp. 380–388, 2006.
- [44] U. Polimeno, D. P. Almond, B. Weekes, and E. W. J. Chen, “A compact thermosonic inspection system for the inspection of composites,” *Compos. Part B Eng.*, vol. 59, pp. 67–73, 2014.
- [45] Y. He, G. Tian, M. Pan, and D. Chen, “Impact evaluation in carbon fiber reinforced plastic (CFRP) laminates using eddy current pulsed thermography,” *Compos. Struct.*, vol. 109, pp. 1–7, Mar. 2014.
- [46] T. Liang, W. Ren, G. Y. Tian, M. Elradi, and Y. Gao, “Low energy impact damage detection in CFRP using eddy current pulsed thermography,” *Compos. Struct.*, vol. 143, pp. 352–361, May 2016.
- [47] S.-A. Keo, D. Defer, F. Breaban, and F. Brachelet, “Comparison between Microwave Infrared Thermography and CO₂ Laser Infrared Thermography in Defect Detection in Applications with CFRP,” *Mater. Sci. Appl.*, vol. 04, no. 10, pp. 600–605, 2013.
- [48] A. Foudazi, M. T. Ghasr, and K. M. Donnell, “Characterization of Corroded Reinforced Steel Bars by Active Microwave Thermography,” *IEEE Trans. Instrum. Meas.*, vol. 64, no. 9, pp. 2583–2585, Sep. 2015.
- [49] R. Hanke, T. Fuchs, and N. Uhlmann, “X-ray based methods for non-destructive testing and material characterization,” *Nucl. Instrum. Methods Phys. Res. Sect. Accel. Spectrometers Detect. Assoc. Equip.*, vol. 591, no. 1, pp. 14–18, Jun. 2008.
- [50] J. M. Warnett *et al.*, “Towards in-process x-ray CT for dimensional metrology,” *Meas. Sci. Technol.*, vol. 27, no. 3, p. 035401, 2016.
- [51] H. Rolland, N. Saintier, P. Wilson, J. Merzeau, and G. Robert, “In situ X-ray tomography investigation on damage mechanisms in short glass fibre reinforced

- thermoplastics: Effects of fibre orientation and relative humidity,” *Compos. Part B Eng.*, vol. 109, pp. 170–186, 2017.
- [52] F. Sket, A. Enfedaque, C. Alton, C. González, J. M. Molina-Aldareguia, and J. Llorca, “Automatic quantification of matrix cracking and fiber rotation by X-ray computed tomography in shear-deformed carbon fiber-reinforced laminates,” *Compos. Sci. Technol.*, vol. 90, pp. 129–138, Jan. 2014.
- [53] B. Dong *et al.*, “Visualized tracing of rebar corrosion evolution in concrete with x-ray micro-computed tomography method,” *Cem. Concr. Compos.*, vol. 92, pp. 102–109, Sep. 2018.
- [54] W. Holub, U. Haßler, and E. Fraunhofer, “XXL X-ray Computed Tomography for Wind Turbines in the lab and on-site,” in *Proceedings of the NDT in Canada 2013 conference in conjunction with the international workshop on smart materials & structures, SHM and NDT for the Energy Industry. Calgary, Alberta, 2013*, pp. 49–54.
- [55] G. Chiesura *et al.*, “A Micro-Computed Tomography Technique to Study the Quality of Fibre Optics Embedded in Composite Materials,” *Sensors*, vol. 15, no. 5, pp. 10852–10871, May 2015.
- [56] M. Endrizzi, B. I. S. Murat, P. Fromme, and A. Olivo, “Edge-illumination X-ray dark-field imaging for visualising defects in composite structures,” *Compos. Struct.*, vol. 134, pp. 895–899, Dec. 2015.
- [57] S. Kharkovsky and R. Zoughi, “Microwave and millimeter wave nondestructive testing and evaluation - Overview and recent advances,” *IEEE Instrum. Meas. Mag.*, vol. 10, no. 2, pp. 26–38, Apr. 2007.
- [58] M. W. Hyde, A. E. Bogle, and M. J. Havrilla, “Nondestructive Characterization of PEC-Backed Materials Using the Combined Measurements of a Rectangular Waveguide and Coaxial Probe,” *IEEE Microw. Wirel. Compon. Lett.*, vol. 24, no. 11, pp. 808–810, Nov. 2014.
- [59] D. Micheli, C. Apollo, R. Pastore, and M. Marchetti, “X-Band microwave characterization of carbon-based nanocomposite material, absorption capability comparison and RAS design simulation,” *Compos. Sci. Technol.*, vol. 70, no. 2, pp. 400–409, Feb. 2010.
- [60] S. I. Ganchev, J. Bhattacharyya, S. Bakhtiari, N. Qaddoumi, D. Brandenburg, and R. Zoughi, “Microwave diagnosis of rubber compounds,” *IEEE Trans. Microw. Theory Tech.*, vol. 42, no. 1, pp. 18–24, Jan. 1994.
- [61] I. L. AL-Qadi and S. Lahouar, “Measuring layer thicknesses with GPR – Theory to practice,” *Constr. Build. Mater.*, vol. 19, no. 10, pp. 763–772, Dec. 2005.
- [62] O. Tantot, M. Chatard-Moulin, and P. Guillon, “Measurement of complex permittivity and permeability and thickness of multilayered medium by an open-ended waveguide method,” *IEEE Trans. Instrum. Meas.*, vol. 46, no. 2, pp. 519–522, Apr. 1997.
- [63] S. Bakhtiari, S. I. Ganchev, and R. Zoughi, “Open-ended rectangular waveguide for nondestructive thickness measurement and variation detection of lossy dielectric slabs backed by a conducting plate,” *IEEE Trans. Instrum. Meas.*, vol. 42, no. 1, pp. 19–24, Feb. 1993.
- [64] C.-Y. Yeh and R. Zoughi, “A novel microwave method for detection of long surface cracks in metals,” *IEEE Trans. Instrum. Meas.*, vol. 43, no. 5, pp. 719–725, Oct. 1994.

- [65] N. Qaddoumi, E. Ranu, J. D. McColskey, R. Mirshahi, and R. Zoughi, "Microwave Detection of Stress-Induced Fatigue Cracks in Steel and Potential for Crack Opening Determination," *Res. Nondestruct. Eval.*, vol. 12, no. 2, pp. 87–103, Jan. 2000.
- [66] H. Zhang, B. Gao, G. Y. Tian, W. L. Woo, and L. Bai, "Metal defects sizing and detection under thick coating using microwave NDT," *NDT E Int.*, vol. 60, pp. 52–61, Dec. 2013.
- [67] D. Hughes *et al.*, "Microwave Nondestructive Detection of Corrosion Under Thin Paint and Primer in Aluminum Panels," *Subsurf. Sens. Technol. Appl.*, vol. 2, no. 4, pp. 435–471, Oct. 2001.
- [68] S. Kharkovsky and R. Zoughi, "Millimeter Wave Nondestructive Evaluation of Corrosion Under Paint in Steel Structures," *AIP Conf. Proc.*, vol. 820, no. 1, pp. 1277–1283, Mar. 2006.
- [69] N. H. Baba, R. Ibrahim, N. Tamyis, and S. Subahir, "Free space microwave measurement for detecting corrosion under a thin paint of aluminium panel," in *2012 IEEE Student Conference on Research and Development (SCORED)*, 2012, pp. 277–282.
- [70] C.-H. Ryu, S.-H. Park, D.-H. Kim, K.-Y. Jhang, and H.-S. Kim, "Nondestructive evaluation of hidden multi-delamination in a glass-fiber-reinforced plastic composite using terahertz spectroscopy," *Compos. Struct.*, vol. 156, pp. 338–347, Nov. 2016.
- [71] A. Hosoi, Y. Yamaguchi, Y. Ju, Y. Sato, and T. Kitayama, "Detection of delamination in GFRP and CFRP by microwaves with focusing mirror sensor," in *Materials Science Forum*, 2013, vol. 750, pp. 142–146.
- [72] P. Wang, M. Liu, and Z. Wang, "Three-dimensional SAR imaging of sea targets with low PRF sampling," *Sonar Navig. IET Radar*, vol. 12, no. 3, pp. 294–300, 2018.
- [73] M. Fallahpour, J. T. Case, M. T. Ghasr, and R. Zoughi, "Piecewise and Wiener Filter-Based SAR Techniques for Monostatic Microwave Imaging of Layered Structures," *IEEE Trans. Antennas Propag.*, vol. 62, no. 1, pp. 282–294, Jan. 2014.
- [74] J. T. Case, M. T. Ghasr, and R. Zoughi, "Optimum 2-D Nonuniform Spatial Sampling for Microwave SAR-Based NDE Imaging Systems," *IEEE Trans. Instrum. Meas.*, vol. 61, no. 11, pp. 3072–3083, Nov. 2012.
- [75] M. T. Ghasr, K. P. Ying, and R. Zoughi, "SAR imaging for inspection of metallic surfaces at millimeter wave frequencies," in *Instrumentation and Measurement Technology Conference (I2MTC) Proceedings, 2014 IEEE International*, 2014, pp. 1202–1206.
- [76] N. N. Qaddoumi, W. M. Saleh, and M. Abou-Khousa, "Innovative Near-Field Microwave Nondestructive Testing of Corroded Metallic Structures Utilizing Open-Ended Rectangular Waveguide Probes," *IEEE Trans. Instrum. Meas.*, vol. 56, no. 5, pp. 1961–1966, Oct. 2007.
- [77] H. Kurokawa, A. Todoroki, and Y. Mizutani, "Damage Monitoring of CFRP Plate Using Self-Sensing TDR Method," *J. Solid Mech. Mater. Eng.*, vol. 6, no. 12, pp. 1053–1061, 2012.
- [78] A. Todoroki, K. Ohara, Y. Mizutani, Y. Suzuki, and R. Matsuzaki, "Lightning strike damage detection at a fastener using self-sensing TDR of composite plate," *Compos. Struct.*, vol. 132, pp. 1105–1112, Nov. 2015.
- [79] Z. Li *et al.*, "Detection of Impact Damage in Carbon Fiber Composites Using an Electromagnetic Sensor," *Res. Nondestruct. Eval.*, vol. 29, no. 3, pp. 123–142, Jul. 2018.

- [80] A. Galehdar, W. S. T. Rowe, K. Ghorbani, P. J. Callus, S. John, and C. H. Wang, "The Effect of Ply Orientation on the Performance of Antennas in or on Carbon Fiber Composites," *Prog. Electromagn. Res.*, vol. 116, pp. 123–136, 2011.
- [81] S. Kharkovsky and R. Zoughi, "Application of Near-Field Microwave and Millimeter Wave Nondestructive Testing for Evaluation of Fiber Breakage and Orientation Evaluation in CFRP Composite Patches," *AIP Conf. Proc.*, vol. 760, no. 1, pp. 554–561, Apr. 2005.
- [82] W. C. Wilson, J. P. Moore, and P. D. Juarez, "Remote strain sensing of CFRP using microwave frequency domain reflectometry," in *2016 IEEE National Aerospace and Electronics Conference (NAECON) and Ohio Innovation Summit (OIS)*, 2016, pp. 401–406.
- [83] B. Akuthota, D. Hughes, R. Zoughi, J. Myers, and A. Nanni, "Near-Field Microwave Detection of Disbond in Carbon Fiber Reinforced Polymer Composites Used for Strengthening Cement-Based Structures and Disbond Repair Verification," *J. Mater. Civ. Eng.*, vol. 16, no. 6, pp. 540–546, Nov. 2004.
- [84] A. S. Bin Sediq and N. Qaddoumi, "Near-field microwave image formation of defective composites utilizing open-ended waveguides with arbitrary cross sections," *Compos. Struct.*, vol. 71, no. 3–4, pp. 343–348, Dec. 2005.
- [85] K.-B. K. Seung-Hwan Yang, "Non-contact detection of impact damage in CFRP composites using millimeter-wave reflection and considering carbon fiber direction," *NDT Amp E Int.*, vol. 57, pp. 45–51, 2013.
- [86] Z. Li, A. Haigh, C. Soutis, A. Gibson, and R. Sloan, "Applications of microwave techniques for aerospace composites," in *2017 IEEE International Conference on Microwaves, Antennas, Communications and Electronic Systems (COMCAS)*, 2017, pp. 1–4.
- [87] D. J. Daniels, *Ground Penetrating Radar, 2nd Edition*, 2nd ed. IET, 2004.
- [88] A. S. Turk, K. A. Hocaoglu, and A. A. Vertiy, *Subsurface Sensing*. John Wiley & Sons, 2011.
- [89] R. Persico, *Introduction to Ground Penetrating Radar: Inverse Scattering and Data Processing*. John Wiley & Sons, 2014.
- [90] M. Metwaly, "Application of GPR technique for subsurface utility mapping: A case study from urban area of Holy Mecca, Saudi Arabia," *Measurement*, vol. 60, pp. 139–145, Jan. 2015.
- [91] Z. Khakiev, V. Shapovalov, A. Kruglikov, and V. Yavna, "GPR determination of physical parameters of railway structural layers," *J. Appl. Geophys.*, vol. 106, pp. 139–145, Jul. 2014.
- [92] W. Shao, A. Bouzerdoum, S. L. Phung, L. Su, B. Indraratna, and C. Rujikiatkamjorn, "Automatic Classification of Ground-Penetrating-Radar Signals for Railway-Ballast Assessment," *IEEE Trans. Geosci. Remote Sens.*, vol. 49, no. 10, pp. 3961–3972, Oct. 2011.
- [93] I. Catapano *et al.*, "Microwave tomography enhanced GPR surveys in Centaur's Domus, Regio VI of Pompeii, Italy," *J. Geophys. Eng.*, vol. 9, no. 4, p. S92, Aug. 2012.
- [94] V. Teodoridis, T. Sphicopoulos, and F. E. Gardiol, "The Reflection from an Open-Ended Rectangular Waveguide Terminated by a Layered Dielectric Medium," *IEEE Trans. Microw. Theory Tech.*, vol. 33, no. 5, pp. 359–366, May 1985.
- [95] M. T. Ghasr, M. J. Horst, M. Lechuga, R. Rapoza, C. J. Renoud, and R. Zoughi, "Accurate One-Sided Microwave Thickness Evaluation of Lined-Fiberglass Composites," *IEEE Trans. Instrum. Meas.*, vol. 64, no. 10, pp. 2802–2812, Oct. 2015.

- [96] R. Zoughi, J. R. Gallion, and M. T. Ghasr, "Accurate Microwave Measurement of Coating Thickness on Carbon Composite Substrates," *IEEE Trans. Instrum. Meas.*, vol. 65, no. 4, pp. 951–953, Apr. 2016.
- [97] A. M. Yadegari, R. Moini, S. H. H. Sadeghi, and F. Mazlumi, "Output signal prediction of an open-ended rectangular waveguide probe when scanning cracks at a non-zero lift-off," *NDT E Int.*, vol. 43, no. 1, pp. 1–7, Jan. 2010.
- [98] R. MacPhie and A. Zaghoul, "Radiation from a rectangular waveguide with infinite flange—Exact solution by the correlation matrix method," *IEEE Trans. Antennas Propag.*, vol. 28, no. 4, pp. 497–503, Jul. 1980.
- [99] H. Baudrand, J.- Tao, and J. Atechian, "Study of radiating properties of open-ended rectangular waveguides," *IEEE Trans. Antennas Propag.*, vol. 36, no. 8, pp. 1071–1077, Aug. 1988.
- [100] C.-W. Chang, Y. F. Chen, and J. Qian, "Nondestructive determination of electromagnetic parameters of dielectric materials at X-band frequencies using a waveguide probe system," *IEEE Trans. Instrum. Meas.*, vol. 46, no. 5, pp. 1084–1092, Oct. 1997.
- [101] C.-W. Chang, K.-M. Chen, and J. Qian, "Nondestructive measurements of complex tensor permittivity of anisotropic materials using a waveguide probe system," *IEEE Trans. Microw. Theory Tech.*, vol. 44, no. 7, pp. 1081–1090, Jul. 1996.
- [102] Marc. C. Decreton and F. E. Gardiol, "Simple Nondestructive Method for the Measurement of Complex Permittivity," *IEEE Trans. Instrum. Meas.*, vol. 23, no. 4, pp. 434–438, Dec. 1974.
- [103] M. C. Decreton and M. S. Ramachandraiah, "Nondestructive Measurement of Complex Permittivity for Dielectric Slabs (Short Papers)," *IEEE Trans. Microw. Theory Tech.*, vol. 23, no. 12, pp. 1077–1080, Dec. 1975.
- [104] S. I. Ganchev, S. Bakhtiari, and R. Zoughi, "A novel numerical technique for dielectric measurement of generally lossy dielectrics," *IEEE Trans. Instrum. Meas.*, vol. 41, no. 3, pp. 361–365, Jun. 1992.
- [105] S. Kim, J. Surek, and J. Baker-Jarvis, "Electromagnetic Metrology on Concrete and Corrosion," *J. Res. Natl. Inst. Stand. Technol.*, vol. 116, no. 3, pp. 655–669, 2011.
- [106] D. de la Fuente, I. Díaz, J. Simancas, B. Chico, and M. Morcillo, "Long-term atmospheric corrosion of mild steel," *Corros. Sci.*, vol. 53, no. 2, pp. 604–617, Feb. 2011.
- [107] M. Morcillo, D. De la Fuente, I. Díaz, and H. Cano, "Atmospheric corrosion of mild steel," *Rev. Metal.*, vol. 47, no. 5, pp. 426–444, Oct. 2011.
- [108] R. E. Melchers, "Mathematical modelling of the diffusion controlled phase in marine immersion corrosion of mild steel," *Corros. Sci.*, vol. 45, no. 5, pp. 923–940, May 2003.
- [109] U. R. Evans, *The Corrosion and Oxidation of Metals: Scientific Principles and Practical Applications.-Repr. Hauptbd., 1961*. Arnold, 1961.
- [110] D. A. Jones, *Principles and Prevention of Corrosion: Pearson New International Edition, 2 edition*. Pearson, 2013.
- [111] G. H. J. Tammann, *Lehrbuch der Metallographie: Chemie und Physik der Metalle und ihrer Legierungen*. S.l.: Adamant Media Corporation, 2001.
- [112] H. R. Copson, "A theory of the mechanism of rusting of low alloy steels in the atmosphere," in *Proceedings-American Society for Testing and Materials*, 1945, vol. 45, pp. 554–580.

- [113] I. Suzuki, Y. Hisamatsu, and N. Masuko, “Nature of Atmospheric Rust on Iron,” *J. Electrochem. Soc.*, vol. 127, no. 10, pp. 2210–2215, Oct. 1980.
- [114] K. Asami and M. Kikuchi, “In-depth distribution of rusts on a plain carbon steel and weathering steels exposed to coastal–industrial atmosphere for 17 years,” *Corros. Sci.*, vol. 45, no. 11, pp. 2671–2688, Nov. 2003.
- [115] P. Dillmann, F. Mazaudier, and S. Hoërlé, “Advances in understanding atmospheric corrosion of iron. I. Rust characterisation of ancient ferrous artefacts exposed to indoor atmospheric corrosion,” *Corros. Sci.*, vol. 46, no. 6, pp. 1401–1429, Jun. 2004.
- [116] N. N. Qaddoumi, W. M. Saleh, and M. Abou-Khousa, “Innovative Near-Field Microwave Nondestructive Testing of Corroded Metallic Structures Utilizing Open-Ended Rectangular Waveguide Probes,” *IEEE Trans. Instrum. Meas.*, vol. 56, no. 5, pp. 1961–1966, Oct. 2007.
- [117] H. Zhang, Y. He, B. Gao, G. Y. Tian, L. Xu, and R. Wu, “Evaluation of Atmospheric Corrosion on Coated Steel Using K-Band Sweep Frequency Microwave Imaging,” *IEEE Sens. J.*, vol. 16, no. 9, pp. 3025–3033, May 2016.
- [118] G. a. O. Davies and R. Olsson, “Impact on composite structures,” *Aeronaut. J.*, vol. 108, no. 1089, pp. 541–563, Nov. 2004.
- [119] S. Abrate, *Impact on Composite Structures*. Cambridge University Press, 2005.
- [120] A. Elias, F. Laurin, M. Kaminski, and L. Gornet, “Experimental and numerical investigations of low energy/velocity impact damage generated in 3D woven composite with polymer matrix,” *Compos. Struct.*, vol. 159, pp. 228–239, Jan. 2017.
- [121] M. O. W. Richardson and M. J. Wisheart, “Review of low-velocity impact properties of composite materials,” *Compos. Part Appl. Sci. Manuf.*, vol. 27, no. 12, pp. 1123–1131, 1996.
- [122] M. V. Donadon, L. Iannucci, B. G. Falzon, J. M. Hodgkinson, and S. F. M. de Almeida, “A progressive failure model for composite laminates subjected to low velocity impact damage,” *Comput. Struct.*, vol. 86, no. 11–12, pp. 1232–1252, Jun. 2008.
- [123] S. Kharkovsky, A. C. Ryley, V. Stephen, and R. Zoughi, “Dual-Polarized Near-Field Microwave Reflectometer for Noninvasive Inspection of Carbon Fiber Reinforced Polymer-Strengthened Structures,” *IEEE Trans. Instrum. Meas.*, vol. 57, no. 1, pp. 168–175, Jan. 2008.
- [124] R. Zoughi, J. R. Gallion, and M. T. Ghasr, “Accurate Microwave Measurement of Coating Thickness on Carbon Composite Substrates,” *IEEE Trans. Instrum. Meas.*, vol. 65, no. 4, pp. 951–953, Apr. 2016.
- [125] Y. Pang, H. Cheng, Y. Zhou, and J. Wang, “Analysis and enhancement of the bandwidth of ultrathin absorbers based on high-impedance surfaces,” *J. Phys. Appl. Phys.*, vol. 45, no. 21, p. 215104, 2012.
- [126] S. M. A. M. H. Abadi and N. Behdad, “Inductively-Coupled Miniaturized-Element Frequency Selective Surfaces With Narrowband, High-Order Bandpass Responses,” *IEEE Trans. Antennas Propag.*, vol. 63, no. 11, pp. 4766–4774, Nov. 2015.
- [127] L. Li *et al.*, “Reconfigurable all-dielectric metamaterial frequency selective surface based on high-permittivity ceramics,” *Sci. Rep.*, vol. 6, p. srep24178, Apr. 2016.
- [128] M. Majidzadeh, C. Ghobadi, and J. Nourinia, “Quadruple filtering mechanism through an effective sketch of reconfigurable frequency selective surface,” *Antennas Propag. IET Microw.*, vol. 10, no. 15, pp. 1605–1612, 2016.

- [129] T. K. Wu, *Frequency Selective Surface and Grid Array*. Wiley, 1995.
- [130] M. Gao, S. M. A. M. H. Abadi, and N. Behdad, "A Hybrid Miniaturized-Element Frequency Selective Surface With a Third-Order Bandpass Response," *IEEE Antennas Wirel. Propag. Lett.*, vol. 16, pp. 708–711, 2017.
- [131] D. Sánchez-Escuderos, H. C. Moy-Li, E. Antonino-Daviu, M. Cabedo-Fabrés, and M. Ferrando-Bataller, "Microwave Planar Lens Antenna Designed With a Three-Layer Frequency-Selective Surface," *IEEE Antennas Wirel. Propag. Lett.*, vol. 16, pp. 904–907, 2017.
- [132] M. S. Mirotznik, S. Yarlagadda, R. McCauley, and P. Pa, "Broadband Electromagnetic Modeling of Woven Fabric Composites," *IEEE Trans. Microw. Theory Tech.*, vol. 60, no. 1, pp. 158–169, Jan. 2012.
- [133] J. Wang, B. Zhou, L. Shi, C. Gao, and B. Chen, "Analyzing the Electromagnetic Performances of Composite Materials With the FDTD Method," *IEEE Trans. Antennas Propag.*, vol. 61, no. 5, pp. 2646–2654, May 2013.
- [134] R. Rafiee, "On the mechanical performance of glass-fibre-reinforced thermosetting-resin pipes: A review," *Compos. Struct.*, vol. 143, pp. 151–164, May 2016.
- [135] R. K. Watkins and L. R. Anderson, *Structural mechanics of buried pipes*. CRC press, 1999.
- [136] S. Bobba, Z. Leman, E. S. Zainuddin, and S. M. Sapuan, "Failures Analysis of E-Glass Fibre reinforced pipes in Oil and Gas Industry: A Review," *IOP Conf. Ser. Mater. Sci. Eng.*, vol. 217, no. 1, p. 012004, 2017.
- [137] B. C. Ray, S. T. Hasan, and D. W. Clegg, "Evaluation of Defects in FRP Composites by NDT Techniques," *J. Reinf. Plast. Compos.*, vol. 26, no. 12, pp. 1187–1192, Aug. 2007.
- [138] S. Gray, S. Ganchev, N. Qaddoumi, G. Beauregard, D. Radford, and R. Zoughi, "Porosity level estimation in polymer composites using microwaves," *Mater. Eval.*, vol. 53, no. 3, Mar. 1995.
- [139] N. Qaddoumi, S. Ganchev, and R. Zoughi, "Microwave diagnosis of low-density fiberglass composites with resin binder," *Res. Nondestruct. Eval.*, vol. 8, no. 3, pp. 177–188, Sep. 1996.
- [140] A. Hosoi, Y. Yamaguchi, Y. Ju, Y. Sato, and T. Kitayama, "Detection and quantitative evaluation of defects in glass fiber reinforced plastic laminates by microwaves," *Compos. Struct.*, vol. 128, pp. 134–144, Sep. 2015.
- [141] D.-H. Han and L.-H. Kang, "Nondestructive evaluation of GFRP composite including multi-delamination using THz spectroscopy and imaging," *Compos. Struct.*, vol. 185, pp. 161–175, Feb. 2018.
- [142] G. D'Angelo and S. Rampone, "Feature extraction and soft computing methods for aerospace structure defect classification," *Measurement*, vol. 85, pp. 192–209, May 2016.
- [143] S. Sumathi and S. N. Sivanandam, *Introduction to Data Mining and its Applications*. Berlin Heidelberg: Springer-Verlag, 2006.
- [144] X. Xu, E. L. Miller, C. M. Rappaport, and G. D. Sower, "Statistical method to detect subsurface objects using array ground-penetrating radar data," *IEEE Trans. Geosci. Remote Sens.*, vol. 40, no. 4, pp. 963–976, Apr. 2002.
- [145] A. C. Gurbuz, "Determination of Background Distribution for Ground-Penetrating Radar Data," *IEEE Geosci. Remote Sens. Lett.*, vol. 9, no. 4, pp. 544–548, Jul. 2012.

- [146] L. Nuzzo, “Coherent noise attenuation in GPR data by linear and parabolic Radon Transform techniques,” *Ann. Geophys.*, vol. 46, no. 3, Dec. 2003.
- [147] J. Baili, S. Lahouar, M. Hergli, I. L. Al-Qadi, and K. Besbes, “GPR signal de-noising by discrete wavelet transform,” *NDT E Int.*, vol. 42, no. 8, pp. 696–703, Dec. 2009.
- [148] J. Baili, S. Lahouar, M. Hergli, A. Amimi, and K. Besbes, “Application of the discrete wavelet transform to denoise GPR signals,” in *Proceedings from the Second International Symposium on Communications, Control and Signal Processing (ISCCSP), Marrakech, Morocco*, 2006, p. 11.
- [149] X. Xu, S. Peng, Y. Xia, and W. Ji, “The development of a multi-channel GPR system for roadbed damage detection,” *Microelectron. J.*
- [150] Z. Leng and I. L. Al-Qadi, “An innovative method for measuring pavement dielectric constant using the extended CMP method with two air-coupled GPR systems,” *NDT E Int.*, vol. 66, pp. 90–98, Sep. 2014.
- [151] C. Le Bastard, Y. Wang, V. Baltazart, and X. Derobert, “Time Delay and Permittivity Estimation by Ground-Penetrating Radar With Support Vector Regression,” *IEEE Geosci. Remote Sens. Lett.*, vol. 11, no. 4, pp. 873–877, Apr. 2014.
- [152] Z. Khakiev, V. Shapovalov, A. Kruglikov, A. Morozov, and V. Yavna, “Investigation of long term moisture changes in trackbeds using GPR,” *J. Appl. Geophys.*, vol. 110, pp. 1–4, Nov. 2014.
- [153] C. Le Bastard, V. Baltazart, Y. Wang, and J. Saillard, “Thin-Pavement Thickness Estimation Using GPR With High-Resolution and Superresolution Methods,” *IEEE Trans. Geosci. Remote Sens.*, vol. 45, no. 8, pp. 2511–2519, Aug. 2007.
- [154] G. Charvat, A. Temme, M. Feigin, and R. Raskar, “Time-of-Flight Microwave Camera,” *Sci. Rep.*, vol. 5, p. 14709, Oct. 2015.
- [155] S. Lahouar and I. L. Al-Qadi, “Automatic detection of multiple pavement layers from GPR data,” *NDT E Int.*, vol. 41, no. 2, pp. 69–81, Mar. 2008.
- [156] C. Le Bastard, V. Baltazart, and Y. Wang, “Modified ESPRIT (M-ESPRIT) algorithm for time delay estimation in both any noise and any radar pulse context by a GPR radar,” *Signal Process.*, vol. 90, no. 1, pp. 173–179, Jan. 2010.
- [157] L. Qu, Q. Sun, T. Yang, L. Zhang, and Y. Sun, “Time-Delay Estimation for Ground Penetrating Radar Using ESPRIT With Improved Spatial Smoothing Technique,” *IEEE Geosci. Remote Sens. Lett.*, vol. 11, no. 8, pp. 1315–1319, Aug. 2014.
- [158] M. Sun, C. Le Bastard, N. Pinel, and Y. Wang, “Estimation of time delay and roughness parameters by GPR using esprit method,” in *Geoscience and Remote Sensing Symposium (IGARSS), 2014 IEEE International*, 2014, pp. 2605–2608.
- [159] C. Kao, J. Li, Y. Wang, H. Xing, and C. R. Liu, “Measurement of Layer Thickness and Permittivity Using a New Multilayer Model From GPR Data,” *IEEE Trans. Geosci. Remote Sens.*, vol. 45, no. 8, pp. 2463–2470, Aug. 2007.
- [160] X. Feng, M. Sato, Y. Zhang, C. Liu, F. Shi, and Y. Zhao, “CMP Antenna Array GPR and Signal-to-Clutter Ratio Improvement,” *IEEE Geosci. Remote Sens. Lett.*, vol. 6, no. 1, pp. 23–27, Jan. 2009.
- [161] G. Meles, S. Greenhalgh, J. van der Kruk, A. Green, and H. Maurer, “Taming the non-linearity problem in GPR full-waveform inversion for high contrast media,” *J. Appl. Geophys.*, vol. 78, pp. 31–43, Mar. 2012.

- [162] N. Kwak and J.-W. Lee, "Feature extraction based on subspace methods for regression problems," *Neurocomputing*, vol. 73, no. 10–12, pp. 1740–1751, Jun. 2010.
- [163] V. Kabourek, P. Cerny, and M. Mazánek, "Clutter reduction based on principal component analysis technique for hidden objects detection," *Radioengineering*, vol. 21, no. 1, pp. 464–470, 2012.
- [164] K. H. Ko, G. Jang, K. Park, and K. Kim, "GPR-Based Landmine Detection and Identification Using Multiple Features," *Int. J. Antennas Propag.*, vol. 2012, p. e826404, Oct. 2012.
- [165] G. Y. Tian, A. Sophian, D. Taylor, and J. Rudlin, "Wavelet-based PCA defect classification and quantification for pulsed eddy current NDT," *IEE Proc. - Sci. Meas. Technol.*, vol. 152, no. 4, pp. 141–148, Jul. 2005.
- [166] A. Sophian, G. Y. Tian, D. Taylor, and J. Rudlin, "A feature extraction technique based on principal component analysis for pulsed Eddy current NDT," *NDT E Int.*, vol. 36, no. 1, pp. 37–41, Jan. 2003.
- [167] A. Miszczyk and K. Darowicki, "Inspection of protective linings using microwave spectroscopy combined with chemometric methods," *Corros. Sci.*, vol. 64, pp. 234–242, Nov. 2012.
- [168] M. A. Kramer, "Nonlinear principal component analysis using autoassociative neural networks," *AIChE J.*, vol. 37, no. 2, pp. 233–243, Feb. 1991.
- [169] S. Tan and M. L. Mayrovouniotis, "Reducing data dimensionality through optimizing neural network inputs," *AIChE J.*, vol. 41, no. 6, pp. 1471–1480, Jun. 1995.
- [170] H. G. Hiden, M. J. Willis, M. T. Tham, and G. A. Montague, "Non-linear principal components analysis using genetic programming," *Comput. Chem. Eng.*, vol. 23, no. 3, pp. 413–425, Feb. 1999.
- [171] B. Schölkopf, A. Smola, and K.-R. Müller, "Nonlinear Component Analysis as a Kernel Eigenvalue Problem," *Neural Comput.*, vol. 10, no. 5, pp. 1299–1319, Jul. 1998.
- [172] A. M. Jade, B. Srikanth, V. K. Jayaraman, B. D. Kulkarni, J. P. Jog, and L. Priya, "Feature extraction and denoising using kernel PCA," *Chem. Eng. Sci.*, vol. 58, no. 19, pp. 4441–4448, Oct. 2003.
- [173] C. S. Throckmorton, S. L. Tantom, Y. Tan, and L. M. Collins, "Independent component analysis for UXO detection in highly cluttered environments," *J. Appl. Geophys.*, vol. 61, no. 3–4, pp. 304–317, Mar. 2007.
- [174] H. Jui-feng and Z. Zheng-ou, "A new GPR targets feature extraction based on kernel method," in *2004 7th International Conference on Signal Processing, 2004. Proceedings. ICSP '04*, 2004, vol. 3, pp. 2159–2162 vol.3.
- [175] U. S. Khan, W. Al-Nuaimy, and F. E. Abd El-Samie, "Detection of landmines and underground utilities from acoustic and GPR images with a cepstral approach," *J. Vis. Commun. Image Represent.*, vol. 21, no. 7, pp. 731–740, Oct. 2010.
- [176] S. Esposito, P. Fallavollita, M. Corcione, and M. Balsi, "Experimental Validation of an Active Thermal Landmine Detection Technique," *IEEE Trans. Geosci. Remote Sens.*, vol. 52, no. 4, pp. 2040–2047, Apr. 2014.
- [177] E. Avci and R. Coteli, "A new automatic target recognition system based on wavelet extreme learning machine," *Expert Syst. Appl.*, vol. 39, no. 16, pp. 12340–12348, Nov. 2012.

- [178] Y. Zhang, P. Candra, G. Wang, and T. Xia, “2-D Entropy and Short-Time Fourier Transform to Leverage GPR Data Analysis Efficiency,” *IEEE Trans. Instrum. Meas.*, vol. 64, no. 1, pp. 103–111, Jan. 2015.
- [179] T. G. Savelyev, L. van Kempen, H. Sahli, J. Sachs, and M. Sato, “Investigation of Time-Frequency Features for GPR Landmine Discrimination,” *IEEE Trans. Geosci. Remote Sens.*, vol. 45, no. 1, pp. 118–129, Jan. 2007.
- [180] G. Lu and Y. Lei, “Investigation of time-frequency analysis in GPR signal using HHT method,” in *2014 4th IEEE International Conference on Network Infrastructure and Digital Content (IC-NIDC)*, 2014, pp. 334–337.
- [181] W. Jiang, “Signal processing strategies for ground-penetrating radar,” phd, University of Bath, 2011.
- [182] O. Missaoui, H. Frigui, and P. Gader, “Land-Mine Detection With Ground-Penetrating Radar Using Multistream Discrete Hidden Markov Models,” *IEEE Trans. Geosci. Remote Sens.*, vol. 49, no. 6, pp. 2080–2099, Jun. 2011.
- [183] X. Zhang, J. Bolton, and P. Gader, “A New Learning Method for Continuous Hidden Markov Models for Subsurface Landmine Detection in Ground Penetrating Radar,” *IEEE J. Sel. Top. Appl. Earth Obs. Remote Sens.*, vol. 7, no. 3, pp. 813–819, Mar. 2014.
- [184] H. Frigui and P. Gader, “Detection and Discrimination of Land Mines in Ground-Penetrating Radar Based on Edge Histogram Descriptors and a Possibilistic -Nearest Neighbor Classifier,” *IEEE Trans. Fuzzy Syst.*, vol. 17, no. 1, pp. 185–199, Feb. 2009.
- [185] P. A. Torrione, K. D. Morton, R. Sakaguchi, and L. M. Collins, “Histograms of Oriented Gradients for Landmine Detection in Ground-Penetrating Radar Data,” *IEEE Trans. Geosci. Remote Sens.*, vol. 52, no. 3, pp. 1539–1550, Mar. 2014.
- [186] V. R. N. dos Santos, W. Al-Nuaimy, J. L. Porsani, N. S. T. Hirata, and H. S. Alzubi, “Spectral analysis of ground penetrating radar signals in concrete, metallic and plastic targets,” *J. Appl. Geophys.*, vol. 100, pp. 32–43, Jan. 2014.
- [187] C. Maas and J. Schmalzl, “Using pattern recognition to automatically localize reflection hyperbolas in data from ground penetrating radar,” *Comput. Geosci.*, vol. 58, pp. 116–125, Aug. 2013.
- [188] A. V. Ristic, D. Petrovacki, and M. Govedarica, “A new method to simultaneously estimate the radius of a cylindrical object and the wave propagation velocity from GPR data,” *Comput. Geosci.*, vol. 35, no. 8, pp. 1620–1630, Aug. 2009.
- [189] M. A. Gonzalez-Huici and F. Giovanneschi, “A combined strategy for landmine detection and identification using synthetic GPR responses,” *J. Appl. Geophys.*, vol. 99, pp. 154–165, Dec. 2013.
- [190] A. Moreira, P. Prats-Iraola, M. Younis, G. Krieger, I. Hajnsek, and K. P. Papathanassiou, “A tutorial on synthetic aperture radar,” *IEEE Geosci. Remote Sens. Mag.*, vol. 1, no. 1, pp. 6–43, Mar. 2013.
- [191] A. L. Boyer, P. M. Hirsch, J. A. Jordan, L. B. Lesem, and D. L. Van Rooy, “Reconstruction of Ultrasonic Images by Backward Propagation,” in *Acoustical Holography*, 1971, pp. 333–348.
- [192] M. Soumekh, “Bistatic synthetic aperture radar inversion with application in dynamic object imaging,” *IEEE Trans. Signal Process.*, vol. 39, no. 9, pp. 2044–2055, Sep. 1991.
- [193] M. Soumekh, “A system model and inversion for synthetic aperture radar imaging,” *IEEE Trans. Image Process.*, vol. 1, no. 1, pp. 64–76, Jan. 1992.

- [194] M. Fallahpour and R. Zoughi, "Fast 3-D Qualitative Method for Through-Wall Imaging and Structural Health Monitoring," *IEEE Geosci. Remote Sens. Lett.*, vol. 12, no. 12, pp. 2463–2467, Dec. 2015.
- [195] Z. Li, J. Wang, J. Wu, and Q. H. Liu, "A Fast Radial Scanned Near-Field 3-D SAR Imaging System and the Reconstruction Method," *IEEE Trans. Geosci. Remote Sens.*, vol. 53, no. 3, pp. 1355–1363, Mar. 2015.
- [196] T. H. Kim, R. James, and R. M. Narayanan, "High-resolution nondestructive testing of multilayer dielectric materials using wideband microwave synthetic aperture radar imaging," in *Nondestructive Characterization and Monitoring of Advanced Materials, Aerospace, and Civil Infrastructure 2017*, vol. 10169, H. F. Wu, A. L. Gyekenyesi, P. J. Shull, and T. Y. Yu, Eds. Bellingham: Spie-Int Soc Optical Engineering, 2017, p. UNSP 1016903.
- [197] F. Gumbmann and L. Schmidt, "Millimeter-Wave Imaging With Optimized Sparse Periodic Array for Short-Range Applications," *IEEE Trans. Geosci. Remote Sens.*, vol. 49, no. 10, pp. 3629–3638, Oct. 2011.
- [198] J. T. Case, S. Kharkovsky, R. Zoughi, G. Steffes, and F. L. Hepburn, "Millimeter wave holographical inspection of honeycomb composites," *AIP Conf. Proc.*, vol. 975, no. 1, pp. 970–975, Feb. 2008.
- [199] K. A. Michalski and D. Zheng, "Electromagnetic scattering and radiation by surfaces of arbitrary shape in layered media. I. Theory," *IEEE Trans. Antennas Propag.*, vol. 38, no. 3, pp. 335–344, Mar. 1990.
- [200] Y. P. Chen, W. C. Chew, and L. Jiang, "A New Green's Function Formulation for Modeling Homogeneous Objects in Layered Medium," *IEEE Trans. Antennas Propag.*, vol. 60, no. 10, pp. 4766–4776, Oct. 2012.
- [201] K. A. Michalski and J. R. Mosig, "Multilayered media Green's functions in integral equation formulations," *IEEE Trans. Antennas Propag.*, vol. 45, no. 3, pp. 508–519, Mar. 1997.
- [202] Y. P. Chen, L. Jiang, Z. Qian, and W. C. Chew, "An Augmented Electric Field Integral Equation for Layered Medium Green's Function," *IEEE Trans. Antennas Propag.*, vol. 59, no. 3, pp. 960–968, Mar. 2011.
- [203] D. Hughes *et al.*, "Microwave Nondestructive Detection of Corrosion Under Thin Paint and Primer in Aluminum Panels," *Subsurf. Sens. Technol. Appl.*, vol. 2, no. 4, pp. 435–471, Oct. 2001.
- [204] V. Lopresto and G. Caprino, "Damage Mechanisms and Energy Absorption in Composite Laminates Under Low Velocity Impact Loads," in *Dynamic Failure of Composite and Sandwich Structures*, S. Abrate, B. Castanié, and Y. D. S. Rajapakse, Eds. Springer Netherlands, 2013, pp. 209–289.
- [205] A. Drach, B. Drach, and I. Tsukrov, "Processing of fiber architecture data for finite element modeling of 3D woven composites," *Adv. Eng. Softw.*, vol. 72, pp. 18–27, Jun. 2014.
- [206] Z. Wang, G. Tian, M. Meo, and F. Ciampa, "Image processing based quantitative damage evaluation in composites with long pulse thermography," *NDT E Int.*, vol. 99, pp. 93–104, Oct. 2018.
- [207] X. Yang, Y. R. Zheng, M. T. Ghasr, and K. M. Donnell, "Microwave Imaging From Sparse Measurements for Near-Field Synthetic Aperture Radar," *IEEE Trans. Instrum. Meas.*, vol. PP, no. 99, pp. 1–13, 2017.

- [208] B. Langmann, W. Weihs, K. Hartmann, and O. Loffeld, "Development and Investigation of a Long-Range Time-of-Flight and Color Imaging System," *IEEE Trans. Cybern.*, vol. 44, no. 8, pp. 1372–1382, Aug. 2014.
- [209] Y. Song, C. A. Glasbey, G. Polder, and G. W. A. M. van der Heijden, "Non-destructive automatic leaf area measurements by combining stereo and time-of-flight images," *IET Comput. Vis.*, vol. 8, no. 5, pp. 391–403, Feb. 2014.
- [210] J. S. Lee, C. Nguyen, and T. Scullion, "A novel, compact, low-cost, impulse ground-penetrating radar for nondestructive evaluation of pavements," *IEEE Trans. Instrum. Meas.*, vol. 53, no. 6, pp. 1502–1509, Dec. 2004.
- [211] D. M. Sheen, D. L. McMakin, and T. E. Hall, "Three-dimensional millimeter-wave imaging for concealed weapon detection," *IEEE Trans. Microw. Theory Tech.*, vol. 49, no. 9, pp. 1581–1592, Sep. 2001.
- [212] S. S. P. Council, "Surface preparation," *Syst. Specif.*, vol. 2, 1991.
- [213] M. Kempin, M. T. Ghasr, J. T. Case, and R. Zoughi, "Modified Waveguide Flange for Evaluation of Stratified Composites," *IEEE Trans. Instrum. Meas.*, vol. 63, no. 6, pp. 1524–1534, Jun. 2014.
- [214] J. Zhang and G. Tian, "UHF RFID Tag Antenna-Based Sensing for Corrosion Detection and Characterization Using Principal Component Analysis," *IEEE Trans. Antennas Propag.*, vol. PP, no. 99, pp. 1–1, 2016.
- [215] J. A. Cuenca *et al.*, "Study of the magnetite to maghemite transition using microwave permittivity and permeability measurements," *J. Phys. Condens. Matter*, vol. 28, no. 10, p. 106002, 2016.
- [216] A. Sentenac, H. Giovannini, and M. Saillard, "Scattering from rough inhomogeneous media: splitting of surface and volume scattering," *J. Opt. Soc. Am. A*, vol. 19, no. 4, p. 727, Apr. 2002.
- [217] O. J. F. Martin and M. Paulus, "Influence of metal roughness on the near-field generated by an aperture/apertureless probe," *J. Microsc.*, vol. 205, no. 2, pp. 147–152, Feb. 2002.
- [218] R. Akkerman, "Laminate mechanics for balanced woven fabrics," *Compos. Part B Eng.*, vol. 37, no. 2–3, pp. 108–116, Apr. 2005.
- [219] S. Sanchez-Saez, E. Barbero, R. Zaera, and C. Navarro, "Compression after impact of thin composite laminates," *Compos. Sci. Technol.*, vol. 65, no. 13, pp. 1911–1919, Oct. 2005.
- [220] S. Petit, C. Bouvet, A. Bergerot, and J.-J. Barrau, "Impact and compression after impact experimental study of a composite laminate with a cork thermal shield," *Compos. Sci. Technol.*, vol. 67, no. 15–16, pp. 3286–3299, Dec. 2007.
- [221] R. Olsson, "Analytical prediction of damage due to large mass impact on thin ply composites," *Compos. Part Appl. Sci. Manuf.*, vol. 72, pp. 184–191, May 2015.
- [222] Z. Shen and H. Zhou, "Mechanical and electrical behavior of carbon fiber structural capacitors: Effects of delamination and interlaminar damage," *Compos. Struct.*, vol. 166, pp. 38–48, Apr. 2017.
- [223] C. W. Chen, J. Luo, and K. J. Parker, "Image segmentation via adaptive K-mean clustering and knowledge-based morphological operations with biomedical applications," *IEEE Trans. Image Process.*, vol. 7, no. 12, pp. 1673–1683, Dec. 1998.